教育部補助大專校院延攬國際頂尖人才

年度績效報告

學校名稱及聘任系所：國立清華大學物理學系	學門領域：理學
學者姓名：藤森淳 (Atsushi Fujimori)	■玉山學者 □玉山青年學者
報告年度：**110** 年 **(第 1 年)**	

藤森淳 (Atsushi Fujimori)

二、質化績效說明（執行成果得累計呈現，如：第 2 年之年度績效報告，可包含第 1 年及第 2 年之成果）

審查重點	預期達成目標	執行績效及目標達成情形說明	檢附資料
一、玉山（青年）學者之研究工作主要內容及全程經過概述。	藤森教授的研究工作主要是使用同步輻射中心(NSRRC)之設備對包括銅酸鹽(cuprate)超導體、鐵基超導體等凝態系統進行軟 X 光共振非彈性散射(RIXS)、角解析光電子能譜(ARPES)或 X-光磁性圓二色性(x-ray magnetic circular dichroism, XMCD)的測量，這次來台的工作重點特別是在高溫超導體中與電荷有關之電荷密度 (charge density wave)以及配對密度波(pair density wave)以及 Ni_3TeO_6 反鐵磁系統。主要的目標為研究這些序參量或密度波之漲落是否與超導競爭或合作，並研究哪些序參量/漲落在實現高溫超導中起關鍵作用。另外在 Ni_3TeO_6 反鐵磁系統中，特別是要探討 X-光磁性圓二色性是否能偵測到反鐵磁序以及與拓撲有關的 Berry curvature 的拓撲量。	由於疫情的關係，藤森教授的訪台延後，經教育部申請「特別入境許可」簽證辦理後，於 111 年 3 月 10 日入台隔離 14+3 天後抵達清華大學後，即開始使用預先申請的光束時間(beam time)進行實驗測量。期間李定國院士亦由中山大學轉至清華大學，與同步輻射中心黃迪靖研究員、物理系牟中瑜(計劃主持人)針對高溫超導體中的電荷密度與配對密度波之測量進行多次討論，藤森教授並於 6 月 1 日做了一場公開的演講(colloquium): “Open issues in high-temperature superconductors: challenges with advance spectroscopies”。在預定達到的目標上，已完成多項工作(見以下說明與檢附資料)並開啟多項合作工作，這些合作在藤森教授離台後會持續進行並完成之。	如 Appendices 1, 2, 3, 4, 5

審查重點	預期達成目標	執行績效及目標達成情形說明	檢附資料
二、玉山（青年）學者未來研究主題與校務發展（包括高等教育深耕計畫）之連結及預期效益： （1） 學者研究規劃及目標。 （2） 學者研究主題內容及其與學校校務發展關聯	(1)學者研究規劃及目標 藤森教授的研究計劃旨在解決高溫超導體中的各種開放性問題，即包括銅酸鹽(cuprate)超導體，鐵基超導體及其在異質結構中的界面中未解決的問題。這些材料屬於所謂的非傳統超導體，其中電子相關性起了非常重要的作用，這與Bardeen-Cooper-Schrieffer（BCS）理論中可以理解的傳統超導體不同。在高溫超導體中，最近的研究已經發現到各種有序參量(orders)和擾動，例如自旋序參量/擾動，電荷序參量/擾動，向列型液晶（nematic）序參數/擾動以及庫珀對密度序參量/波動。藤森教授計劃首先確定這些序參量/漲落的性質，研究這些序參量/漲落是否與超導競爭或合作，並研究哪些序參量/漲落在實現高溫超導中起關鍵作用。特別地，最近發現在銅酸鹽超導體中普遍存在電荷序參量/擾動。他將重點研究它們與費米表面嵌套(nesting)，電子相關性，庫珀配對以及最終與高溫超導起源的關係。 藤森教授還計劃研究塊材、薄膜和原子層形式的過渡金屬化合物中的奇異(exotic)磁性及其各向異性。人們認為這種引人入勝的磁性來自自旋軌道相互作用和各向異性晶體樣品結構的綜合作用。他的目標是通過使用軟 X 射線光譜技術來消除自旋軌道相互作用和結構/電子各向異性在觀察到的現象中的作用。 (2)學者研究主題內容及其與學校校務發展關聯性 藤森教授的研究主題集中在以下領域： 1.銅酸鹽高溫超導體，鐵基超導體以及包含 3d 過渡金屬元素的相關超導材料的電子結構，其中強電子相關性為至關重要的作用。 2.過渡金屬化合物，稀釋的鐵磁半導體，異質界面和凡得瓦(van der Vaal)磁性材料的電子結構和磁性能，這些被認為是未來自旋電子學應用的有前途的材料。 3.開發用於強相關電子系統的軟 X 射線光譜研究的新儀器和數據分析方法 上述研究課題與清大物理系的許多凝聚態物理教授息息相關：牟中瑜教授是高溫超導和磁性理論的專家。 鄭宏泰教授是一位計算物理學家，從事相關電子材料的各種訂單研究，非常適合藤森教授當前的研究重點。陳正中教授與藤森教授在二維超導體方面有著共同的興趣，他們專門研究不同的光譜技術（紅外與軟 X 射線）。在高度相關的	通過 RIXS 闡明與銅酸鹽超導體中的電荷順序相關的量子臨界漲落：由藤森教授、牟中瑜教授 與李定國院士以及黃迪靖研究員以及黃筱妤博士完成。 證明 RIXS 在 $CuAl_2O_4$ 中揭示 Jahn-Teller 效應和自旋軌道耦合之間競爭的可行性：Profs. A. Fujimori, D.-J. Huang and Dr. H.-Y. Huang. 使用 RIXS 在空穴摻雜銅酸鹽中發現聲等離子體激發 Profs. A. Fujimori, T.-K. Lee, D.-J. Huang, Drs. H.-Y. Huang, and A. Singh. 發表在凝聚態物理期刊俱樂部(Journal club)上的關於鎳酸鹽和銅酸鹽超導體的量子臨界行為的評論：藤森教授	Appendix 1 Appendix 2 Appendix 3 Appendix 4

審查重點	預期達成目標	執行績效及目標達成情形說明	檢附資料
性。 （3） 具體工作績效或成果，內容請包括專題研究計畫期中進度報告。 （4） 預期成效（預計可達到量化或質化之具體成	系統理論上與 Miguel Cazalilla 教授進行互動將有益於雙方的研究。藤森教授已經與清大物理系的一些兼職教師建立了密切的關係：與黃迪靖教授和崔古鼎教授在國家同步輻射研究中心進行了長期卓有成效的合作。在過去的十年中，他經常與李定國教授進行交流，以對銅酸鹽高溫超導體的實驗數據進行理論解釋，並與吳茂昆教授進行交流，以交換有關鐵基超導體的信息。還應該指出的是，自 2005 年以來，藤森教授和黃迪靖教授一直組織有關強相關電子系統的年度台灣-日本-韓國研討會，並鼓勵了相關研究群，特別是該領域的年輕研究人員參與。他被任命為玉山學者將加強與 N 清華院系的互動，與他的新的富有成果的合作將使他們受益匪淺。 (3)研究工作之具體做法 藤森教授一直是以同步輻射加速器角分辨光電子能譜（ARPES）研究強關聯電子系統的世界領先專家之一。他還擅長於核心電子能階(core-level)光譜學，例如 X 射線吸收光譜（XAS）和 X 射線磁性圓二色性（XMCD）。最近，他與 NSRRC 的黃迪靖教授小組合作，將他的同步輻射光譜學工作擴展到了新近快速發展的共振非彈性 X 射線散射（RIXS）技術。黃教授的台灣光子源（TPS）光束線 41A 處的 RIXS 終端站現在擁有世界上最高的能量分辨率和高效的數據採集系統。對於藤森教授進行高溫超導體和相關電子材料的研究，該終端站將是一個極其強大的理想基地。 自 2011 年以來，藤森教授一直是 NSRRC 台灣光源（TLS）在 Dragon 光束線上的定期用戶，用於 XMCD 測量磁性化合物，薄膜和其他自旋電子材料。在台灣光子源(TPS)和光束線的建造期間，他還擔任 TPS 儲存環科學諮詢委員會的成員三年，並密切關注軟 X 射線光束線（包括 RIXS 光束線）的規劃。在過去的九年中，他還被任命為傑出訪問學者學者，並與黃迪靖教授的團隊合作。現在，藤森教授獲得了日本科學促進會（JSPS）的資助，與日本的材料科學團體合作，並支持學生從東京到 NSRRC 的旅行。最近，藤森教授參加了由計算物理學家領導的日本教育，文化，體育，科學和技術部（MEXT）的一個項目：該項目的目標是通過分析獲得對相關電子材料的深刻見解。通過結合第一原理和多體理論來分析 ARPES，RIXS 和 STM 光譜，兩者都嚴重依賴於下一代超級計算機“ Fugaku”的性能。 為了研究當前所感興趣的各種磁性材料和納米結構，藤森教授還將利用 XMCD。它是	物理系藤森教授的公開演講(colloquium)：“Open issues in high-temperature superconductors: challenges with advance spectroscopies” 關於銅酸鹽超導體中電子分數化(fractionalization)的工作已投稿：Profs. A. Fujimori, D.-Jing Huang, M. Imada, Dr. A. Singh. 具有結構手性的反鐵磁體 Ni_3TeO_6 的異常光譜特性分析：Profs. A. Fujimori, C.-Y. Mou, H.-T. Jeng, D.-J. Huang, and Dr. J. Okamoto. Manuscript under preparation. 計劃新的聯合研究項目“銅酸鹽高溫超導體中庫珀對密度波動力學的 RIXS 研究”： Profs. A. Fujimori, C.-Y. Mou, T.-K. Lee and D.-J. Huang.	Appendix 5

審查重點	預期達成目標	執行績效及目標達成情形說明	檢附資料
果） ※如有量化績效者，請另再填寫附件 1	一種強大而獨特的局部磁性探測器，通過它可以將磁矩分成每個原子位點的自旋和軌道分量。有關自旋和軌道力矩的個別信息對於闡明磁性材料的磁各向異性是必不可少的，因為磁各向異性是由自旋軌道耦合以及結構和/或電子各向異性的綜合作用引起的。 (4)預期成效(預計可達到量化或質化之具體成果) 藤森教授將持續並與台灣的研究學者合作研發，將在高影響力的期刊上發表出版物。通過此次任命，藤森教授將能夠在台灣停留更長的時間，並將能夠促進與當前清華大學合作夥伴之間的合作並將其擴展到其他學院。他還將能夠更頻繁地與他們的學生互動。在任命期之後，在此期間建立的研究網絡也將繼續，甚至在兩國之間的年輕合作者之間發展。		
三、學校申請計畫原定目標暨支持成效。（請敘明學校協助學者進行教學研究所提供之各項配合措施或經費，如研究設備及經費、研究	**學校提供配套措施及條件**(例如研究經費與設備、研究助理人事費、住宿與搬遷費、子女教育協助事項等；前開措施所需經費，學校可自籌經費及運用政府部門補助經費方式籌措。如有與企業合作提供實驗設備、共組研發團隊或挹注經費等相關配套措施，亦請特別敘明)。 (一)學校整體之配套措施 1.新聘教師學術專案補助費(start up 起始費) (1)補助目的：鼓勵本校新聘教師從事學術研究，協助建立必須之研究設施。 (2)補助對象：到校任職半年內，經系所(中心)推薦之新聘教師。 (3)補助內容：補助研究相關之經費，惟不包括申請人之薪資津貼。補助經費總額及項目：總額以不超過 150 萬元為原則，由校款及學校管理費支付。由系所(中心)、院(含清華學院)、校以對等比例共同補助。 2.宿舍及房租津貼補助 (1)新聘教師原則優先配住「學人宿舍」，房型為一房及兩房。此外，尚有清華會館及第二招待所可供申請。國立清華大學招待所管理要點及收費標準詳見 http://affairs.site.nthu.edu.tw/p/404-1165-44868.php。	藤森教授來訪的住宿、搬遷以及研究所需之開辦費已完全由清華大學支付[redacted]。又藤森教授於清華期間使用物理系 718 室辦公室、並配有大電腦螢幕以及市內電話，設備齊全。	[redacted]

審查重點	預期達成目標	執行績效及目標達成情形說明	檢附資料
助理人事費、住宿搬遷、子女教育協助事項等）	(2)房租津貼補助：編制內新聘專任教師符合本校房租津貼要件者每月補助 10,000 元，自到職日起至多 3 年。 3.子女入學 (1)國立清華大學附設實驗小學及幼兒園優先入學： 依本校附設實驗國小學新生入學辦法及幼兒園招生簡章，本校編制內專任之教職員工之子女享有清華附小與幼兒園優先入學資格。 (2)國立科學工業園區實驗高級中學具有入學申請資格： 本校編制內專任教職員及學校約用人員之子女可申請國立科學工業園區實驗高級中學之國中部、國小部、幼兒園部新生及轉學生入學。 (3)子女教育補助費：依「全國軍公教員工待遇支給要點」標準補助。 http://person.site.nthu.edu.tw/p/406-1066-12001,r940.php?Lang=zh-tw 4.福利事項 (1)生日禮券：編制內教職員每年發給。 (2)健康檢查補助：年滿 40 歲以上編制內教職員，兩年補助一次。 (3)優惠團體保險：請參考人事室員工福利網站。 (4)優惠存款：郵局、兆豐銀行、玉山銀行。 (5)體育場館：本校教職員工優惠使用重訓室、羽球館、游泳池；參加各種舞蹈班；借用運動器材。 5.教學資源與輔助 (1)提供「新進教師研習營」 (2)提供「教師研習工作坊」 (3)設置「教師社群」 (4)提供「教師教學精進錄影」服務 (5)支援「個別教學發展計畫」 (二)擬聘單位(系所/院)之配套措施(如有與企業合作提供實驗設備、共組研發團隊或挹注經費等相關配套措施，亦請特別敘明)		

<table>
<tr><th>審查重點</th><th>預期達成目標</th><th>執行績效及目標達成情形說明</th><th>檢附資料</th></tr>
<tr><td></td><td>理學院物理系將提供必要的辦公室空間、實驗室資源，並安排適切的實驗室資源。在住宿部分，將協助申請清華會館，方便在校園研究與活動。

(三)學校(系所/院/校)自籌經費(相關配套措施)之項目及金額表

<table><tr><th>項 目 / 年度</th><th>研究經費</th><th>住宿費</th><th>學校自籌經費(相關配套措施)
小計(元)
☐ 一整年總數
■ 3 個月總數
(請見備註)</th></tr><tr><td>[redacted]</td><td>[redacted]</td><td>[redacted]</td><td>[redacted]</td></tr><tr><td>[redacted]</td><td>[redacted]</td><td>[redacted]</td><td>[redacted]</td></tr><tr><td>[redacted]</td><td>[redacted]</td><td>[redacted]</td><td>[redacted]</td></tr><tr><td>[redacted]</td><td>[redacted]</td><td>[redacted]</td><td>[redacted]</td></tr></table>備註：玉山學者(短期交流者)請填寫 3 個月總數，其餘請填寫一整年總數。</td><td></td><td></td></tr>
</table>

<table>
<tr><th>審查重點</th><th>預期達成目標</th><th>執行績效及目標達成情形說明</th><th>檢附資料</th></tr>
<tr><td>四、玉山學者團隊合作情形（請敘明團隊成員及合作方式）（玉山青年學者免填）</td><td>(一)團隊合作建立規劃情形
自 2011 年以來，藤森教授一直國家同步輻射中心台灣光源（TLS）的經常用戶，用於磁性材料的 XMCD 測量，並且自那時以來一直與黃迪靖教授合作擔任同步輻射中心的傑出學者。他與牟中瑜、李定國與吳茂昆教授以相遇經常在會議上和通過相互訪問，對超導性研究進行反復和廣泛的討論。他將與其他擁有共同興趣的清華大學研究小組進行更緊密的互動和協作。關於與日本材料科學團體的合作，該團體為他的團隊提供了高質量的單晶，藤森教授已獲得了日本科學促進會（JSPS）的資助，這筆款項還將用於支持日本的科學旅行使日本的學生也加了使用同步輻射中心的光束時間。

(二)團隊成員名單 (成員應包括校內副教授職級以下成員或博士後研究人員)
<table>
<tr><th>姓名</th><th>單位</th><th>職稱</th></tr>
<tr><td>牟中瑜</td><td>清華大學物理系</td><td>教授</td></tr>
<tr><td>鄭宏泰</td><td>清華大學物理系</td><td>教授</td></tr>
<tr><td>陳正中</td><td>清華大學物理系</td><td>教授</td></tr>
<tr><td>Miguel Cazalilla</td><td>清華大學物理系</td><td>教授</td></tr>
<tr><td>徐斌睿</td><td>清華大學物理系</td><td>助理教授</td></tr>
<tr><td>黃迪靖</td><td>清華大學物理系/同步輻射中心</td><td>合聘教授</td></tr>
<tr><td>崔古鼎</td><td>清華大學物理系/同步輻射中心</td><td>合聘教授</td></tr>
<tr><td>李定國</td><td>清華大學物理系/中山大學</td><td>合聘教授</td></tr>
<tr><td>吳茂昆</td><td>清華大學物理系/中研院物理所</td><td>合聘教授</td></tr>
<tr><td>岡本淳(Jun Okamoto)</td><td>同步輻射中心</td><td>助研究員</td></tr>
<tr><td>黃筱妤</td><td>同步輻射中心</td><td>博士後研究員</td></tr>
</table>
</td><td>藤森教授已經開始與團隊成員名單中牟中瑜教授、李定國院士、鄭宏泰教授、黃迪靖教授、岡本淳助理研究員以及黃筱妤博士合作。
他還將合作擴展到同步輻射中心的助理科學家 Amol Singh 博士。</td><td>Appendices 1, 2, and 3.</td></tr>
</table>

審查重點	預期達成目標	執行績效及目標達成情形說明	檢附資料
五、玉山（青年）學者國際化合作，鏈結接軌國外學術資源合作交流，與學校發展相結合；學者亦應善用其國際學術網絡資源，協助任職學校國際化，推動國際交流合作（包括國際師生交換、跨國合作研究、雙聯學制）	藤森教授的目標是在 NTHU 教職員工和 NSRRC 合作者的支持下建立一個全球相關電子系統研究網絡。在玉山院士任職期間建立的研究網絡預計將在此期間繼續發展。該網絡的海外成員包括來自日本和美國的材料科學家、來自日本和俄羅斯的凝聚態理論家、來自日本和德國的初始階段的同步輻射實驗家。該網絡將隨著研究合作的發展而發展。特別是與大型現有研究項目的合作，例如基於超級計算機 Fugaku 的計算物理項目和同步加速器輻射設施 SPring-8 的 X 射線光譜組，將有利於並加強我們的國際研究網絡。 NSRRC 的台灣光子源用戶也將參與並構成網絡。 台日韓強相關係統研討會系列將在因 COVID-19 而中斷幾年後重新啟動，並將作為三個國家之間以及與包括台灣在內的其他國家的互動和思想交流的平台。網絡成員。研討會將大力鼓勵年輕研究人員和學生在國際氛圍中參與。	第二項問題中“玉山學者未來的研究課題與大學的發展和預期收益之間的聯繫”來自於所提的全球網絡的初始階段。 藤森教授擔任國際會議的組委會成員：“Spectroscopies in Novel Superconductors (SNS)”、“Integrated Spectroscopy for Strong Electron Correlation”和“International Symposium on Superconductivity (ISS)”	Appendices 1-3

附件 1

量化績效說明

項目		成果及具體工作績效	說明
1.人才培育		碩博班課程_ 1__堂 學士班課程___堂 博士生__0_人 碩士生__1_人 學士生__0_人 其他____0__	定期指導在同步輻射工作的清華學生。
2.論文著作	國內	期刊論文_0__篇 專書及專書論文_0__本 研討會論文__0_篇 技術報告_0__篇 其他__0_	
	國外	期刊論文_16__篇 專書及專書論文_0__本 研討會論文_0__篇 技術報告_0__篇 其他_2__	在 15 篇期刊論文中，有 4 篇與清華大學和同步輻射教授的合作。“其他”一項包括的是評論文章。
3.專題演講		__1_場次	
4.專利 （含申請中）	國內	___件	
	國外	___件	
	■ 不適用		
5.產學合作		產學合作企業_0__家	
		產學合作計畫__0_案	
6.技術移轉		技轉授權___項	
		技術移轉授權金合計（金額）___元	
		■ 不適用	
7.其他		擔任某期刊特刊的客座編輯。	J. Phys. Soc. Jpn. 90, No. 11 (2021). Int’l Workshop “Integrated Spectroscopy for Strong Electron Correlation”

Quantum Fluctuations of Charge Order Induce Phonon Softening in a Superconducting Cuprate

H. Y. Huang,[1] A. Singh,[1] C. Y. Mou,[2] S. Johnston,[3] A. F. Kemper,[4] J. van den Brink,[5] P. J. Chen,[6,7] T. K. Lee,[8,9] J. Okamoto,[1] Y. Y. Chu,[1] J. H. Li,[10,1] S. Komiya,[11] A. C. Komarek,[12] A. Fujimori,[13,1] C. T. Chen,[1] and D. J. Huang[1,10,*]

[1]*National Synchrotron Radiation Research Center, Hsinchu 30076, Taiwan*
[2]*Center for Quantum Technology and Department of Physics, National Tsing Hua University, Hsinchu 30013, Taiwan*
[3]*Department of Physics and Astronomy, The University of Tennessee, Knoxville, Tennessee 37996, USA*
[4]*Department of Physics, North Carolina State University, Raleigh, North Carolina 27695, USA*
[5]*Institute for Theoretical Solid State Physics, IFW Dresden, Helmholtzstrasse 20, D 01069 Dresden, Germany*
[6]*Department of Mechanical Engineering, City University of Hong Kong, Kowloon, Hong Kong 999077, China*
[7]*Hong Kong Institute for Advanced Study, City University of Hong Kong, Kowloon, Hong Kong 999077, China*
[8]*Institute of Physics, Academia Sinica, Taipei 11529, Taiwan*
[9]*Department of Physics, National Sun Yat sen University, Kaohsiung 80424, Taiwan*
[10]*Department of Physics, National Tsing Hua University, Hsinchu 30013, Taiwan*
[11]*Central Research Institute of Electric Power Industry, Yokosuka, Kanagawa 240 0196, Japan*
[12]*Max Planck Institute for Chemical Physics of Solids, Nöthnitzer Straße 40, 01187 Dresden, Germany*
[13]*Department of Applied Physics, Waseda University, Shinjuku ku, Tokyo 169 8555, Japan*

(Received 3 April 2021; revised 13 August 2021; accepted 29 September 2021; published 23 November 2021)

Quantum phase transitions play an important role in shaping the phase diagram of high temperature cuprate superconductors. These cuprates possess intertwined orders which interact strongly with superconductivity. However, the evidence for the quantum critical point associated with the charge order in the superconducting phase remains elusive. Here, we reveal the short range charge orders and the spectral signature of the quantum fluctuations in $La_{2-x}Sr_xCuO_4$ (LSCO) near the optimal doping using high resolution resonant inelastic x ray scattering. On performing calculations through a diagrammatic framework, we discover that the charge correlations significantly soften several branches of phonons. These results elucidate the role of charge order in the LSCO compound, providing evidence for quantum critical scaling and discommensurations associated with charge order.

DOI: 10.1103/PhysRevX.11.041038

Subject Areas: Condensed Matter Physics
Strongly Correlated Materials
Superconductivity

I. INTRODUCTION

When doped with holes or electrons, cuprates at low temperatures can be tuned from a Mott insulating phase to a superconducting phase and then to a Fermi-liquid phase. In addition, an enigmatic pseudogap phase exists in the underdoped regime of hole-doped cuprates above the superconductivity transition temperature T_C with a crossover temperature T^*, which decreases monotonically when the doping is increased [1]. Several symmetry-breaking orders such as charge-density waves (CDWs) have also been discovered in the cuprates with comparable onset temperatures [2].

Charge fluctuations are one of the most fundamental collective excitations in matter. Recently, CDWs in cuprate superconductors have attracted renewed interest [3–25], but their mechanism and competition with superconductivity remain subjects of vigorous discussion. The wave vector of the CDW, for example, exhibits an inconsistent evolution with doping in various cuprate families [7,8]. This observation has lead to debate on whether real-space local interactions or Fermi surface nesting in momentum space underlies the CDW physics. Moreover, CDWs are coupled to phonons in cuprates [22–33], but the underlying mechanism of phonon softening remains a mystery [6], although lattice vibrations in metals can be damped or softened by electronic quasiparticles or excitations.

*djhuang@nsrrc.org.tw

Upon tuning a nonthermal parameter through a critical value, quantum phase transitions occur at the absolute zero of temperature T. The putative quantum critical point (QCP) in a cuprate holds the key to understanding many profound phenomena related to its superconductivity [34–40]. Anomalous thermodynamic [38] and transport properties [39,40] of cuprates close to a QCP have been observed. For example, as temperature T approaches zero, the electrical resistivity varies linearly with T rather than the T^2 dependence of a Fermi liquid. In approaching a QCP, two quantum states of the system can exchange their energy ordering. As a result, a CDW state can be intertwined with the superconducting state. Also, because the energy difference is small, switching back and forth between CDW and superconducting ground states is energetically likely, resulting in quantum charge fluctuations. Interestingly, recent resonant inelastic x-ray scattering (RIXS) studies have found that the charge-density fluctuations permeate through a broad region of the cuprate phase diagram [10].

A crucial task in the scenario of the presence of QCP is to identify the ordered phases that terminates at the QCP. In the present work, we presume the ordered phases to be the CDW order and try to find evidence for the QCP associated with the CDW in the superconducting phase. Inelastic x-ray scattering (IXS) probes charge fluctuations by measuring the dynamical structure factor $S(\mathbf{q},\omega)$, which is the space and time Fourier transformation of the density-density correlation function. Here, $\hbar\mathbf{q}$ and $\hbar\omega$ are the momentum and energy transferred to charge excitations, respectively, with $\hbar$ being the Planck constant h divided by 2π. For a given electron system of charge density $n(\mathbf{r},t)$ at position $\mathbf{r}$ and time t, the charge fluctuation is $\delta n(\mathbf{r},t) = n(\mathbf{r},t) - \langle n(\mathbf{r},t)\rangle$, in which $\langle\cdots\rangle$ denotes the quantum statistical average. The density-density correlation function $\langle n(\mathbf{r},t)n(\mathbf{r}',t')\rangle$ can then be written as

$$\langle n(\mathbf{r},t)n(\mathbf{r}',t')\rangle = \langle n(\mathbf{r},t)\rangle\langle n(\mathbf{r}',t')\rangle + \langle \delta n(\mathbf{r},t)\delta n(\mathbf{r}',t')\rangle. \tag{1}$$

In the presence of disorder, an additional average over disorders must be taken over Eq. (1). X-ray scattering data, thus, comprise contributions of the static charge distribution $\langle n(\mathbf{r},t)\rangle\langle n(\mathbf{r}',t')\rangle$ and its dynamical fluctuations $\langle \delta n(\mathbf{r},t)\delta n(\mathbf{r}',t')\rangle$, corresponding to charge susceptibilities denoted by $\chi_0(\mathbf{q},\omega)$ and $\chi(\mathbf{q},\omega)$, respectively. In addition, through the fluctuation-dissipation theorem, $S(\mathbf{q},\omega)$ is related to the charge susceptibility $\chi(\mathbf{q},\omega)$ by $S(\mathbf{q},\omega) = 2\hbar(1-e^{-\beta\hbar\omega})^{-1}\mathrm{Im}\chi(\mathbf{q},\omega)$, in which $\beta = 1/k_BT$, with k_B denoting the Boltzmann constant.

O K-edge RIXS probes certain characteristics of the dynamical charge fluctuations of CDWs, although additionally modulated by the effects of RIXS matrix elements, light polarization, and orbital characters [10,23,41,42]. In this work, we perform high-resolution O K-edge RIXS measurements and theoretical calculations through a diagrammatic framework to investigate the quantum fluctuations of charge order in superconducting cuprate $La_{2-x}Sr_xCuO_4$ (LSCO) near the optimal doping. Our results elucidate the role of charge order in the LSCO compound, providing evidence for the quantum critical scaling associated with charge order.

II. RIXS MEASUREMENTS

A. Experimental

The LSCO single crystals with the doping level $x = 0.15$ are grown by the traveling-solvent floating zone method [43–45]. After growth, the crystals are annealed to remove oxygen defects. The value of x is determined from an inductively-coupled-plasma atomic-emission spectrometric analysis. The T_C of the $x = 0.15$ sample is 37.5 K.

We conduct O K-edge RIXS measurements using the AGM-AGS spectrometer of beam line 41A at Taiwan Photon Source of National Synchrotron Radiation Research Center, Taiwan [46]. This recently constructed AGM-AGS beam line is based on the energy compensation principle of grating dispersion. High-resolution RIXS data are measured with an energy resolution of 16 meV at an incident photon energy of 530 eV. See Supplemental Material [47] for the details of the AGM-AGS spectrometer and data analysis.

B. Charge order of LSCO

We first measure static charge distributions $\langle n(\mathbf{r},t)\rangle\langle n(\mathbf{r}',t')\rangle$ of LSCO with $x = 0.15$ using energy-resolved elastic x-ray scattering. Figure 1(a) plots the intensity of O K-edge elastic scattering as a function of in-plane wave vector change $\mathbf{q}_\parallel$ varied along the antinodal direction $(\pi,0)$ at various temperatures. We observe CDW correlations in LSCO with an in-plane modulation vector $\mathbf{q}_{\mathrm{CDW}} = (0.235,0)$, which is given in reciprocal lattice units (r.l.u.) throughout this paper. Figures 1(c) and 1(d) show, respectively, the temperature-dependent CDW intensity and correlation length (ξ) defined as the inverse of the half width at half maximum (HWHM) of the momentum scan. The charge order of optimally doped LSCO exhibits a short correlation length, ranging from 22 to 12 Å. Consistent with previous results of LSCO, the CDWs are slightly suppressed in the superconducting phase as the temperature is decreased across T_C [5,9].

The observed charge correlations of LSCO persist over a wide temperature range, up to well above T^* and into the strange-metal phase. These correlations achieve no long-range charge order, however, in contrast with other La-214 cuprates. For example, $La_{1.48}Nd_{0.4}Sr_{0.12}CuO_4$ (Nd-LSCO), which has a low-temperature tetragonal (LTT) structure, shows long-range and short-range charge orders, as plotted in Fig. 1(b). The short-range charge order of LSCO might be caused by spatial disorders or phase separation arising

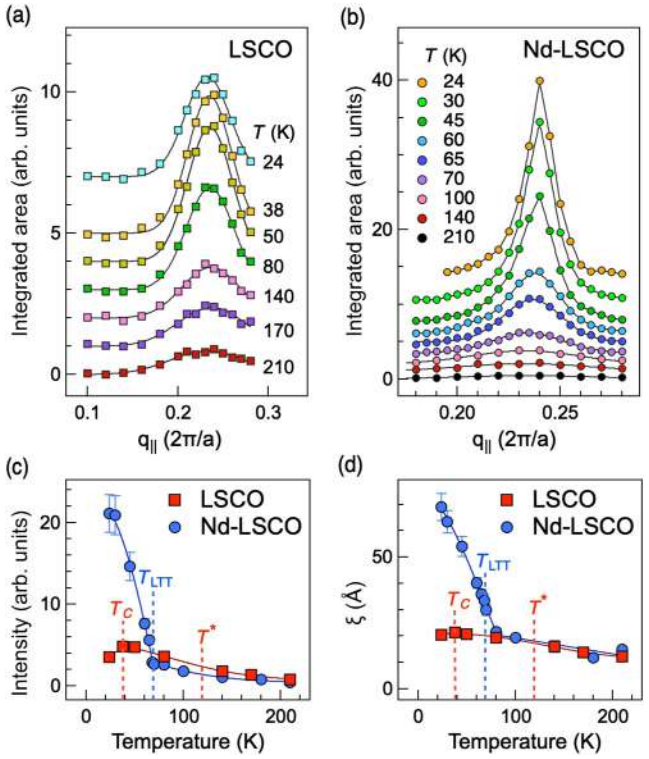

FIG. 1. O K edge elastic scattering of La 214 cuprates. (a),(b) Scattering intensities of LSCO and Nd LSCO vs in plane momentum $\mathbf{q}_{\parallel}$ along the antinodal direction $(\pi, 0)$ at various temperatures. Energy resolved elastic scattering plots are extracted from the integrated area of O K edge RIXS over the energy from −5 to 5 meV. The incident x ray energy for the RIXS spectra is tuned to the mobile hole of the so called Zhang Rice singlet (ZRS) with an absorption energy near 528.5 eV. All spectra are vertically offset for clarity. (c),(d) CDW intensity and correlation length (ξ) of LSCO and Nd LSCO as a function of the temperature, respectively. The vertical dashed lines show T_C and T^* of LSCO and structural transition temperature T_{LTT} of Nd LSCO. All solid lines serve as visual guidance.

from a subtle balance between Coulomb interactions and kinetic energy. At this time, we cannot determine if the CDWs with $\mathbf{q}_{\mathrm{CDW}} = (0.235, 0)$ are truly incommensurate or instead appear incommensurate due to defects known as discommensurations in the commensurate CDW state [48–51]. In a discommensurated structure, locally commensurate CDW regions are separated by discommensurations within which the CDW phase varies rapidly.

To unveil the charge instability and the coupling between CDW fluctuations and phonons in LSCO, we perform high-resolution O K-edge RIXS measurements. Figure 2(a) presents a series of temperature-dependent RIXS intensity distribution maps in the plane of energy loss vs in-plane momentum transfer $\mathbf{q}_{\parallel}$ along $(\pi, 0)$; Fig. 2(b) shows those maps after the subtraction of elastic scattering. There exists a pronounced excitation feature of energy about 14 meV in the neighborhood of $\mathbf{q}_{\mathrm{CDW}}$. Its intensity decreases with increasing temperature, unlike that of the static CDW intensity that has a maximum at T_C as plotted in Fig. 1(c) with red squares. This low-energy RIXS excitation appears to shift away from $\mathbf{q}_{\mathrm{CDW}}$ when the thermal energy approaches the excitation energy. This reflects that, at low temperatures, the low-energy RIXS excitation is dominated by charge-density fluctuations and its contribution from the coupling of CDW to acoustic phonons increases with the increase of temperature, as discussed later.

C. CDW fluctuations

For a system that exhibits a QCP associated with charge order, $S(\mathbf{q}, \omega)$ near $\mathbf{q}_{\mathrm{CDW}}$ measures the collective fluctuations sensitive to the proximity of the QCP. When the thermal energy $k_B T$ is less than the typical energy of order parameter fluctuations and less than energy $\hbar\omega$, their quantum nature is important. For low temperatures, we expect that the finite frequency fluctuation is dominated by the amplitude fluctuation of the charge density, and the following phenomenological form for charge susceptibility describes the quantum fluctuations [10,35]:

$$\chi_{\mathrm{CDW}}(\mathbf{q}_{\parallel}, \omega) = \frac{1}{\Delta^2 + c^2(\mathbf{q}_{\parallel} - \mathbf{q}_{\mathrm{CDW}})^2 - (\omega + i\Gamma_{\mathrm{CDW}})^2}. \tag{2}$$

Here, Δ is the characteristic energy of the fluctuations at $T = 0$ and can be interpreted as the inverse correlation length for the amplitude fluctuations. One expects that the characteristic energy Δ vanishes when the doping level approaches the quantum critical point. c is a parameter that characterizes the speed of the excitations with dispersion $\omega \sim c|\mathbf{q}_{\parallel} - \mathbf{q}_{\mathrm{CDW}}|$, and Γ_{CDW} is a parameter that characterizes the lifetime of the CDW amplitude excitations. In contrast, the static charge susceptibility $\chi_0(\mathbf{q}, \omega)$ vanishes except for $\omega \sim 0$ and its nearby region of CDW phase fluctuations characterized by Eq. (2) with $\Delta = 0$ and parameters c and Γ_{CDW}. This energy region is beyond our RIXS energy resolution.

Figure 3(a) plots RIXS spectra after the subtraction of elastic scattering for momentum integrated from $q_{\parallel} = 0.22$ to $q_{\parallel} = 0.25$ at different temperatures. This low-energy RIXS intensity decreases when the temperature is increased as plotted in Fig. 3(b). On comparing the intensity, spectral profile, and peak energy of the low-energy RIXS excitation near 14 meV with those of calculated $S(\mathbf{q}_{\mathrm{CDW}}, \omega)$, in which the contribution of the dispersion parameter c vanishes, one can obtain the evolution of Δ and Γ_{CDW} for various temperatures. Figures 3(c) and 3(d) show the estimated temperature-dependent Δ and Γ_{CDW}, respectively. The evolution of Δ, which is inversely proportional to the CDW correlation length [36], is accordant with the temperature dependence of static charge order shown in Fig. 1. At low temperatures, Γ_{CDW} grows with increasing temperature. In the quantum critical regime, the scattering rate of

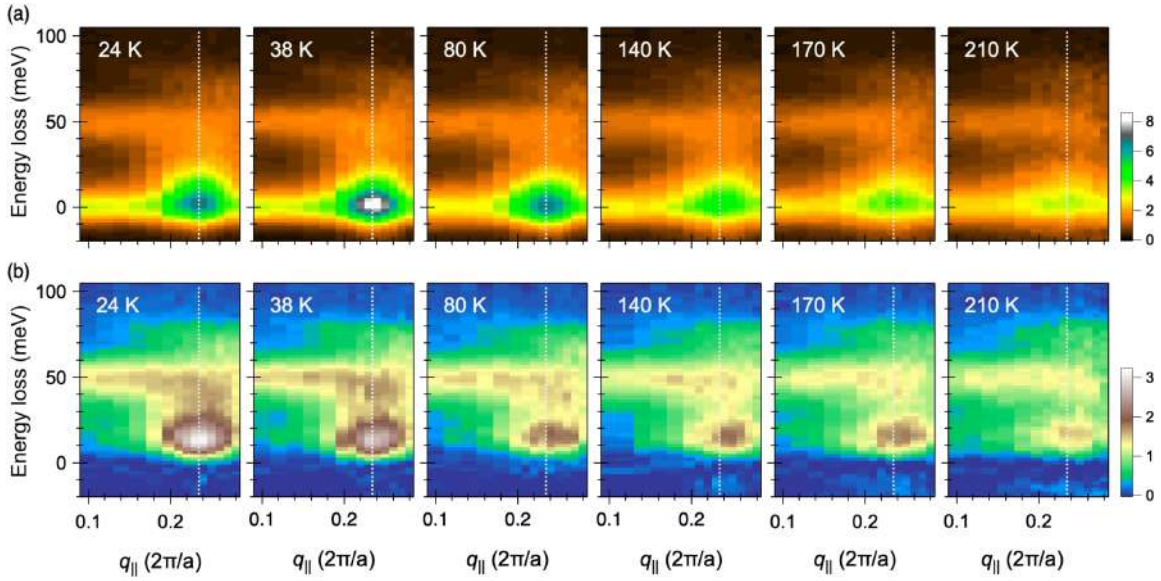

FIG. 2. Temperature dependent O K edge RIXS of optimally doped LSCO. (a) RIXS intensity distribution maps in the plane of energy loss vs in plane momentum transfer $\mathbf{q}_{\|}$ along $(\pi, 0)$ at various temperatures. (b) RIXS intensity distribution maps after the subtraction of elastic scattering. All RIXS spectra are recorded with σ polarized incident x rays of energy tuned to the ZRS hole. The momentum transfer is $\mathbf{q} = (q_{\|}, 0, L)$ with L varying between 0.47 and 1.03 in reciprocal lattice units. Dotted lines indicate the position of measured $\mathbf{q}_{\mathrm{CDW}} = (0.23, 0, L)$.

quasiparticles reaches the Planckian limit, and the change of Γ_{CDW} is comparable with $k_B T/\hbar$, i.e., the Planckian dissipation [40,52]. Although the measured data cover only one temperature point below T_C, this observation supports the quantum critical nature of CDW fluctuations in LSCO.

Figure 3(d) also shows that, as T is increased, the temperature dependence of Γ_{CDW} exhibits a bending feature about 80 K. This suggests two possible scenarios: a crossover near the QCP and the coupling of CDW fluctuations to acoustic phonons. First, a crossover of Γ_{CDW} behavior near the QCP [53,54] indicates that Planckian linear-T dependence works only at the critical regime (low-temperature regions) controlled by the QCP. In other words, only inside the critical regime, Γ_{CDW} shows the linear-T dependence, which reflects the gapless nature at the QCP, i.e., $1/\Gamma_{\mathrm{CDW}}$ going to infinity. At higher temperatures beyond the critical regime, Γ_{CDW} no longer reaches the Planckian limit. In this scenario, the quantum critical region is up to approximately 80 K. In the second scenario, the bending feature of Γ_{CDW} suggests that, for the thermal energy $k_B T$ comparable to the charge fluctuation energy, CDW fluctuations alone do not explain the RIXS data at high temperatures, as shown in supplemental Figs. S8(e)–S8(g) [47]. This indicates that the low-energy RIXS is also contributed by the coupling of CDW fluctuations to phonons. We, hence, calculate the full RIXS intensity using a diagrammatic framework, in which the coupling between χ_{CDW} and phonons renormalizes the phonon propagator.

III. RIXS CALCULATIONS

The intensity of the phonon excitations is calculated by using the diagrammatic framework [55] generalized to the O K edge. The RIXS intensity is given by ($\hbar = 1$)

$$
\begin{aligned}
I_\nu(\mathbf{q},\Omega) = {} & \frac{1}{N}\sum_{\mathbf{k},\alpha}\frac{1}{N}\sum_{\mathbf{k}',\beta}[\hat{\boldsymbol{\epsilon}}_i\cdot\hat{\mathbf{r}}_\alpha][\hat{\boldsymbol{\epsilon}}_f\cdot\hat{\mathbf{r}}_\beta]g_\nu(\mathbf{k},\mathbf{k}+\mathbf{q})|\phi_{2p_\alpha}(\mathbf{k})|^2|\phi_{2p_\beta}(\mathbf{k}+\mathbf{q})|^2\left[\frac{n_f(-\epsilon_{\mathbf{k}})}{\epsilon_{\mathbf{k}}-\omega_f-E_{1s,2p}-i\Gamma}-\frac{n_f(-\epsilon_{\mathbf{k}+\mathbf{q}})}{\epsilon_{\mathbf{k}+\mathbf{q}}-\omega_i-E_{1s,2p}-i\Gamma}\right] \\
& \times g_\nu(\mathbf{k}'+\mathbf{q},\mathbf{k}')|\phi_{2p_\beta}(\mathbf{k}')|^2|\phi_{2p_\alpha}(\mathbf{k}'+\mathbf{q})|^2\left[\frac{n_f(-\epsilon_{\mathbf{k}'})}{\epsilon_{\mathbf{k}'}-\omega_f-E_{1s,2p}+i\Gamma}-\frac{n_f(-\epsilon_{\mathbf{k}'+\mathbf{q}})}{\epsilon_{\mathbf{k}'+\mathbf{q}}-\omega_i-E_{1s,2p}+i\Gamma}\right] \\
& \times -\frac{1}{\pi}\mathrm{Im}\left\{\frac{1}{\epsilon_{\mathbf{k}}-\epsilon_{\mathbf{k}+\mathbf{q}}+\Omega+i\gamma_e}D_\nu(\mathbf{q},\Omega)\frac{1}{\epsilon_{\mathbf{k}'}-\epsilon_{\mathbf{k}'+\mathbf{q}}+\Omega-i\gamma_e}\right\}. \qquad (3)
\end{aligned}
$$

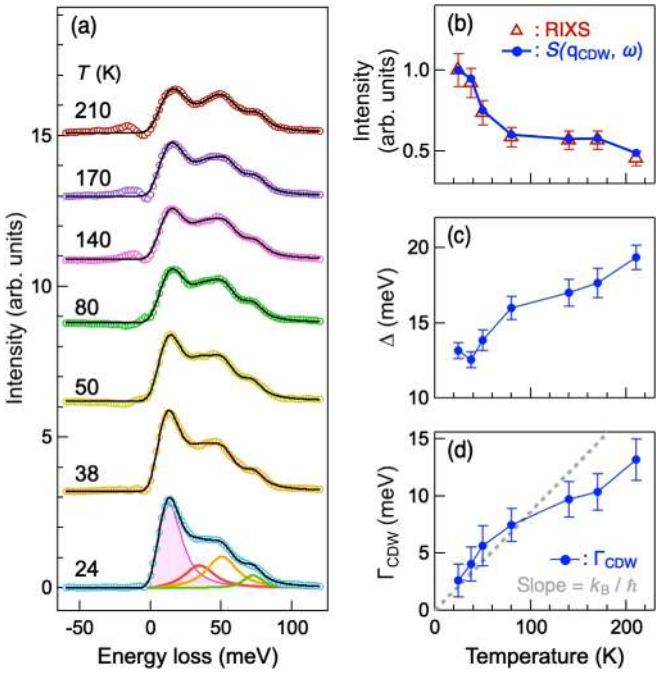

FIG. 3. Temperature dependence of CDW fluctuations. (a) Momentum integrated RIXS spectra after the subtraction of elastic scattering and then momentum integration over a range from 0.22 to 0.25 in units of $2\pi/a$ at different temperatures. The RIXS spectra are fitted to four phonon modes. The component derived from the coupling of CDW fluctuations to acoustic phonons is shaded in pink. The components of the BS, A_{1g}, and B_{1g} phonon modes are shown in green, orange, and red, respectively. Details of the curve fitting are presented in Supplemental Material [47]. (b) RIXS peak intensity of the 14 meV component shown in (a), compared to the maximum of calculated $S(\mathbf{q}_{\mathrm{CDW}},\omega)$ after convolution with the instrumental resolution. The value of $S(\mathbf{q}_{\mathrm{CDW}},\omega)$ with the 24 K data point is normalized to the RIXS intensity. Values of Δ and Γ_{CDW} used for the $S(\mathbf{q}_{\mathrm{CDW}},\omega)$ calculations are plotted in (c) and (d), respectively. (d) Temperature dependence of Γ_{CDW}. The gray dashed line indicates the slope of the lifetime width vs T determined by the limit of the Planckian dissipation. All solid lines connecting data points in (b) (d) serve as visual guidance.

Here, $n_f(x)$ is the Fermi factor; $\epsilon_{\mathbf{k}}$ is the electron band dispersion; $g_\nu(\mathbf{k},\mathbf{q})$ and $D_\nu(\mathbf{q},\xi)$ are the electron-phonon vertex and phonon propagators for phonon branch ν, respectively; $\phi_{2p_\alpha}(\mathbf{k})$ is the oxygen $2p_\alpha$ orbital character of the band; $\hat{\mathbf{r}}_\alpha$ is a unit vector pointing along the direction of the oxygen orbital; Γ is the core-hole lifetime parameter; γ_e is a lifetime parameter for the electrons; and $\Omega = \omega_i - \omega_f$ and $\mathbf{q} = \mathbf{k}_i - \mathbf{k}_f$ are the energy and momentum, respectively, transferred to the sample. The phonon softening is determined by the total electronic polarizability. Our model essentially assumes that the phonons respond to some strong CDW fluctuation caused by an external source like correlations. That is, the coupling of CDW fluctuations to phonons renormalizes the phonon propagator through charge susceptibility $\chi_{\mathrm{CDW}}(\mathbf{q}_\parallel,\omega)$. See Supplemental Material [47] for the calculation details.

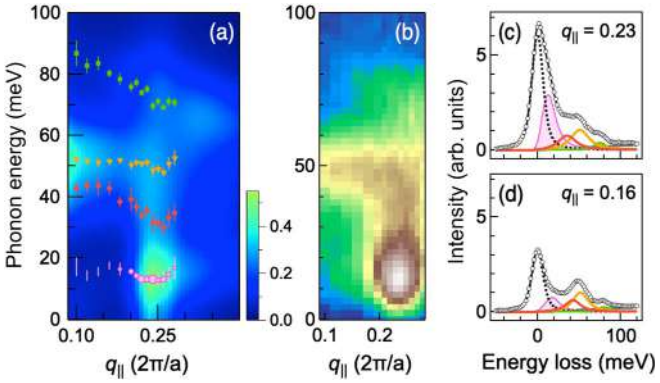

FIG. 4. Phonon excitations from RIXS measurements of optimally doped LSCO. (a) Calculated intensity distribution map using the diagrammatic framework in comparison with phonon dispersions obtained from RIXS spectra of 24 K. Green squares, orange triangles, and red diamonds depict the dispersions of BS, A_{1g}, and B_{1g} phonon modes, respectively. The dispersions of the low energy RIXS excitations are represented by pink circles scaled to the fitted intensity. (b) RIXS intensity distribution map of $T = 24$ K extracted from Fig. 2(b) and plotted with the same color scale. (c),(d) Measured RIXS spectra with fitted components for phonon excitations of momenta $q_\parallel = 0.23$ and 0.16 at $T = 24$ K, respectively. The curve fitting scheme is the same as that in Fig. 3(a). RIXS data are plotted as open circles with black curves to show the summation of fitted components and a linear background. The component derived from the coupling of CDW fluctuations to acoustic and optical phonons is shaded in pink. The components of the BS, A_{1g}, and B_{1g} phonon modes are shown in green, orange, and red, respectively. The elastic component is plotted as a dashed curve.

Figure 4(a) presents the calculated RIXS intensity distribution map. That the coupling of CDW fluctuations to acoustic phonons enhances the RIXS intensity significantly at 14 meV for momentum about $\mathbf{q}_{\mathrm{CDW}}$ agrees satisfactorily well with the measurements shown in Fig. 4(b), corroborating the phenomenological form of charge susceptibility given in Eq. (2).

IV. ELECTRON-PHONON COUPLING

In addition to the pronounced low-energy feature, RIXS also measures other phonon excitations [55,56]. The electron-phonon coupling involved with states near the Fermi level is weak for the apical mode [57]. The contribution of apical phonons to RIXS can be neglected. We, therefore, fit RIXS spectra with three components for high-energy phonons, i.e., bond-stretching (BS), A_{1g} buckling, and B_{1g} buckling phonons [30,32,58–60], as shown in Figs. 4(c) and 4(d), which plot fitting spectra of $q_\parallel = 0.23$ and 0.16 at 24 K, respectively. Results of other $q_\parallel$ and temperatures are presented in Figs. S9–S11 in Supplemental Material [47]. Figure 4(a) also depicts the phonon dispersions from curve fitting. The diagrammatic

calculations explain well the observed photon softening. In addition to phonon softening, the phonon energies from RIXS agree with those are from density-functional-theory (DFT) calculations [30] and measurements of Raman scattering [59], inelastic neutron scattering [58], IXS [28], and photoemission [60]. We also fit the RIXS data of $T = 24$ K with three phonon modes, i.e., BS, buckling, and acoustic phonons; the fitting results plotted in supplemental Fig. S12 [47] show a phonon softening consistent with that from the four-phonon fitting. That is, our curve fitting results show that these phonons all exhibit the strongest softening at $\mathbf{q}_{\parallel} = (0.25, 0)$ rather than $\mathbf{q}_{\mathrm{CDW}}$, supporting the scenario of discommensurate CDWs in LSCO at doping level $x = 0.15$. In domains of discommensurate CDWs, phonons are strongly coupled to charge fluctuations, and the phase shift between scattered x rays from separate domains is negligible. The phonon softening, therefore, occurs at $\mathbf{q}_{\parallel} = (0.25, 0)$ for CDW domains of period $4a$, in which a is the in-plane lattice constant.

To further understand the characteristics of CDWs in LSCO, we examine the coupling of CDWs to phonons through performing DFT calculations in the scheme of frozen phonons, which are adopted to study qualitatively the coupling of longitudinal BS mode and apical phonon mode of A_{1g} symmetry with a periodicity of $4a$. See Supplemental Material [47] for the details. The calculations show that the apical mode has an energy lower than that of the BS mode. Whereas the vibration of either the apical or the BS mode raises the total energy, the vibrations of these two modes together produce an energy gain for the CDW state as compared with the vibration of each single mode. This energy gain indicates that the coupling of these two phonon modes with CDWs is favorable; the coupling strength, measured by the energy gain, is found to be stronger than that with other periodicities, such as $6a$. The coupling strength also enhances with increasing hole concentrations. These findings are in agreement with the RIXS results that strong phonon softening occurs about $q_{\parallel} = 0.25$. One plausible scenario is that the CDW has effectively a period $4a$ and is short ranged [51]; a shift in the wave vector of a large sample appears in the Fourier space, giving rise to the formation of discommensurate CDWs.

V. DISCUSSION AND CONCLUSION

Although the data presented in the present work are only from a sample near the optimal doping, quantum critical scalings of charge fluctuations in the temperature domain are clearly demonstrated. These results are consistent with the speculation on the existence of a QCP. On the other hand, by suppressing superconductivity in high magnetic fields, linear scalings in resistivity are observed in a more extended regime around the putative QCP near a doping level of 0.2 [39]. While the extended linear-resistivity region shows quantum scaling in temperature, it does not exhibit the quantum critical scaling in the nonthermal parameter, doping. Thus, the correspondence between quantum criticality and T-linear resistivity may not be of necessity [61,62]. The apparent extended critical region that is overlapped with the putative QCP may just be a non-Fermi-liquid phase [63]. In this scenario, the CDW phase becomes a non-Fermi-liquid phase as the doping level is tuned across the putative QCP. Clearly, to clarify these issues, future work on samples (both LSCO and Nd-LSCO) with different dopings around the critical point and inside the region of long-range charge-ordered phase (Nd-LSCO sample) is required in order to unequivocally prove the existence of QCP related to charge order in LSCO.

In conclusion, we observe short-range CDWs in LSCO near the optimal doping over a wide temperature range; these orders compete locally with the superconducting order. Through combining high-resolution RIXS measurements, theoretical modeling, and diagrammatic calculations, our results provide evidence for phonon softening in superconducting cuprates induced by charge order. The observation of phonon softening indeed results from quantum fluctuations of the charge order.

ACKNOWLEDGMENTS

We thank Wei-Sheng Lee and Alfred Baron for useful discussions. We thank Peter Towei Huang for making graphic illustrations. This work was supported in part by the Ministry of Science and Technology of Taiwan under Grants No. 109-2112-M-213-010-MY3 and No. 109-2923-M-213-001. S. J. acknowledges support from the National Science Foundation under Grant No. DMR-1842056. A. F. K. acknowledges support from the National Science Foundation under Grant No. DMR-1752713. We also thank the support by KAKENHI Grant No. 19K03741 from JSPS and Program for Promoting Researches on the Supercomputer Fugaku (Basic Science for Emergence and Functionality in Quantum Matter JPMXP-1020200104) from MEXT.

[1] B. Keimer, S. A. Kivelson, M. R. Norman, S. Uchida, and J. Zaanen, *From Quantum Matter to High Temperature Superconductivity in Copper Oxides*, Nature (London) **518**, 179 (2015).

[2] E. Fradkin, S. A. Kivelson, and J. M. Tranquada, *Colloquium: Theory of Intertwined Orders in High Temperature Superconductors*, Rev. Mod. Phys. **87**, 457 (2015).

[3] G. Ghiringhelli, M. Le Tacon, M. Minola, S. Blanco Canosa, C. Mazzoli, N. B. Brookes, G. M. De Luca, A. Frano, D. G. Hawthorn, F. He, T. Loew, M. M. Sala, D. C. Peets, M. Salluzzo, E. Schierle, R. Sutarto, G. A. Sawatzky, E. Weschke, B. Keimer, and L. Braicovich, *Long Range Incommensurate Charge Fluctuations in* $(Y, \mathrm{Nd})\mathrm{Ba}_2\mathrm{Cu}_3\mathrm{O}_{6+x}$, Science **337**, 821 (2012).

[4] E. Blackburn, J. Chang, M. Hücker, A. T. Holmes, N. B. Christensen, R. Liang, D. A. Bonn, W. N. Hardy, U. Rütt, O. Gutowski, M. v. Zimmermann, E. M. Forgan, and S. M. Hayden, *X Ray Diffraction Observations of a Charge Density Wave Order in Superconducting Ortho II* $YBa_2Cu_3O_{6.54}$ *Single Crystals in Zero Magnetic Field*, Phys. Rev. Lett. **110**, 137004 (2013).

[5] T. P. Croft, C. Lester, M. S. Senn, A. Bombardi, and S. M. Hayden, *Charge Density Wave Fluctuations in* $La_{2-x}Sr_xCuO_4$ *and Their Competition with Superconductivity*, Phys. Rev. B **89**, 224513 (2014).

[6] X. Zhu, Y. Cao, J. Zhang, E. W. Plummer, and J. Guo, *Classification of Charge Density Waves Based on Their Nature*, Proc. Natl. Acad. Sci. U.S.A. **112**, 2367 (2015).

[7] R. Comin and A. Damascelli, *Resonant X Ray Scattering Studies of Charge Order in Cuprates*, Annu. Rev. Condens. Matter Phys. **7**, 369 (2016).

[8] H. Miao, R. Fumagalli, M. Rossi, J. Lorenzana, G. Seibold, F. Yakhou Harris, K. Kummer, N. B. Brookes, G. D. Gu, L. Braicovich, G. Ghiringhelli, and M. P. M. Dean, *Formation of Incommensurate Charge Density Waves in Cuprates*, Phys. Rev. X **9**, 031042 (2019).

[9] J. J. Wen, H. Huang, S. J. Lee, H. Jang, J. Knight, Y. S. Lee, M. Fujita, K. M. Suzuki, S. Asano, S. A. Kivelson, C. C. Kao, and J. S. Lee, *Observation of Two Types of Charge Density Wave Orders in Superconducting* $La_{2-x}Sr_xCuO_4$, Nat. Commun. **10**, 3269 (2019).

[10] R. Arpaia, S. Caprara, R. Fumagalli, G. De Vecchi, Y. Y. Peng, E. Andersson, D. Betto, G. M. De Luca, N. B. Brookes, F. Lombardi, M. Salluzzo, L. Braicovich, C. Di Castro, M. Grilli, and G. Ghiringhelli, *Dynamical Charge Density Fluctuations Pervading the Phase Diagram of a Cu Based High Tc Superconductor*, Science **365**, 906 (2019).

[11] M. Mitrano, S. Lee, A. A. Husain, L. Delacretaz, M. Zhu, G. de la Peña Munoz, S. X. L. Sun, Y. I. Joe, A. H. Reid, S. F. Wandel, G. Coslovich, W. Schlotter, T. van Driel, J. Schneeloch, G. D. Gu, S. Hartnoll, N. Goldenfeld, and P. Abbamonte, *Ultrafast Time Resolved X Ray Scattering Reveals Diffusive Charge Order Dynamics in* $La_{2-x}Ba_xCuO_4$, Sci. Adv. **5**, eaax3346 (2019).

[12] D. H. Torchinsky, F. Mahmood, A. T. Bollinger, I. Božović, and N. Gedik, *Fluctuating Charge Density Waves in a Cuprate Superconductor*, Nat. Mater. **12**, 387 (2013).

[13] R. Comin, A. Frano, M. M. Yee, Y. Yoshida, H. Eisaki, E. Schierle, E. Weschke, R. Sutarto, F. He, A. Soumyanarayanan, Y. He, M. Le Tacon, I. S. Elfimov, J. E. Hoffman, G. A. Sawatzky, B. Keimer, and A. Damascelli, *Charge Order Driven by Fermi Arc Instability in* $Bi_2Sr_{2-x}La_xCuO_{6+\delta}$, Science **343**, 390 (2014).

[14] W. Tabis, Y. Li, M. Le Tacon, L. Braicovich, A. Kreyssig, M. Minola, G. Dellea, E. Weschke, M. J. Veit, M. Ramazanoglu, A. I. Goldman, T. Schmitt, G. Ghiringhelli, N. Barišić, M. K. Chan, C. J. Dorow, G. Yu, X. Zhao, B. Keimer, and M. Greven, *Charge Order and Its Connection with Fermi Liquid Charge Transport in a Pristine High Tc Cuprate*, Nat. Commun. **5**, 5875 (2014).

[15] E. H. da Silva Neto, R. Comin, F. He, R. Sutarto, Y. Jiang, R. L. Greene, G. A. Sawatzky, and A. Damascelli, *Charge Ordering in the Electron Doped Superconductor* $Nd_{2-x}Ce_xCuO_4$, Science **347**, 282 (2015).

[16] G. Campi, A. Bianconi, N. Poccia, G. Bianconi, L. Barba, G. Arrighetti, D. Innocenti, J. Karpinski, N. D. Zhigadlo, S. M. Kazakov, M. Burghammer, M. v. Zimmermann, M. Sprung, and A. Ricci, *Inhomogeneity of Charge Density Wave Order and Quenched Disorder in a High Tc Superconductor*, Nature (London) **525**, 359 (2015).

[17] S. Gerber *et al.*, *Three Dimensional Charge Density Wave Order in* $YBa_2Cu_3O_{6.67}$ *at High Magnetic Fields*, Science **350**, 949 (2015).

[18] Y. Y. Peng, R. Fumagalli, Y. Ding, M. Minola, S. Caprara, D. Betto, M. Bluschke, G. M. De Luca, K. Kummer, E. Lefrançois, M. Salluzzo, H. Suzuki, M. Le Tacon, X. J. Zhou, N. B. Brookes, B. Keimer, L. Braicovich, M. Grilli, and G. Ghiringhelli, *Re entrant Charge Order in Overdoped* $(Bi,Pb)_{2.12}Sr_{1.88}CaCuO_{6+\delta}$ *outside the Pseudogap Regime*, Nat. Mater. **17**, 697 (2018).

[19] H. H. Kim, S. M. Souliou, M. E. Barber, E. Lefrançois, M. Minola, M. Tortora, R. Heid, N. Nandi, R. A. Borzi, G. Garbarino, A. Bosak, J. Porras, T. Loew, M. König, P. J. W. Moll, A. P. Mackenzie, B. Keimer, C. W. Hicks, and M. Le Tacon, *Uniaxial Pressure Control of Competing Orders in a High Temperature Superconductor*, Science **362**, 1040 (2018).

[20] X. M. Chen, C. Mazzoli, Y. Cao, V. Thampy, A. M. Barbour, W. Hu, M. Lu, T. A. Assefa, H. Miao, G. Fabbris, G. D. Gu, J. M. Tranquada, M. P. M. Dean, S. B. Wilkins, and I. K. Robinson, *Charge Density Wave Memory in a Cuprate Superconductor*, Nat. Commun. **10**, 1435 (2019).

[21] B. Yu, W. Tabis, I. Bialo, F. Yakhou, N. B. Brookes, Z. Anderson, Y. Tang, G. Yu, and M. Greven, *Unusual Dynamic Charge Correlations in Simple Tetragonal* $HgBa_2Cu_2O_{4+\delta}$, Phys. Rev. X **10**, 021059 (2020).

[22] L. Chaix, G. Ghiringhelli, Y. Y. Peng, M. Hashimoto, B. Moritz, K. Kummer, N. B. Brookes, Y. He, S. Chen, S. Ishida, Y. Yoshida, H. Eisaki, M. Salluzzo, L. Braicovich, Z. X. Shen, T. P. Devereaux, and W. S. Lee, *Dispersive Charge Density Wave Excitations in* $Bi_2Sr_2CaCu_2O_{8+\delta}$, Nat. Phys. **13**, 952 (2017).

[23] W. S. Lee, K. J. Zhou, M. Hepting, J. Li, A. Nag, A. C. Walters, M. Garcia Fernandez, H. C. Robarts, M. Hashimoto, H. Lu, B. Nosarzewski, D. Song, H. Eisaki, Z. X. Shen, B. Moritz, J. Zaanen, and T. P. Devereaux, *Spectroscopic Fingerprint of Charge Order Melting Driven by Quantum Fluctuations in a Cuprate*, Nat. Phys. **17**, 53 (2021).

[24] J. Q. Lin, H. Miao, D. G. Mazzone, G. D. Gu, A. Nag, A. C. Walters, M. García Fernández, A. Barbour, J. Pelliciari, I. Jarrige, M. Oda, K. Kurosawa, N. Momono, K. J. Zhou, V. Bisogni, X. Liu, and M. P. M. Dean, *Strongly Correlated Charge Density Wave in* $La_{2-x}Sr_xCuO_4$ *Evidenced by Doping Dependent Phonon Anomaly*, Phys. Rev. Lett. **124**, 207005 (2020).

[25] J. Li, A. Nag, J. Pelliciari, H. Robarts, A. Walters, M. Garcia Fernandez, H. Eisaki, D. Song, H. Ding, S. Johnston, R. Comin, and K. J. Zhou, *Multiorbital Charge Density Wave Excitations and Concomitant Phonon Anomalies in* $Bi_2Sr_2LaCuO_{6+\delta}$, Proc. Natl. Acad. Sci. U.S.A. **117**, 16219 (2020).

[26] C. Castellani, C. Di Castro, and M. Grilli, *Singular Quasiparticle Scattering in the Proximity of Charge Instabilities*, Phys. Rev. Lett. **75**, 4650 (1995).

[27] F. Becca, M. Tarquini, M. Grilli, and C. Di Castro, *Charge Density Waves and Superconductivity as an Alternative to Phase Separation in the Infinite U Hubbard Holstein Model*, Phys. Rev. B **54**, 12443 (1996).

[28] T. Fukuda, J. Mizuki, K. Ikeuchi, K. Yamada, A. Q. R. Baron, and S. Tsutsui, *Doping Dependence of Softening in the Bond Stretching Phonon Mode of* $La_{2-x}Sr_xCuO_4$ *(*$0 \leq x \leq 0.29$*)*, Phys. Rev. B **71**, 060501(R) (2005).

[29] D. Reznik, L. Pintschovius, M. Ito, S. Iikubo, M. Sato, H. Goka, M. Fujita, K. Yamada, G. D. Gu, and J. M. Tranquada, *Electron Phonon Coupling Reflecting Dynamic Charge Inhomogeneity in Copper Oxide Superconductors*, Nature (London) **440**, 1170 (2006).

[30] F. Giustino, M. L. Cohen, and S. G. Louie, *Small Phonon Contribution to the Photoemission Kink in the Copper Oxide Superconductors*, Nature (London) **452**, 975 (2008).

[31] M. Le Tacon, A. Bosak, S. M. Souliou, G. Dellea, T. Loew, R. Heid, K. P. Bohnen, G. Ghiringhelli, M. Krisch, and B. Keimer, *Inelastic X Ray Scattering in* $YBa_2Cu_3O_{6.6}$ *Reveals Giant Phonon Anomalies and Elastic Central Peak due to Charge Density Wave Formation*, Nat. Phys. **10**, 52 (2014).

[32] S. R. Park, T. Fukuda, A. Hamann, D. Lamago, L. Pintschovius, M. Fujita, K. Yamada, and D. Reznik, *Evidence for a Charge Collective Mode Associated with Superconductivity in Copper Oxides from Neutron and X Ray Scattering Measurements of* $La_{2-x}Sr_xCuO_4$, Phys. Rev. B **89**, 020506(R) (2014).

[33] H. Miao, G. Fabbris, R. J. Koch, D. G. Mazzone, C. S. Nelson, R. Acevedo Esteves, G. D. Gu, Y. Li, T. Yilimaz, K. Kaznatcheev, E. Vescovo, M. Oda, T. Kurosawa, N. Momono, T. Assefa, I. K. Robinson, E. S. Bozin, J. M. Tranquada, P. D. Johnson, and M. P. M. Dean, *Charge Density Waves in Cuprate Superconductors beyond the Critical Doping*, npj Quantum Mater. **6**, 31 (2021).

[34] S. Sachdev, *Where Is the Quantum Critical Point in the Cuprate Superconductors?*, Phys. Status Solidi (b) **247**, 537 (2010).

[35] S. Sachdev, *Quantum Phase Transitions*, 2nd ed. (Cambridge University Press, Cambridge, Englandm 2011).

[36] S. Caprara, C. Di Castro, G. Seibold, and M. Grilli, *Dynamical Charge Density Waves Rule the Phase Diagram of Cuprates*, Phys. Rev. B **95**, 224511 (2017).

[37] C. Proust and L. Taillefer, *The Remarkable Underlying Ground States of Cuprate Superconductors*, Annu. Rev. Condens. Matter Phys. **10**, 409 (2019).

[38] B. Michon, C. Girod, S. Badoux, J. Kačmarčík, Q. Ma, M. Dragomir, H. A. Dabkowska, B. D. Gaulin, J. S. Zhou, S. Pyon, T. Takayama, H. Takagi, S. Verret, N. Doiron Leyraud, C. Marcenat, L. Taillefer, and T. Klein, *Thermodynamic Signatures of Quantum Criticality in Cuprate Superconductors*, Nature (London) **567**, 218 (2019).

[39] R. Cooper, Y. Wang, B. Vignolle, O. Lipscombe, S. Hayden, Y. Tanabe, T. Adachi, Y. Koike, M. Nohara, H. Takagi, C. Proust, and N. E. Hussey, *Anomalous Criticality in the Electrical Resistivity of* $La_{2-x}Sr_xCuO_4$, Science **323**, 603 (2009).

[40] A. Legros, S. Benhabib, W. Tabis, F. Laliberté, M. Dion, M. Lizaire, B. Vignolle, D. Vignolles, H. Raffy, Z. Z. Li, P. Auban Senzier, N. Doiron Leyraud, P. Fournier, D. Colson, L. Taillefer, and C. Proust, *Universal T Linear Resistivity and Planckian Dissipation in Overdoped Cuprates*, Nat. Phys. **15**, 142 (2019).

[41] L. J. P. Ament, M. van Veenendaal, T. P. Devereaux, J. P. Hill, and J. van den Brink, *Resonant Inelastic X Ray Scattering Studies of Elementary Excitations*, Rev. Mod. Phys. **83**, 705 (2011).

[42] C. Jia, K. Wohlfeld, Y. Wang, B. Moritz, and T. P. Devereaux, *Using RIXS to Uncover Elementary Charge and Spin Excitations*, Phys. Rev. X **6**, 021020 (2016).

[43] S. Komiya, Y. Ando, X. F. Sun, and A. N. Lavrov, *c Axis Transport and Resistivity Anisotropy of Lightly to Moderately Doped* $La_{2-x}Sr_xCuO_4$ *Single Crystals: Implications on the Charge Transport Mechanism*, Phys. Rev. B **65**, 214535 (2002).

[44] S. Komiya, H. D. Chen, S. C. Zhang, and Y. Ando, *Magic Doping Fractions for High Temperature Superconductors*, Phys. Rev. Lett. **94**, 207004 (2005).

[45] S. Ono, S. Komiya, and Y. Ando, *Strong Charge Fluctuations Manifested in the High Temperature Hall Coefficient of High* T_c *Cuprates*, Phys. Rev. B **75**, 024515 (2007).

[46] A. Singh *et al.*, *Development of the Soft X Ray AGM AGS RIXS Beamline at the Taiwan Photon Source*, J. Synchrotron Radiat. **28**, 977 (2021).

[47] See Supplemental Material at http://link.aps.org/supplemental/10.1103/PhysRevX.11.041038 for sample characterizations, RIXS setup, calculations, and data analysis.

[48] W. L. McMillan, *Theory of Discommensurations and the Commensurate Incommensurate Charge Density Wave Phase Transition*, Phys. Rev. B **14**, 1496 (1976).

[49] C. H. Chen, J. M. Gibson, and R. M. Fleming, *Direct Observation of Charge Density Wave Discommensurations and Dislocations in* $2H$ $TaSe_2$, Phys. Rev. Lett. **47**, 723 (1981).

[50] W. L. Tu and T. K. Lee, *Evolution of Pairing Orders between Pseudogap and Superconducting Phases of Cuprate Superconductors*, Sci. Rep. **9**, 1719 (2019).

[51] A. Mesaros, K. Fujita, S. D. Edkins, M. H. Hamidian, H. Eisaki, S. i. Uchida, J. C. S. Davis, M. J. Lawler, and E. A. Kim, *Commensurate* $4a_0$ *Period Charge Density Modulations throughout the* $Bi_2Sr_2CaCu_2O_{8+x}$ *Pseudogap Regime*, Proc. Natl. Acad. Sci. U.S.A. **113**, 12661 (2016).

[52] J. Zaanen, *Why the Temperature is High*, Nature (London) **430**, 512 (2004).

[53] S. Chakravarty, B. I. Halperin, and D. R. Nelson, *Two Dimensional Quantum Heisenberg Antiferromagnet at Low Temperatures*, Phys. Rev. B **39**, 2344 (1989).

[54] S. Chakravarty, *Quantum Critical Fluctuations, Planckian Dissipation, and Compactification Scale*, arXiv:1907.12163.

[55] T. P. Devereaux, A. M. Shvaika, K. Wu, K. Wohlfeld, C. J. Jia, Y. Wang, B. Moritz, L. Chaix, W. S. Lee, Z. X. Shen, G. Ghiringhelli, and L. Braicovich, *Directly Characterizing the Relative Strength and Momentum Dependence of*

Electron Phonon Coupling Using Resonant Inelastic X Ray Scattering, Phys. Rev. X **6**, 041019 (2016).

[56] L. J. P. Ament, M. van Veenendaal, and J. van den Brink, *Determining the electron phonon coupling strength from Resonant Inelastic X ray Scattering at transition metal L edges*, Europhys. Lett. **95**, 27008 (2011).

[57] S. Johnston, F. Vernay, B. Moritz, Z. X. Shen, N. Nagaosa, J. Zaanen, and T. P. Devereaux, *Systematic Study of Elec tron Phonon Coupling to Oxygen Modes across the Cup rates*, Phys. Rev. B **82**, 064513 (2010).

[58] R. J. McQueeney, Y. Petrov, T. Egami, M. Yethiraj, G. Shirane, and Y. Endoh, *Anomalous Dispersion of LO Phonons in* $La_{1.85}Sr_{1.5}CuO_4$ *at Low Temperatures*, Phys. Rev. Lett. **82**, 628 (1999).

[59] S. Sugai, Y. Takayanagi, N. Hayamizu, T. Muroi, R. Shiozaki, J. Nohara, K. Takenaka, and K. Okazaki, *Super conducting Pairing and the Pseudogap in the Nematic Dynamical Stripe Phase of* $La_{2-x}Sr_xCuO_4$, J. Phys. Con dens. Matter **25**, 475701 (2013).

[60] X. J. Zhou *et al.*, *Multiple Bosonic Mode Coupling in the Electron Self Energy of* $La_{2-x}Sr_xCuO_4$, Phys. Rev. Lett. **95**, 117001 (2005).

[61] Y. Ando, S. Komiya, K. Segawa, S. Ono, and Y. Kurita, *Electronic Phase Diagram of High* T_c *Cuprate Superconductors from a Mapping of the In Plane Resistivity Curvature*, Phys. Rev. Lett. **93**, 267001 (2004).

[62] P. Phillips and C. Chamon, *Breakdown of One Parameter Scaling in Quantum Critical Scenarios for High Temper ature Copper Oxide Superconductors*, Phys. Rev. Lett. **95**, 107002 (2005).

[63] N. Doiron Leyraud, I. Walker, L. Taillefer, M. Steiner, S. Julian, and G. Lonzarich, *Fermi Liquid Breakdown in the Paramagnetic Phase of a Pure Metal*, Nature (London) **425**, 595 (2003).

npj | Quantum Materials

www.nature.com/npjquantmats

ARTICLE OPEN

Resonant inelastic X-ray scattering as a probe of $J_{\mathrm{eff}} = 1/2$ state in 3*d* transition-metal oxide

H. Y. Huang[1], A. Singh[1], C. I. Wu[2], J. D. Xie[3], J. Okamoto[1], A. A. Belik[4], E. Kurmaev[5], A. Fujimori[1,6], C. T. Chen[1], S. V. Streltsov[5,7]✉ and D. J. Huang[1,3,8]✉

The state with effective total moment $J_{\mathrm{eff}} = 1/2$ stabilized by the spin-orbit coupling is known to suppress Jahn-Teller distortions and may induce a strong exchange anisotropy. This in turn may lead to the formation of an elusive spin-liquid state in real materials. While recent studies have demonstrated that such a situation can be realized in 3*d* transition-metal compounds such as those based on Co^{2+} and Cu^{2+}, diagnosis of $J_{\mathrm{eff}} = 1/2$ state remains challenging. We show that resonant inelastic X-ray scattering is an effective tool to probe this state and apply it to $CuAl_2O_4$, material where Cu^{2+} ions were previously proposed to be in the $J_{\mathrm{eff}} = 1/2$ state. Our results unambiguously demonstrate that, contrary to previous expectations, a competitive (to $J_{\mathrm{eff}} = 1/2$) Jahn-Teller state realizes in this compound.

npj Quantum Materials (2022)7:33 ; https://doi.org/10.1038/s41535-022-00430-0

INTRODUCTION

Spin-orbit materials, i.e., systems in which physical properties are strongly affected by the spin-orbit coupling (SOC), undoubtedly became one of the central subjects in modern condensed matter physics[1,2]. In particular, it is essential for various topological effects and anisotropic exchange interaction in magnetic materials, which may result, e.g., in a mysterious Kitaev quantum spin liquid[3,4]. Since the SOC constant is large for heavy elements[5], the investigations were initially concentrated on the 4*d* and 5*d* transition-metal compounds such as α $RuCl_3$ and $(Li,Na)_2IrO_3$[4,6,7]. However, it was very recently shown that more conventional 3*d* oxides also can demonstrate similar behavior with the ground state characterized by an effective moment $J_{\mathrm{eff}} = 1/2$ (New is often well overlooked old.)[8,9].

Indeed, the spin-orbital entangled state can be realized, for example, in the case of Co^{2+} ions having octahedral coordination or Cu^{2+} ions surrounded by a ligand tetrahedron. Intensive ongoing studies of layered honeycomb cobaltites have demonstrated that anisotropic and bond-dependent exchange coupling can be sufficiently strong and may result in an elusive quantum spin liquid state[10–13]. Strong exchange anisotropy was also predicted for Cu^{2+} ions occupying *A* sites in spinels such as $CuAl_2O_4$, if the ground state is characterized by $J_{\mathrm{eff}} = 1/2$[14,15]. However, whether this situation realizes accurate 3*d* materials is an open question.

Resonant inelastic X-ray scattering (RIXS) was shown to be a powerful technique for studying Kitaev materials based on 4*d* and 5*d* transition metals. It can be used both to estimate physical parameters of a system, such as the crystal-field splitting or the SOC constant, and also anomalous magnetic excitation spectra of Kitaev systems, see, e.g.,[16–20]. In the present work we demonstrate that RIXS turns out to be a sensitive probe in the case of 3*d* transition-metal compounds and can discriminate between conventional $S = 1/2$ and spin-orbit $J_{\mathrm{eff}} = 1/2$ states, which may lead to anisotropic exchange interactions. Applying this technique to $CuAl_2O_4$, we show that the vibronic coupling suppresses the formation of the $J_{\mathrm{eff}} = 1/2$ state in this material.

$CuAl_2O_4$ belongs to the *A*-site spinel system, in which the Cu^{2+} ions site at the center of the tetrahedral *A*-sites and the nonmagnetic Al^{3+} ions are located at the center of octahedral *B*-sites. The 3*d* states of tetrahedral Cu^{2+} are split into t_2 and e states because of the T_d crystal field of the four oxygen ions, as illustrated in Fig. 1. An atomic t_2^5 configuration is therefore realized with a single hole in the upper t_2 manifold, making $CuAl_2O_4$ a possible candidate of the spin-orbit Mott insulator because the on-site Coulomb interaction amplifies the effect of relativistic SOC[14,15,21]. The t_2 degeneracy can be lifted through the following two channels. In the presence of SOC, the triply degenerate t_2 states are split into states of effective total angular momenta $J_{\mathrm{eff}} = 1/2$ and 3/2 through the approximation of effective orbital angular momentum $L_{\mathrm{eff}} = 1$ for t_2 states. Hence the ground state would be a spin-orbital entangled state in the SOC limit. On the other hand, the degeneracy can be lifted due to the Jahn-Teller distortion, which lowers the T_d symmetry of crystal field, resulting in a spin-half ground state with a quenched orbital angular momentum.

Recent theoretical studies based on first-principles calculations conclude that $CuAl_2O_4$ is a spin-orbital-entangled $J_{\mathrm{eff}} = 1/2$ Mott insulator[14,15]. X-ray and neutron diffraction results also show that the crystal structure of $CuAl_2O_4$ at ambient pressure is in cubic phase without evidence of tetragonal distortion[22]. However, the breakdown of local symmetry induced by Jahn-Teller distortion can not be ruled out. Moreover, the diffraction data have shown a finite site-disorder in $CuAl_2O_4$, where about 30% of Cu^{2+} ions occupy the octahedral sites[23,24]. To unravel the ground state of $CuAl_2O_4$, we used Cu *L*-edge RIXS to investigate the electronic structure as RIXS is an element- and site-selective probe. In combining with multiplet calculations, our RIXS results demonstrate the existence

[1]National Synchrotron Radiation Research Center, Hsinchu 30076, Taiwan. [2]Graduate Program in Science and Technology of Synchrotron Light Source, National Tsing Hua University, Hsinchu 30013, Taiwan. [3]Department of Electrophysics, National Yang Ming Chiao Tung University, Hsinchu 30010, Taiwan. [4]International Center for Materials Nanoarchitectonics (WPI MANA), National Institute for Materials Science (NIMS), Namiki 1 1, Tsukuba, Ibaraki 305 0044, Japan. [5]Institute of Metal Physics, S. Kovalevskoy Street 18, 620990 Ekaterinburg, Russia. [6]Department of Applied Physics, Waseda University, Shinjuku ku, Tokyo 169 8555, Japan. [7]Department of theoretical physics and applied mathematics, Ural Federal University, Mira St. 19, 620002 Ekaterinburg, Russia. [8]Department of Physics, National Tsing Hua University, Hsinchu 30013, Taiwan.
✉email: streltsov@imp.uran.ru; djhuang@nsrrc.org.tw

Published in partnership with Nanjing University

npj nature partner journals

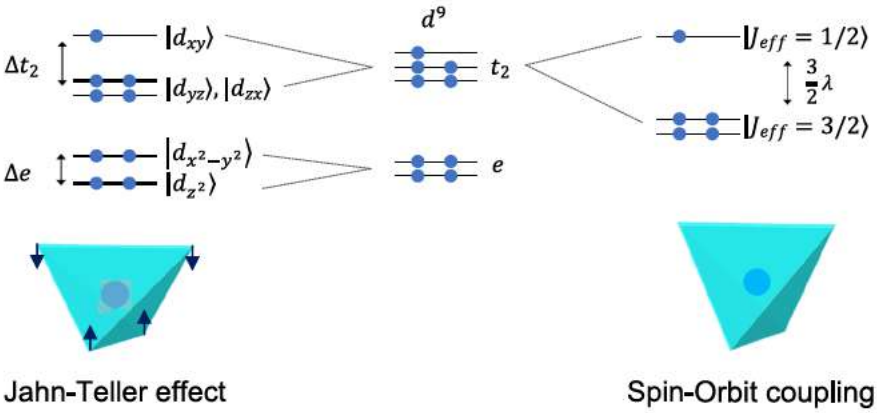

Fig. 1 Schematic illustration on the t_2 splitting of tetrahedral Cu^{2+} due to the Jahn-Teller effect (left) and spin-orbit coupling (right).

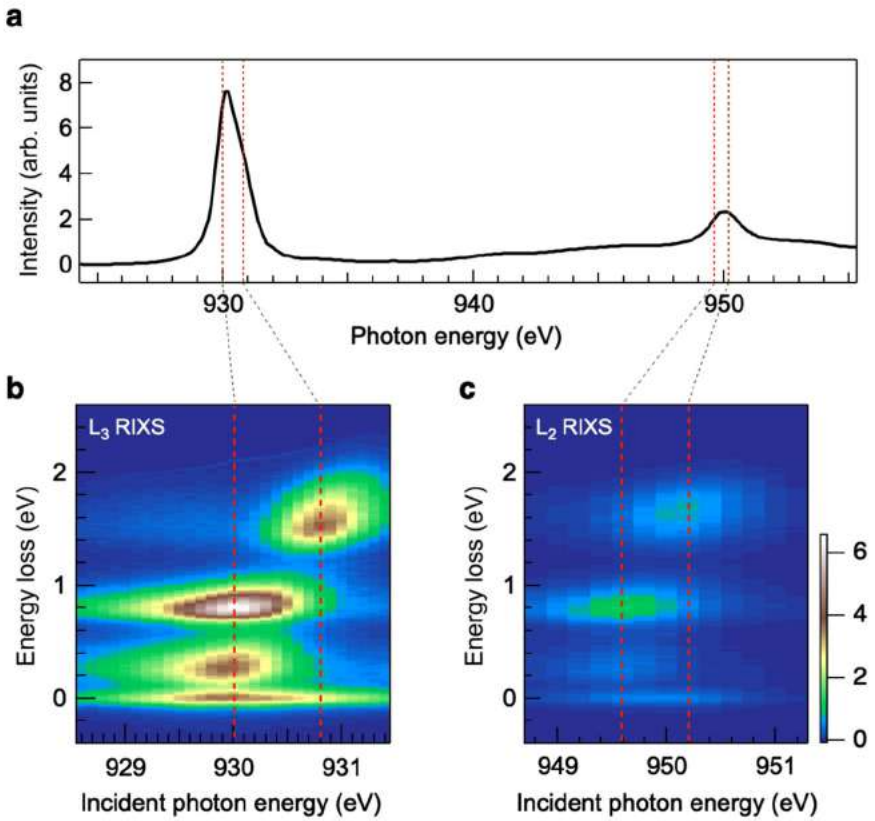

Fig. 2 RIXS intensity distribution maps of $CuAl_2O_4$ in the plane of energy loss vs. incident photon energy. **a** Cu *L*-edge XAS spectrum measured with total electron yield. **b** & **c** RIXS intensity maps measured around Cu L_3 and L_2 edges, respectively. The vertical red dashed lines indicate RIXS features from tetrahedral and octahedral Cu^{2+}, corresponding to the absorption energies of the XAS spectrum shown in (**a**), i.e., 930 & 949.6 eV and 930.8 & 950.2 eV, respectively. All spectra were recorded at room temperature with π-polarized incident X-ray.

of local Jahn-Teller distortion in the tetrahedral sites, in contrast to the scenario of spin-orbital entanglement.

RESULTS

X-ray absorption

L-edge X-ray absorption spectroscopy (XAS) is an effective tool to investigate the SOC in the ground state of transition-metal compounds because it probes the dipole transitions from 2*p* electrons to unoccupied *d* states. If the Cu^{2+} is in the pure $J_{\text{eff}} = 1/2$ ground state, the L_2 edge is forbidden due to the dipole selection rule, i.e., the transition from $2p_{1/2}$ to $J_{\text{eff}} = 1/2$ is not allowed[25,26]. Figures 2(a) plots Cu *L*-edge XAS of $CuAl_2O_4$. Consistent with recent XAS results of single-crystal $CuAl_2O_4$[22], our data show that the L_3-edge XAS contains two distinct features; they arise from the transition to the unoccupied 3*d* states of tetrahedral and octahedral Cu^{2+}. In addition, we observed non-vanishing Cu L_2-edge XAS intensity, implying the existence of octahedral Cu^{2+} or tetrahedral Cu^{2+} which has a ground state with a Jahn-Teller distortion. Although previous XAS study concluded that the L_2 XAS intensity solely originates from the octahedral Cu^{2+} site[22], the measured XAS can also be explained by the scenario of the coexistence of octahedral Cu^{2+} and tetrahedral Cu^{2+} of a spin-half ground state. In other words, whether $CuAl_2O_4$ is a $J_{\text{eff}} = 1/2$ Mott insulator remains an open question. To resolve this issue, we resort to RIXS measurements to

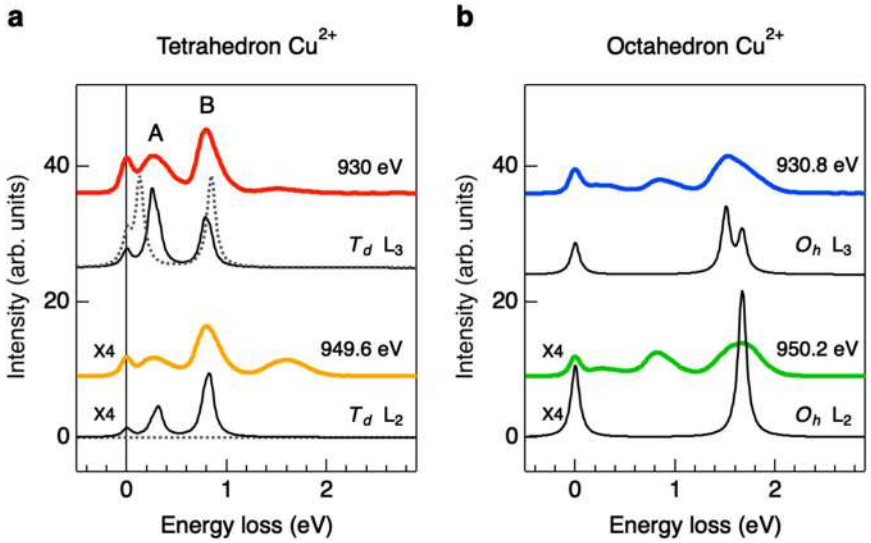

Fig. 3 Cu *L*-edge RIXS spectra recorded at selected incident photon energies in comparison with multiplet calculations. a RIXS spectra measured with the incident photon energies tuned to the resonance of T_d Cu^{2+} compared with calculated RIXS. The solid black lines plot the calculated spectra of T_d Cu^{2+} with the Jahn-Teller distortion; the dashed gray lines are for those in a spin-orbital entangled state. The calculated RIXS intensity of T_d Cu^{2+} in the J_{eff} 1/2 state vanishes. See the main text for the discussion on the origin of peaks A and B. **b** Measured RIXS of O_h Cu^{2+} in comparision with calculations. The solid black lines plot the calculated spectra of O_h Cu^{2+} without a distortion. The incident photon energies E_{in} indicated in (**a**) and (**b**) correspond to the red dashed lines shown in Fig. 2. Both experimental and calculated RIXS spectra of Cu L_2 edge are magnified by a factor of four.

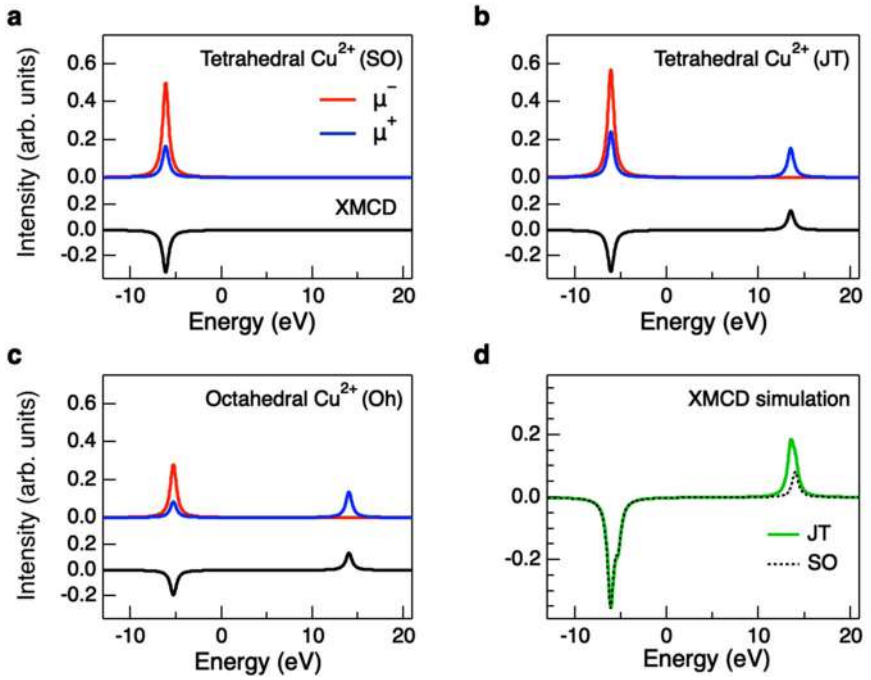

Fig. 4 Simulation of Cu *L*-edge XMCD. a c The calculated XAS and XMCD spectra of Cu^{2+} tetrahedron in the spin-orbit coupling (SO) scheme, Cu^{2+} tetrahedron in the Jahn-Teller (JT) coupling scheme and Cu^{2+} octahedron, respectively. The calculations are down with an external magnetic field 1 T alone the z direction, and the polarization of incident X-ray lies on the xy plane. **d** The thick green line is the calculated XMCD spectra from 37.5% O_h Cu^{2+} and 62.5% T_d Cu^{2+} with Jahn-Teller distortion; the dashed black line is the result of 37.5% O_h Cu^{2+} and 62.5% spin-orbital entangled T_d Cu^{2+}.

separate the contribution of octahedral Cu^{2+} to the L_2 absorption from that of tetrahedral sites by examining the incident-energy dependence of Cu L_2-edge RIXS.

Resonant inelastic X-ray scattering

RIXS has been proved to be a powerful probe of crystal-field excitation from different site symmetry[27]. By selecting the incident photon to particular absorption energy, RIXS measures electronic excitations of *d* electrons with the site-specific orbital degree of freedom. Figure 2(b),(c) show the RIXS intensity maps of $CuAl_2O_4$ measured about Cu L_3 and L_2 edges, respectively. The scattering angle was fixed at 90°. The L_3-edge RIXS map shows two sets of distinct excitation structures which resonate at incident energies of 930 eV and 930.8 eV, respectively, indicating that these

excitations arise from two Cu sites with different crystal field symmetries. Two excitations with energy loss centered at 0.3 eV and 0.82 eV were observed at the first excitation energy, resulting from the *dd* excitations of tetrahedral Cu^{2+}. The excitation at the other incident energy shows only one broad peak at 1.52 eV and is best explained as the *dd* excitations of octahedral Cu^{2+}. Interestingly, similar features occur at Cu L_2-edge RIXS map as well. The Cu L_2-edge RIXS intensity map displays two sets of excitations at incident energies of 949.6 eV and 950.2 eV, respectively. These experimental observations indicate that the Cu L_2-edge XAS spectrum is composed of the $2p$ to $3d$ transition of two Cu sites with different crystal field symmetries, like those in the Cu L_3-edge XAS spectrum.

To understand the electronic structure of $CuAl_2O_4$, we analyzed RIXS data through crystal-field multiplet calculations. The RIXS spectra measured at the L_3 resonance energy of T_d Cu^{2+}, i.e., 930 eV, were compared with the atomic multiplet calculations of a single Cu^{2+} ion in the crystal field produced by four ligands O^{2-}, as shown in Fig. 3(a). With the Hartree–Fock value of $3d$ SOC and a 30% reduction in Slater integrals, the calculations explain measured RIXS features well. The RIXS *dd* excitations of tetrahedral Cu^{2+} are mainly composed of the hole transitions within the t_2 states and those from the t_2 to the e states. The corresponding RIXS peaks are labeled A and B, respectively. The value of $10Dq$ determines the energy position of peak B, while the value of the Jahn-Teller splitting Δe controls the spectral line shape of B, as shown in Supplementary Fig. 3(a),(b). Similarly, Supplementary Fig. 3(c) shows that the Jahn-Teller splitting Δt_2 dictates the energy position of peak A. Through the comparison of the RIXS data with calculations, we found that the crystal field parameters are: $10Dq = 0.72 \pm 0.05$ eV, $\Delta e = 50 \pm 20$ meV, and $\Delta t_2 = 270 \pm 50$ meV. The CuO_4 tetrahedron was found to be slightly compressed along the z axis, lifting the orbital degeneracy of d_{xy}, d_{yz}, d_{zx} states. The Cu L_3-edge RIXS spectra provide explicit spectroscopy evidence for the local distortion in $CuAl_2O_4$. Furthermore, the calculated RIXS intensity at the L_2 edge nearly vanishes when no local distortion was included (dashed gray curves), in contrast to the calculations with CuO_4 structural distortions (black curves). On the other hand, the RIXS spectra measured at the resonance of O_h Cu L-edge show only a single structure, indicating a small distortion in the Cu^{2+} octahedron. The calculated RIXS spectra of O_h Cu sites with $10Dq = 1.6$ eV reproduce the experimental data measured at 930.8 eV and 950.2 eV (Fig. 3(b)).

Our results indicate that in $CuAl_2O_4$, an expected spin-orbit Mott insulator, the T_d Cu site is locally compressed. Through comparing the measured RIXS intensities with calculations of compressed CuO_4 tetrahedron and CuO_6 octahedron, we obtained an amount of site disorder 37.5%, in line with the value obtained from diffraction results. These results indicate that the spin-orbital entangled ground state is destabilized against the Jahn-Teller distorted ground state. From a general perspective, when we start from $S = 1/2$ and increase the SOC strength, the $J_{eff} = 1/2$ state admixes only perturbatively. And then at some critical SOC, we have a drastic transition to $J_{eff} = 1/2$, see Fig. 6 in Ref. [28]. Thus, at small SOC as in Cu, one would expect a small admixture of $J_{eff} = 1/2$, to the ground state. In fact, the distorted ground state from our simulations based on RIXS data has 92% overlap with the d_{xy} orbital expected for the JT ground state. In addition, one can measure spectra of X-ray magnetic circular dichroism (XMCD) in Cu L-edge absorption to further examine the Jahn-Teller distorted ground state of $CuAl_2O_4$ by applying a high magnetic field. Figure 4 plots XMCD spectra simulated by using the electronic parameters from RIXS. Clearly, the XMCD spectral line shape at the L_2-edge of the $J_{eff} = 1/2$ is significantly different from that of the Jahn-Teller state, as shown in Fig. 4(d). Also, the orbital moment the Jahn-Teller state is expected to be quenched; a future XMCD experimental study will be helpful for further clarification.

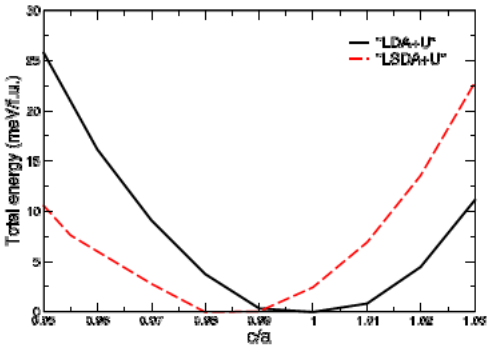

Fig. 5 Total energies as obtained in DFT + *U* + SOC with two different implementations of the + *U* term (black curve - spin-polarization is allowed only in "*U*" part, so-called LDA + U; red - spin polarization is possible in both DFT and "*U*" parts, LSDA + *U*). Minimum at c/a 1 corresponds to SOC J_{eff} 1/2 state, while at c/a < 1 to Jahn-Teller S 1/2. These results illustrate that the type of ground state strongly depends on the details of the DFT calculations.

The conclusion drawn from the RIXS data does not disagree with density functional theory (DFT) results of Ref. [15]. It is shown in Ref. [15] that $J_{eff} = 1/2$ state can be realized in a narrow range of parameters used in the calculations. For example, the ground state changes if we change Hubbard U. Moreover, our calculations show that the choice of double counting also changes the ground state wavefunction. Figure 5 demonstrates that even the choice of DFT +U+SOC calculation scheme may affect the result. Only a delicate balance between Coulomb interaction and SOC stabilizes the $J_{eff} = 1/2$ state, and our *experimental* result shows that most probably this idealized situation is not realized in $CuAl_2O_4$.

DISCUSSION

The spin-orbit materials have become an important class of systems demonstrating exceptional physical properties defined by competition of various interactions such as strong electronic correlations, vibronic and SOCs, etc. Experimental diagnosis of their ground state is a challenging task, which, however, unravels mechanisms lying behind the physical effects observed in these materials. Using RIXS and crystal-field multiplet calculations, we demonstrate that this method is an effective probe of the spin-orbital entangled $J_{eff} = 1/2$ state in $3d$ transition-metal oxides. Being applied to spin-orbit candidate material $CuAl_2O_4$ it shows that, contrary to previous expectations, a competing Jahn-Teller configuration is stabilized in this material, and the tetragonal splittings of the e and t_2 orbitals are $\Delta e = 50$ meV and $\Delta t_2 = 270$ meV, respectively. These results suggest that the T_d Cu site is locally compressed. Neither neutron powder diffraction[23] nor single-crystal X-ray diffraction[29] studies observed anomalous atomic displacement in $CuAl_2O_4$, but total scattering measurements like pair-distribution-function analysis will be an excellent probe to study the local structure.

METHODS

Sample synthesis

A stoichiometric mixture of Al_2O_3 (99.9%) and CuO (99.9%) was used for the synthesis of $CuAl_2O_4$. The mixture was pressed into a pellet and then annealed at 1193 K for 84 h and 1293 K for 38 h (with several intermediate grindings) in the air on a Pt foil. X ray powder diffraction data were measured at room temperature on a RIGAKU MiniFlex600 diffractometer using Cu Kα radiation (2θ range of 8 140°, a step width of 0.02°, and a scan speed of 1 deg/min). The X ray data were analyzed by the Rietveld method using RIETAN 2000[30]. The sample was single phase with sharp reflections. The distribution of Cu^{2+} cations between the tetrahedral $8a$ site and

octahedral 16*d* site was refined with a constraint on the total chemical composition. The experimental, calculated, and difference X ray diffraction profiles and the main refinement results are shown in Supplementary Fig. 1.

XAS and RIXS measurements

All XAS and RIXS measurements were performed at the AGM AGS spectrometer of beamline 41A at Taiwan Photon Source[31]. This AGM AGS beamline is based on the energy compensation principle of grating dispersion. The energy bandwidth of incident X ray was 314.5 meV while keeping the total energy resolution of RIXS at 90 meV. The sample was at room temperature during the measurements. Both XAS and RIXS measurements were carried out using a linear horizontally (π) polarized X ray. The XAS spectrum was measured with a normal incident X ray in the total electron yield mode. For the RIXS measurement, the incidence angle was 45°, and the scattering angle was fixed at 90°.

Multiplet calculations

Simulations of RIXS, XAS, and XMCD spectra were performed with the full multiplet code through QUANTY, a script language to calculate many body eigenenergy, XAS, and RIXS spectra[32,33]. The on site Coulomb interaction, the crystal field, and the 2*p* and 3*d* SOC (ζ_{2p} & ζ_{3d}) were included in the calculations. The intra atomic Coulomb interaction of 3*d* electrons is described by the radial part of the direct Coulomb interactions $F^2(3d, 3d)$ and $F^4(3d, 3d)$. The interaction between core hole and 3*d* electrons is described by $F^2(2p, 3d)$ and exchange interactions $G^1(2p, 3d)$, $G^3(2p, 3d)$. The Hartree Fock values of ζ_{2p} (13.498 eV) and ζ_{3d} (0.102 eV), and a scaling factor 70% for Slater integrals were used in the calculations. The calculations of tetrahedral and octahedral Cu^{2+} were conducted separately with crystal field of 0.72 eV and 1.55 eV, respectively. The calculation of RIXS and XAS spectra are an average of three possible geometries as described in Supplementary Fig. 2.

DFT calculations

DFT calculations were performed using VASP package[34] and PBE type of the exchange correlation functional[35]. We used 125 k points for the Brillouin zone integration and chose *U* correction according to ref. [36] with Hubbard *U* 7 eV[37,38] and Hund's exchange J_H 1 eV.

DATA AVAILABILITY

All data generated or analyzed during this study are available from the corresponding authors upon reasonable request.

Received: 6 September 2021; Accepted: 22 January 2022;
Published online: 21 March 2022

REFERENCES

1. Jackeli, G. & Khaliullin, G. Mott insulators in the strong spin orbit coupling limit: from Heisenberg to a quantum compass and Kitaev models. *Phys. Rev. Lett.* **102**, 017205 (2009).
2. Pesin, D. & Balents, L. Mott physics and band topology in materials with strong spin orbit interaction. *Nat. Phys.* **6**, 376 381 (2010).
3. Armitage, N. P., Mele, E. J. & Vishwanath, A. Weyl and Dirac semimetals in three dimensional solids. *Rev. Mod. Phys.* **90**, 15001 (2018).
4. Takagi, H., Takayama, T., Jackeli, G., Khaliullin, G. & Nagler, S. E. Concept and realization of Kitaev quantum spin liquids. *Nat. Rev. Phys.* **1**, 264 280 (2019).
5. Khomskii, D. I. & Streltsov, S. V. Orbital effects in solids: basics, recent progress, and opportunities. *Chem. Rev.* **121**, 2992 (2021).
6. Rau, J. G., Lee, E. K. H. & Kee, H. Y. Spin orbit physics giving rise to novel phases in correlated systems: Iridates and related materials. *Annu. Rev. Condens. Matter Phys.* **7**, 195 221 (2016).
7. Winter, S. M. et al. Models and materials for generalized Kitaev magnetism. *J. Phys. Condens. Matter* **29**, 493002 (2017).
8. Liu, H. & Khaliullin, G. Pseudospin exchange interactions in d^7 cobalt compounds: Possible realization of the Kitaev model. *Phys. Rev. B* **97**, 014407 (2018).
9. Liu, H., Chaloupka, J. c. v. & Khaliullin, G. Kitaev spin liquid in 3*d* transition metal compounds. *Phys. Rev. Lett.* **125**, 047201 (2020).
10. Zhong, R., Gao, T., Ong, N. P. & Cava, R. J. Weak field induced nonmagnetic state in a Co based honeycomb. *Sci. Adv.* **6**, eaay6953 (2020).
11. Kim, C. et al. Antiferromagnetic Kitaev interaction in $J_{\text{eff}} = 1/2$ cobalt honeycomb materials $Na_3Co_2SbO_6$ and $Na_2Co_2TeO_6$ (2021).
12. Chen, W. et al. Spin orbit phase behavior of $Na_2Co_2TeO_6$ at low temperatures. *Phys. Rev. B* **103**, L180404 (2021).
13. Gillig, M. et al. Unusual heat transport of the Kitaev material $Na_2Co_2TeO_6$: putative quantum spin liquid and low energy spin excitations. J. Phys.: Condens. Matter **34**, 045802 https://arxiv.org/abs/2101.12199 (2022).
14. Nikolaev, S. A., Solovyev, I. V., Ignatenko, A. N., Irkhin, V. Y. & Streltsov, S. V. Realization of the anisotropic compass model on the diamond lattice of Cu^{2+} in $CuAl_2O_4$. *Phys. Rev. B* **98**, 201106 (2018).
15. Kim, C. H. et al. Theoretical evidence of spin orbital entangled $J_{\text{eff}} = 1/2$ state in the 3*d* transition metal oxide $CuAl_2O_4$. *Phys. Rev. B* **100**, 161104 (2019).
16. Halász, G. B., Perkins, N. B. & van den Brink, J. Resonant inelastic X ray scattering response of the Kitaev honeycomb model. *Phys. Rev. Lett.* **117**, 127203 (2016).
17. Halász, G. B., Kourtis, S., Knolle, J. & Perkins, N. B. Observing spin fractionalization in the Kitaev spin liquid via temperature evolution of indirect resonant inelastic X ray scattering. *Phys. Rev. B* **99**, 184417 (2019).
18. Revelli, A. et al. Fingerprints of Kitaev physics in the magnetic excitations of honeycomb iridates. *Phys. Rev. Res.* **2**, 043094 (2020).
19. Lebert, B. W. et al. Resonant inelastic X ray scattering study of *α* $RuCl_3$: a pro gress report. *J. Condens. Matter Phys.* **32**, 144001 (2020).
20. Suzuki, H. et al. Proximate ferromagnetic state in the Kitaev model material *α* $RuCl_3$. *Nat. Commun.* **12**, 4512 (2021).
21. Liu, G. Q., Antonov, V. N., Jepsen, O. & Andersen., O. K. Coulomb enhanced spin orbit splitting: The missing piece in the Sr_2RhO_4 puzzle. *Phys. Rev. Lett.* **101**, 026408 (2008).
22. Cho, H. et al. Pressure induced transition from $J_{\text{eff}} = 1/2$ to $s = 1/2$ states in $CuAl_2O_4$. *Phys. Rev. B* **103**, L081101 (2021).
23. Nirmala, R. et al. Spin glass behavior in frustrated quantum spin system $CuAl_2O_4$ with a possible orbital liquid state. *J. Condens. Matter Phys.* **29**, 13LT01 (2017).
24. Cho, H. et al. Dynamic spin fluctuations in the frustrated *a* site spinel $CuAl_2O_4$. *Phys. Rev. B* **102**, 014439 (2020).
25. Thole, B. T. & van der Laan, G. Linear relation between X ray absorption branching ratio and valence band spin orbit expectation value. *Phys. Rev. A* **38**, 1943 1947 (1988).
26. Clancy, J. P. et al. Spin orbit coupling in iridium based 5*d* compounds probed by X ray absorption spectroscopy. *Phys. Rev. B* **86**, 195131 (2012).
27. Huang, H. Y. et al. Jahn Teller distortion driven magnetic polarons in magnetite. *Nat. Commun.* **8**, 15929 (2017).
28. Streltsov, S. V. & Khomskii, D. I. Jahn Teller effect and spin orbit coupling: friends or foes? *Phys. Rev. X* **10**, 031043 (2020).
29. Fregola, R. A., Bosi, F., Skogby, H. & Hålenius, U. Cation ordering over short range and long range scales in the $MgAl_2O_4$ $CuAl_2O_4$ series. *Am. Mineral.* **97**, 1821 1827 (2012).
30. Izumi, F. & Ikeda, T. A rietveld analysis programm RIETAN 98 and its applications to zeolites. *Mater. Sci. Forum* **321–324**, 198 205 (2000).
31. Singh, A. et al. Development of the soft X ray AGM AGS RIXS beamline at the Taiwan photon source. *J. Synchrotron Radiat.* **28**, 977 986 (2021).
32. Haverkort, M. W., Zwierzycki, M. & Andersen, O. K. Multiplet ligand field theory using Wannier orbitals. *Phys. Rev. B* **85**, 165113 (2012).
33. Haverkort, M. W. Quanty for core level spectroscopy excitons, resonances and band excitations in time and frequency domain. *J. Phys. Conf. Ser.* **712**, 012001 (2016).
34. Kresse, G. & Furthmüller, J. Efficient iterative schemes for ab initio total energy calculations using a plane wave basis set. *Phys. Rev. B* **54**, 11169 11186 (1996).
35. Perdew, J. P., Burke, K. & Ernzerhof, M. Generalized gradient approximation made simple. *Phys. Rev. Lett.* **77**, 3865 3868 (1996).
36. Liechtenstein, A. I., Anisimov, V. I. & Zaanen, J. Density functional theory and strong interactions: Orbital ordering in Mott Hubbard insulators. *Phys. Rev. B* **52**, R5467 R5470 (1995).
37. Markina, M. M. et al. Magnetic phase diagram and first principles study of $Pb_3TeCo_3V_2O_{14}$. *Phys. Rev. B* **89**, 104409 (2014).
38. Zvereva, E. A. et al. Orbitally induced hierarchy of exchange interactions in zigzag antiferromagnetic state of honeycomb silver delafossite $Ag_3Co_2SbO_6$. *Dalton Trans.* **45**, 7373 7384 (2016).

ACKNOWLEDGEMENTS

This work was supported in part by the Ministry of Science and Technology of Taiwan under Grant No. 109 2112 M 213 010 MY3 and 109 2923 M 213 001. S.V.S. and A.F. acknowledge the support of DFT calculations and theoretical analysis by the Russian Science Foundation via project 20 62 46047. E.K. thanks program AAAA A18 118020190095 4 (Quantum) of the Russian ministry of science and education. This work was also supported by KAKENHI Grant No. 19K03741 from JSPS, and Program

for Promoting Researches on the Supercomputer Fugaku (Basic Science for Emergence and Functionality in Quantum Matter) from MEXT.

AUTHOR CONTRIBUTIONS

D.J.H. and S.V.S. conceived and coordinated the project. H.Y.H., A.S., C.I.W., C.D.X. J.O., D.J.H., and C.T.C. developed the RIXS instruments and conducted the RIXS experiments. A.A.B. and E.K. synthesized and characterized the sample. H.Y.H. and D.J.H. performed multiplet, and S.V.S. performed DFT calculations. H.Y.H., D.J.H., S.V.S., and A.F. analyzed the data and wrote the paper with inputs from other authors.

COMPETING INTERESTS

The authors declare no competing interests.

ADDITIONAL INFORMATION

Supplementary information The online version contains supplementary material available at https://doi.org/10.1038/s41535 022 00430 0.

Correspondence and requests for materials should be addressed to S. V. Streltsov or D. J. Huang.

Acoustic plasmons and conducting carriers in hole-doped cuprate superconductors

A. Singh,[1] H. Y. Huang,[1] Christopher Lane,[2,3] J. H. Li,[4] J. Okamoto,[1] S. Komiya,[5] Robert S. Markiewicz,[6] Arun Bansil,[6] T. K. Lee,[4] A. Fujimori,[7,1,4] C. T. Chen,[1] and D. J. Huang[1,4,*]

[1]*National Synchrotron Radiation Research Center, Hsinchu 30076, Taiwan*
[2]*Theoretical Division, Los Alamos National Laboratory, Los Alamos, New Mexico 87545, USA*
[3]*Center for Integrated Nanotechnologies, Los Alamos National Laboratory, Los Alamos, New Mexico 87545, USA*
[4]*Department of Physics, National Tsing Hua University, Hsinchu 30013, Taiwan*
[5]*Central Research Institute of Electric Power Industry, Yokosuka, Kanagawa, 240-0196, Japan*
[6]*Physics Department, Northeastern University, Boston, Massachusetts 02115, USA*
[7]*Department of Applied Physics, Waseda University, Shinjuku-ku, Tokyo 169-8555, Japan*

(Received 26 October 2021; revised 27 January 2022; accepted 6 May 2022; published 9 June 2022)

The layered crystal structures of cuprates enable collective charge excitations fundamentally different from those of three-dimensional metals. Acoustic plasmons have been observed in electron-doped cuprates by resonant inelastic x-ray scattering (RIXS); in contrast, the characteristics of acoustic plasmons in hole-doped cuprates are under debate, despite extensive measurements. This contrast led us to investigate the charge excitations of hole-doped cuprate $La_{2-x}Sr_xCuO_4$. Here we present incident-energy-dependent RIXS measurements and calculations of collective charge response via the loss function to reconcile the issues above. Our results provide evidence for the acoustic plasmons of Zhang-Rice singlet (ZRS), which has a character of the Cu $3d_{x^2-y^2}$ strongly hybridized with the O $2p$ orbitals; the metallic behavior is implied to result from the movement of ZRS rather than the simple hopping of O $2p$ holes.

DOI: 10.1103/PhysRevB.105.235105

I. INTRODUCTION

The superconductivity of cuprates, which has been a mystery ever since its discovery decades ago, is created through doping electrons or holes into a Mott insulator [1,2]. There exists an inherent electron-hole asymmetry in cuprates [3,4]. The antiferromagnetic phase of electron-doped cuprates persists at higher doping concentrations, and its superconductivity is more difficult to achieve. Electron correlations in electron-doped cuprates appear weaker than those of hole-doped compounds. Measurements of resonant inelastic x-ray scattering (RIXS) reveal acoustic plasmons in electron-doped cuprates [5,6], showing the characteristic of conduction electrons of a layered system as shown in Fig. 1(a) in the presence of a long-range Coulomb interaction [7,8]. Acoustic plasmons of hole-doped cuprates, however, were not observed in measurements of Cu L-edge RIXS [9–14]. Although optical plasmons with a quadratic dispersion appear in measurements of electron energy loss spectroscopy (EELS), acoustic plasmons of cuprates were not detected in EELS measurements [15–19]. Acoustic plasmons of cuprates were also not observed in other studies such as optical spectroscopy, including reflectance and ellipsometry measurements [20–24], which is limited to nearly zero momentum transfer. Interestingly, recent O K-edge RIXS results showed the presence of acoustic plasmons in hole-doped cuprates [25].

The conducting carriers are hallmarks of hole-doped cuprates, but their nature remains elusive. Upon doping, the low-energy excitations in the optical conductivity of $La_{2-x}Sr_xCuO_4$ (LSCO) are much enhanced [21]; the Hall coefficient R_H of LSCO is much smaller than what is expected from the contribution of doped holes [26], i.e., $R_H \ll \frac{1}{n_p e}$, where n_p is the hole density and e is the magnitude of electron charge. Early photoemission studies on superconducting cuprates indicated that the parent compound is a charge-transfer insulator, which led to a conjecture that doped holes are oxygen p-like [27]. Theoretically, doped holes are assumed to enter p orbitals of an O atom between two Cu atoms, i.e., the Emery model [28], or of four oxygen atoms surrounding one Cu atom to form a spin singlet termed a Zhang-Rice singlet (ZRS) [29], as illustrated in Fig. 1(b). O K-edge x-ray absorption [30] and resonant elastic scattering [31] indeed provided experimental evidence for O $2p$ holes. The RIXS results also concluded that the acoustic plasmons are predominantly associated with the O sites through a strong $2p$ character [25]. In contrast, photoemission intensity at the Fermi level showed no resonant enhancement at the O K edge [32]. Many angle-resolved photoemission data [33] have been interpreted based on band structures in the local density approximation, which predict that Cu d and oxygen p characters are about equally mixed at the Fermi level. In addition, theoretical calculations using the three-band Hubbard model [34] reveal that the ZRS band of hole-doped cuprates is composed of a comparable amount of O $2p$ and Cu $3d_{x^2-y^2}$.

Here we report measurements of incident-energy-dependent O K-edge RIXS to investigate the nature of the conducting carriers of superconducting LSCO with the doping concentration $x = 0.12$. The remainder of this paper is organized as follows. In Sec. II, we present the experimental technique RIXS and the calculation details. The RIXS results and their comparison with the calculated loss

*Corresponding author: djhuang@nsrrc.org.tw

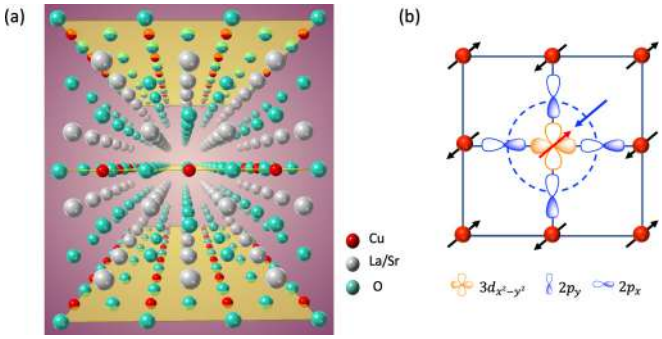

FIG. 1. (a) Crystal structure of LSCO. The stacked CuO_2 layers are highlighted in yellow. (b) Cartoon illustration of a ZRS in the CuO_2 plane. It is a two-hole state formed by a Cu $d_{x^2-y^2}$ hole hybridized with an O $2p_{x,y}$ hole distributed over the surrounding ligands in an antiparallel spin configuration. The singlet moves through the lattice of Cu^{2+} ions in a way similar to that of a mobile hole in the CuO_2 plane. The arrows on Cu^{2+} indicate the antiferromagnetic structure of the lattice.

function are discussed in Sec. III, followed by a conclusion section.

II. METHODS

A. RIXS measurements

The LSCO single crystal was grown by the traveling-solvent floating zone method [35,36]. After growth, the crystals were annealed appropriately to remove oxygen defects. The oxygen content was tuned to be 4.000±0.001 following Ref. [37]. The stoichiometry $x = 0.12$ was determined from an inductively coupled-plasma atomic-emission spectrometric analysis. The sample's transition temperature T_C of superconductivity was 30 K. See Ref. [35] for the crystal growth and characterization. Based on the above information and the previously published characterizations of LSCO [37,38], our crystal was estimated to have lattice constants $a = b = 3.77$ Å and $c = 13.22$ Å.

We conducted O K-edge RIXS measurements using the AGM-AGS spectrometer of beam line 41A at Taiwan Photon Source. This RIXS beam line has been constructed based on the energy compensation principle of grating dispersion. The instrumental energy resolution defined as the full width at half-maximum (FWHM) was ∼20 meV for all RIXS measurements with the monochromator exit slit set to 100 μm. See Ref. [39] for more details of the beam line. Figure 2(a) shows the scattering geometry of our RIXS measurements. The crystallographic axes of the LSCO crystal were precisely aligned with x-ray diffraction using a unique holder with tilting adjustment. Prior to RIXS measurements, the LSCO sample was cleaved in air and then mounted on a three-axis in-vacuum manipulator through a load-lock system. X-ray absorption spectra were measured using a photodiode in the fluorescence yield mode. The resonant conditions were achieved by tuning the energy of the incident x ray to the Zhang-Rice singlet (ZRS) about 528.3 eV or the upper Hubbard band (UHB) [30,40]. RIXS measurements were recorded with σ-polarized incident x rays and normalized to the fluorescence intensity for various in-plane wave-vector changes. The sample was cooled to 23 K with liquid helium.

B. Theoretical calculations

In a RIXS process, a photon scatters resonantly to another state, leaving behind an electron-hole excitation of well-defined momentum $\mathbf{q}$ and energy ω. The general expression for the K-edge RIXS intensity [41,42] can be expressed

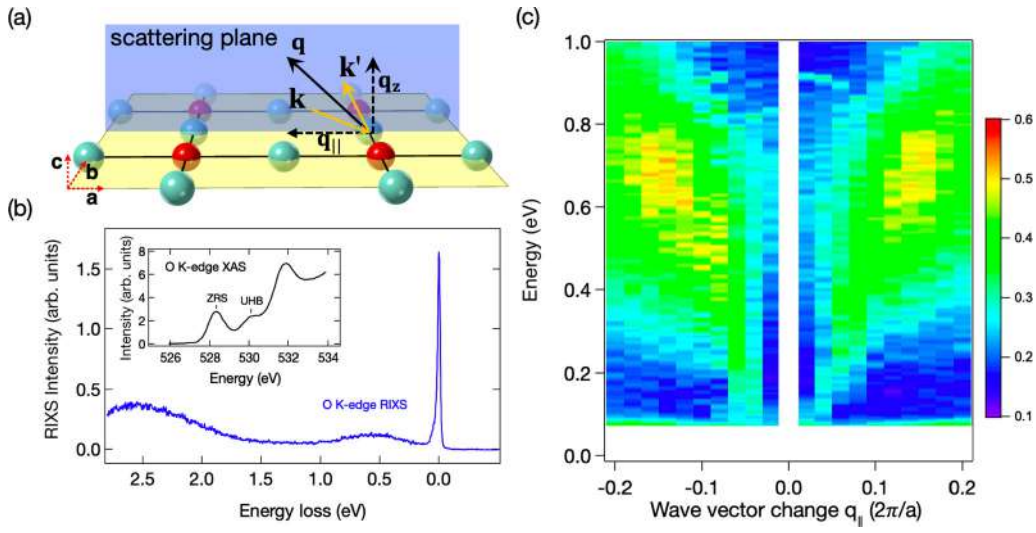

FIG. 2. (a) Scattering geometry of RIXS measurements. The CuO_2 plane is perpendicular to the scattering plane defined by $\mathbf{k}$ and $\mathbf{k}'$, which are the wave vectors of the incident and scattered x rays, respectively. The projection of the wave vector change onto the CuO_2 plane, $\mathbf{q}_\parallel$, is parallel to the antinodal direction. (b) O K-edge RIXS spectrum of LSCO. This spectrum was recorded for a sample at temperature 23 K and with $\mathbf{q}_\parallel = (0.1, 0)$ and $q_z = 0.7$. The total energy resolution of the RIXS monochromator and spectrometer was 20 meV. The incident photon energy was set to the absorption at the ZRS resonance. Inset: XAS spectrum recorded through a fluorescence yield scheme. (c) RIXS intensity distribution map of LSCO in the energy-momentum space. The wave-vector change $\mathbf{q}$ is decomposed into an in-plane wave-vector change $\mathbf{q}_\parallel$ that varies along the antinodal direction and q_z is fixed to 0.7. RIXS spectra were recorded with incident x rays tuned to the ZRS resonance.

TABLE I. Tight-binding hopping parameters (in meV) used in this study.

t	t'	t''	t'''
312.5	−31.25	25.0	68.75

as [43]

$$I_{RIXS}(\mathbf{q},\omega,\omega_i) = (2\pi)^3 N |w(\omega,\omega_i)|^2 \frac{\hat{v}(\mathbf{q})^2}{v(\mathbf{q})} L(\mathbf{q},\omega), \quad (1)$$

where $w(\omega,\omega_i)$ is the energy-dependent matrix element, $\hat{v}(\mathbf{q})$ [$v(\mathbf{q})$] is the interaction energy between electron hole (electron electron), and $L(\mathbf{q},\omega)$ is the loss function in the charge channel

$$\mathrm{Im}\left[-\varepsilon_{00}^{-1}\right], \quad (2)$$

with ε_{00}^{-1} being the inverse dielectric function. Therefore, peaks of K-edge RIXS intensity are directly proportional to transitions in the loss function, which mark the presence of collective charge modes, or plasmons [44]. To construct the inverse dielectric function we follow Ref. [45], where it is defined as

$$\varepsilon_{IJ}^{-1} = [\delta_{NL} - v_{NK} P_{KL}]_{IJ}^{-1}. \quad (3)$$

$I(J) = 0$ index the charge components, while $I(J) \in \{x, y, z\}$ denote the various spin channels. By assuming a noninteracting ground state and taking the vertex to be the identity, ε_{IJ}^{-1} is the random-phase-approximation (RPA) dielectric function and P_{KL} the Lindhard polarizability. Since the electronic dispersion is local-density-approximation-like for $x = 0.12$ [46], we use the single-band electronic dispersion ε_k as defined in Refs. [47,48] with the hopping parameters given in Table I.

To generate acoustic plasmons we must go beyond the usual Hubbard limiting case and consider the full long-range Coulomb interaction. Moreover, the treatment of the long-range Coulomb interaction for the correlated electronic system in a layered structure requires some care. We model $v(r)$ as $\sum_i \bar{v}(\mathbf{R}_i)\delta(r - \mathbf{R}_i)$, so that $v(\mathbf{q}) = \sum_i \bar{v}(\mathbf{R}_i)\exp(-i\mathbf{q}\cdot\mathbf{R}_i)$. $\bar{v}(\mathbf{R}_i)$ is taken to be an on-site Hubbard $U = 2$ eV [49] for $\mathbf{R}_i = 0$ and a screened Coulomb interaction contribution $\bar{v}(\mathbf{R}_i) = e^2/(\varepsilon_0 \mathbf{R}_i)$ for $\mathbf{R}_i \neq 0$, using a background dielectric constant $\varepsilon_0 = 6$. To recover the correct $q \to 0$ limit of $v(\mathbf{q})$ we range separate $v(\mathbf{r})$ into short-range (SR) and long-range (LR) pieces. For the short-range interactions where r less than or equal to a cutoff L we sum the contributions of all in-plane Cu terms. We approximate the remaining long-range component ($r > L$) by a continuum. Then after summing over the interplane contribution we arrive at the following expression for $v(\mathbf{q})$ [43,50],

$$v(\mathbf{q}) = v_{2d}^{SR}(\mathbf{q}) + v_{2d}^{LR}(\mathbf{q}) + v_z(\mathbf{q}), \quad (4)$$

where

$$v_{2d}^{SR}(\mathbf{q}) = U + \sum_{i\neq 0}^{L} \frac{e^2}{\varepsilon_0 R_i} e^{-i\mathbf{q}\cdot\mathbf{R}_i}, \quad (5a)$$

$$v_{2d}^{LR}(\mathbf{q}) = \frac{2\pi e^2}{\varepsilon_0 a^2 q_\parallel}\Big[1 - q_\parallel L J_0(q_\parallel L)\frac{\pi q_\parallel L}{2}(J_0(q_\parallel L)H_1(q_\parallel L) - J_1(q_\parallel L)H_0(q_\parallel L))\Big], \quad (5b)$$

$$v_z(\mathbf{q}) = \frac{2\pi e^2}{\varepsilon_0 a^2 q_\parallel}\left[\frac{\cos(q_z l) - e^{-q_\parallel l}}{\cosh(q_\parallel l) - \cos(q_z l)}\right]. \quad (5c)$$

a and $l = c/2$ are the in-plane lattice parameter and distance between adjacent CuO_2 planes in La_2CuO_4 [51,52], respectively, J_i (H_i) are the Bessel (Struve) functions, and the short-range cutoff L is $500a$. Then by inserting $v(q)$ in Eq. (3) we obtain the loss function.

III. RESULTS AND DISCUSSIONS

A. RIXS results

LSCO has a quasi-two-dimensional (quasi-2D) crystal structure with stacked CuO_2 layers. This system is theoretically expected to exhibit acoustic plasmons [8]. Whereas optical spectroscopy is limited to measurements of nearly zero momentum transfer, RIXS can probe the dispersion of acoustic plasmons in cuprates [5,6,25]. However, the conclusion drawn from O K-edge RIXS results [25] is inconsistent with EELS results [18,19]. Figure 2(b) plots a typical RIXS spectrum of hole-doped cuprate LSCO with the incident photon energy set to the ZRS resonance in XAS denoted in the inset. This spectrum includes the following features: elastic scattering, phonon excitations, plasmons, parabimagnons, d-d excitations, and electron-hole pair excitations. Because of the limited energy resolution of the RIXS spectrometer, the low-energy phonon excitations were not well resolved from the elastic scattering, giving rise to an asymmetric and intense spectral profile near the zero energy loss [53]. Because the O $2p$ bands are strongly hybridized with Cu $3d$, d-d excitations of Cu and the excitonic excitations of ZRS occur in this RIXS spectrum at an energy loss above 1.5 eV; these excitation energies overlap with the energy of resonant fluorescence. Distinct from the Cu L_3-edge RIXS measurements, the O K-edge resonance yields negligible single-magnon excitations but permits us to observe even-order spin excitations. The excitation of parabimagnons, which are called bimagnons throughout the paper for simplicity, appears in the broad feature at an energy loss centered at about 0.5 eV in LSCO [54,56]. This broad feature might also contain plasmon excitations, depending on the wave-vector change, which is composed of in-plane wave-vector change $\mathbf{q}_\parallel$ and out-of-plane component q_z, i.e., $\mathbf{q} = \mathbf{q}_\parallel + q_z\hat{\mathbf{z}}$; they are expressed in units of $\frac{2\pi}{a}$ and $\frac{2\pi}{c}$ throughout the paper, respectively.

We measured $\mathbf{q}$-dependent spectra on LSCO ($x = 0.12$) to examine acoustic plasmons in hole-doped cuprates. Figure 2(c) maps the distribution of RIXS intensity as a function of in-plane wave-vector change $\mathbf{q}_\parallel$ along the antinodal direction with q_z fixed to 0.7. This measurement method differs from those used in most of previous momentum-resolved RIXS measurements on cuprates in which q_z was not fixed [6,14]. In addition to the quasielastic scattering, overall this RIXS intensity map shows a broad feature that shifts toward higher energy with an increasing width as $q_\parallel$ is increased. After scrutinizing the RIXS data with $\mathbf{q}_\parallel$ near the zone center, we found that the RIXS spectrum of $\mathbf{q}_\parallel = (0.04, 0)$ contains a low-energy narrow feature near 0.14 eV and a broad feature of

bimagnon excitation centered at about 0.5 eV, like bimagnons in the undoped compound La_2CuO_4.

B. RIXS data analysis and curve fitting

In the RIXS spectra recorded at the ZRS resonance, the bimagnon energy overlaps closely with the plasmon energy of $q_\parallel$ larger than 0.06. We analyzed the RIXS spectra measured at the ZRS and UHB resonances through a nonlinear least-squares curve fitting. Prior to the fitting, spectra were normalized to the incident photon flux and corrected for self-absorption [53,57]. Each of the plasmon, bimagnon, and phonon components was fitted with an antisymmetrized Lorentzian function $f(\omega)$ expressed as

$$f(\omega) = \frac{\gamma}{2\pi}\left[\frac{1}{(\omega-\omega_0)^2+(\gamma/2)^2} - \frac{1}{(\omega+\omega_0)^2+(\gamma/2)^2}\right], \tag{6}$$

where ω_0 is the transition energy and γ is FWHM [5,25]. A cubic background was used to account for the tail contribution of d-d excitation. In addition, we used a Gaussian function for the component of elastic scattering.

First, we fitted the spectrum of in-plane momentum $q_\parallel = 0.02$ with four components: one Gaussian function for elastic scattering with an instrumental energy resolution of 20 meV and three antisymmetrized Lorentzian functions for bimagnon, plasmon, and phonon of energy between 0.03 and 0.05 eV [53]. We used the previously published results [25,54] to limit the bimagnon energy to be larger than 0.4 eV and found that it was a broad peak centered about 0.5 eV. For the fitting of RIXS spectra of other in-plane momenta, the position and FWHM of the bimagnon component were constrained to be close to those obtained from the fit results of $q_\parallel = 0.02$ within ± 0.025 eV and ± 0.15 eV, respectively. The constraints of the bimagnon energy and width in curve fitting may cause some uncertainty about the plasmon dispersion, although the deduced dispersion is similar to that of electron-doped cuprates. The conclusion from RIXS at the ZRS resonance requires further verification because of the spectral contributions of bimagnons. We varied the incident photon energy in the RIXS measurements to the UHB resonance to diminish the spectral weight of the bimagnon. The bimagnon contribution to the RIXS spectra measured at the UHB resonance is nearly negligible, particularly for high $q_\parallel$. Since the UHB is more localized and at about 2 eV higher than the ZRS band, RIXS excitations directly involved with the ZRS resonance are more sensitive to bimagnons than those with the UHB resonance [54]. The $q_\parallel$-dependent widths of acoustic plasmons obtained from the curve fitting results of RIXS data at the UHB resonance justify those from the data measured at the ZRS resonance. See Figs. S1 and S2 in the Supplemental Material [55] for the comparison of the fitted curves with measured data. Table II lists the fitted parameters of our curve-fitting analysis.

Figure 3(a) plots the spectra of various $q_\parallel$ after subtraction of the bimagnon and background; it reveals that the energy of the acoustic plasmon monotonically increases from 0.08–0.69 eV as $q_\parallel$ is increased to 0.2. The obtained plasmon dispersion of LSCO is similar to that of electron-doped cuprate $La_{2-x}Ce_xCuO_4$ (LCCO) [5]. Our results indicate that the plasmons of hole-doped cuprates are strongly damped and have a greater spectral width than those of electron-doped cuprates because of stronger electron correlations [4,58]. For example, the plasmon FWHM of LSCO at $q_\parallel = 0.1$ and $q_z = 1.0$ is 0.68 eV, whereas that of LCCO is about 0.3 eV. Figure 3(b) plots momentum-dependent RIXS spectra measured with the x-ray energy set to the UHB resonance, in which the excitations are dominated by Cu $3d$ orbitals. As plotted in Figs. 3(a) and 3(b), the plasmon dispersions excited by x rays tuned to the ZRS and UHB resonances agree with each other, revealing that both O $2p$ and Cu $3d$ orbitals are involved with the acoustic plasmons.

TABLE II. Fit results of RIXS spectra recorded at the ZRS and UHB resonances for various in-plan momentum ($q_\parallel$, 0) in units of $2\pi/a$. The energy of plasmon (ω_{plasmon}) and bimagnon (ω_{bimag}) are given in units of eV; their FWHM are expressed by γ_{plasmon} and γ_{bigmag} in units of eV, respectively.

ZRS

$q_\parallel$	ω_{plasmon}	I_{plasmon}	γ_{plasmon}	ω_{bimag}	γ_{bimag}
0.02	0.08 ± 0.01	0.18 ± 0.02	0.23 ± 0.05	0.55 ± 0.1	0.8 ± 0.1
0.04	0.14 ± 0.01	0.34 ± 0.04	0.26 ± 0.05	0.54 ± 0.1	0.7 ± 0.1
0.06	0.24 ± 0.02	0.35 ± 0.04	0.43 ± 0.09	0.55 ± 0.1	0.8 ± 0.1
0.08	0.31 ± 0.02	0.30 ± 0.03	0.56 ± 0.12	0.5 ± 0.1	0.8 ± 0.1
0.10	0.51 ± 0.05	0.67 ± 0.07	0.65 ± 0.13	0.5 ± 0.1	0.9 ± 0.1
0.12	0.57 ± 0.06	1.10 ± 0.12	0.68 ± 0.14	0.5 ± 0.1	0.8 ± 0.1
0.14	0.60 ± 0.06	1.13 ± 0.12	0.70 ± 0.15	0.5 ± 0.1	0.8 ± 0.1
0.16	0.63 ± 0.06	1.15 ± 0.13	0.72 ± 0.15	0.5 ± 0.1	0.9 ± 0.1
0.18	0.68 ± 0.07	1.03 ± 0.11	0.73 ± 0.15	0.5 ± 0.1	0.6 ± 0.1
0.20	0.69 ± 0.07	0.99 ± 0.10	0.76 ± 0.16	0.5 ± 0.1	0.6 ± 0.1

UHB

$q_\parallel$	ω_{plasmon}	I_{plasmon}	γ_{plasmon}	ω_{bimag}	γ_{bimag}
0.02	0.08 ± 0.01	0.07 ± 0.01	0.18 ± 0.04	0.5 ± 0.1	0.6 ± 0.1
0.04	0.15 ± 0.01	0.09 ± 0.01	0.20 ± 0.04	0.5 ± 0.1	0.6 ± 0.1
0.06	0.22 ± 0.02	0.13 ± 0.01	0.35 ± 0.07	0.5 ± 0.1	0.6 ± 0.1
0.08	0.30 ± 0.03	0.24 ± 0.02	0.60 ± 0.12	–	–
0.10	0.44 ± 0.04	0.22 ± 0.02	0.62 ± 0.13	–	–
0.12	0.49 ± 0.05	0.24 ± 0.02	0.63 ± 0.13	–	–
0.14	0.54 ± 0.05	0.22 ± 0.02	0.65 ± 0.13	–	–
0.16	0.60 ± 0.06	0.22 ± 0.02	0.67 ± 0.14	–	–
0.18	0.65 ± 0.06	0.20 ± 0.02	0.69 ± 0.14	–	–
0.20	0.66 ± 0.07	0.18 ± 0.02	0.73 ± 0.15	–	–

C. Comparison with the loss function

To verify that the observed collective charge dynamics follow the energy dispersion associated with acoustic plasmons, we calculated the collective charge response of the system via the loss function. That is, on incorporating a long-range Coulomb interaction into the one-band parametrization of LSCO [43] with a hole doping, we calculated $\varepsilon^{-1}(\mathbf{q},\omega)$, in which ε is the dielectric function, and $\mathbf{q}$ contains both in- and out-of-plane momentum transfer components within the RPA. The three dimensionality was incorporated through interplane Coulomb interactions. The loss function was eventually obtained as $-\text{Im}(\varepsilon^{-1})$.

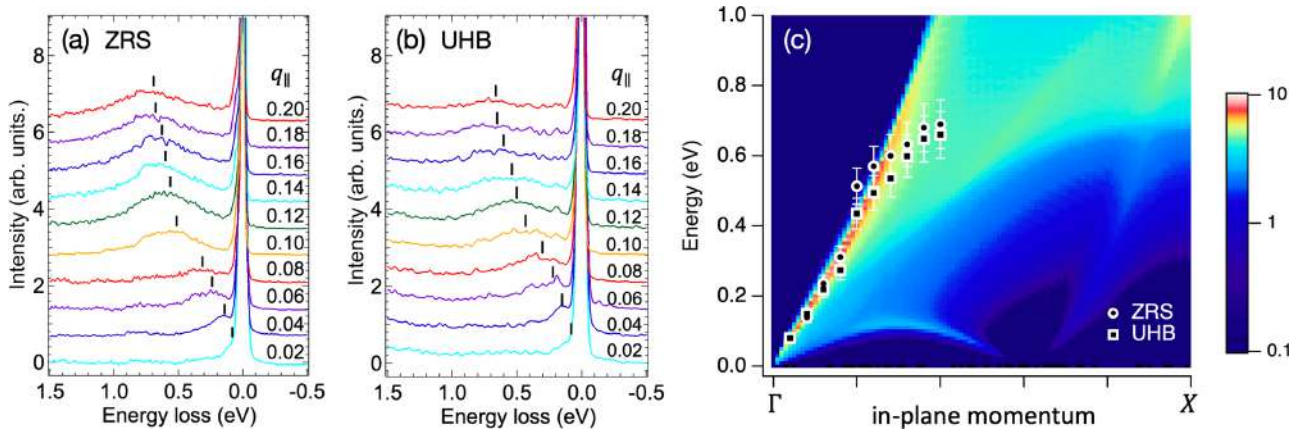

FIG. 3. (a) and (b) Momentum-dependent RIXS spectra of LSCO excited by x rays of energy tuned to the ZRS and the UHB resonances, respectively. The out-of-plane component q_z was fixed to 0.7. Color curves in (a) are spectra deduced from Fig. 2(c) after 10-point binomial smoothing and subtraction of the bimagnon component and the background. RIXS spectra shown in (b), which are multiplied by 3 to account for the difference in the cross section between the ZRS and UHB resonances, are plotted without bimagnon and background subtractions. The details of data analysis are presented in the Supplemental Material [55]. Spectra in both (a) and (b) are offset vertically for clarity; vertical ticks indicate the plasmon energies. (c) Theoretically obtained loss function for LSCO with hole doping $x = 0.12$ along $\Gamma - X$ in the square Brillouin zone with $q_z = 0.7$. Measured plasmon energies of LSCO (circles and squares) deduced from the RIXS spectra shown in (a) and (b) are also plotted for comparison.

Figure 4 shows the loss function for values of q_z ranging from 0–1. For $q_z = 0$, a clear plasmon peak is seen at the zone center near 0.7 eV, in agreement with optical measurements [21]. As $q_\parallel$ changes from Γ to X, the plasmon peak disperses to higher energies, eventually entering the particle-hole continuum around $(\pi/2, 0)$, where the peak intensity sharply decreases. As q_z increases, the plasmon energy at Γ decreases, becoming zero for $q_z > 0.04$. Moreover, the plasmon dispersion along Γ-X softens, becoming linear for $q_z > 0.3$, ultimately merging with the electron-hole continuum for very large q_z, which dampens out the plasmon peak entirely. The evolution of the plasmon with q_z is in agreement with Ref. [7], confirming that the existence of acoustic plasmons arises from the out-of-phase motion of electrons on adjacent CuO_2 planes. These calculations explain the discrepancy between EELS and RIXS results. For transmission-type EELS, the magnitude of electron momentum is typically larger than $2\pi/c$ by a couple of orders [15–17]. A special scattering geometry is required to pick up the contribution of acoustic plasmons. The reflection-type EELS results presented in Ref. [18] and Ref. [19] are dominated by the in-phase motion of electrons on different CuO_2 planes, and they are much less sensitive to acoustic plasmons because the out-of-plane momentum transfers were fixed to $q_z = 20$.

Figure 3(c) plots the calculated loss function for 12% hole-doped LSCO in the paramagnetic phase along the x axis in the Brillouin zone with $q_z = 0.7$. The measured plasmon energies of LSCO are also shown for comparison. The dispersion of an acousticlike plasmon excitation is seen to extend from near zero at the zone center Γ to above 1 eV at X. The slight gap at $q_\parallel = (0, 0)$ is due to the finite interlayer momentum transfer [43,59] in accord with the observed dispersion. The charge fluctuations near the Fermi surface govern the plasmon excitations of small $q_\parallel$. As $q_\parallel$ extends away from the zone center, more incoherent states with decreased lifetime contribute to plasmon excitations, and the width of the plasmon peak increases, consistent with the Landau quasiparticle picture in which the plasmon peak becomes incoherent. As the plasmon enters the particle-hole continuum, the peak broadens, and the slight curve appears to follow the ridge in the particle-hole continuum of the loss function. Consequently, the RIXS spectral width of acoustic plasmons becomes broadened when $q_\parallel$ increases, consistent with the dynamics of the electrons near the Fermi surface. The agreement between our data and theory thus supports the proposal of attributing the zone center mode to acoustic plasmon excitations.

D. 3D nature of acoustic plasmons

Next, we corroborate the acoustic plasmon's three-dimensional (3D) nature originating from the interlayer Coulomb interaction. Figure 5(a) plots the spectra of $\mathbf{q}_\parallel = (0.1, 0)$ with selected q_z. The broad spectral features about 0.5 eV were fitted with two antisymmetrized Lorentzian functions: one is a q_z-independent component for the bimagnon; the other disperses with the change of q_z. We found that when q_z is altered from 0.6 to 1.0, the energy of this feature decreases by 91 meV for $q_\parallel$ fixed to 0.1, i.e., evidence for the 3D nature of plasmon excitations. Figure 5(b) illustrates the dispersions of the plasmon bands of a layered electron-gas model for the high-T_c cuprates [7]. The plasmon bands are restricted to be in between two boundary branches corresponding to the in-phase motion of electrons on separate planes and the out-of-phase motion on adjacent planes, i.e., $q_z = 0$ and $\frac{\pi}{d}$, respectively, where d is the distance between two adjacent CuO_2 layers and $d = c/2$. Figure 4 shows the loss function for values of q_z ranging from 0–1 in units of $2\pi/c$. For $q_z = 0$ [Fig. 4 (top-left panel)] a clear plasmon peak is seen at the zone center near 0.70 eV. As $q_\parallel$ changes from Γ to X the plasmon peak disperses to higher ener-

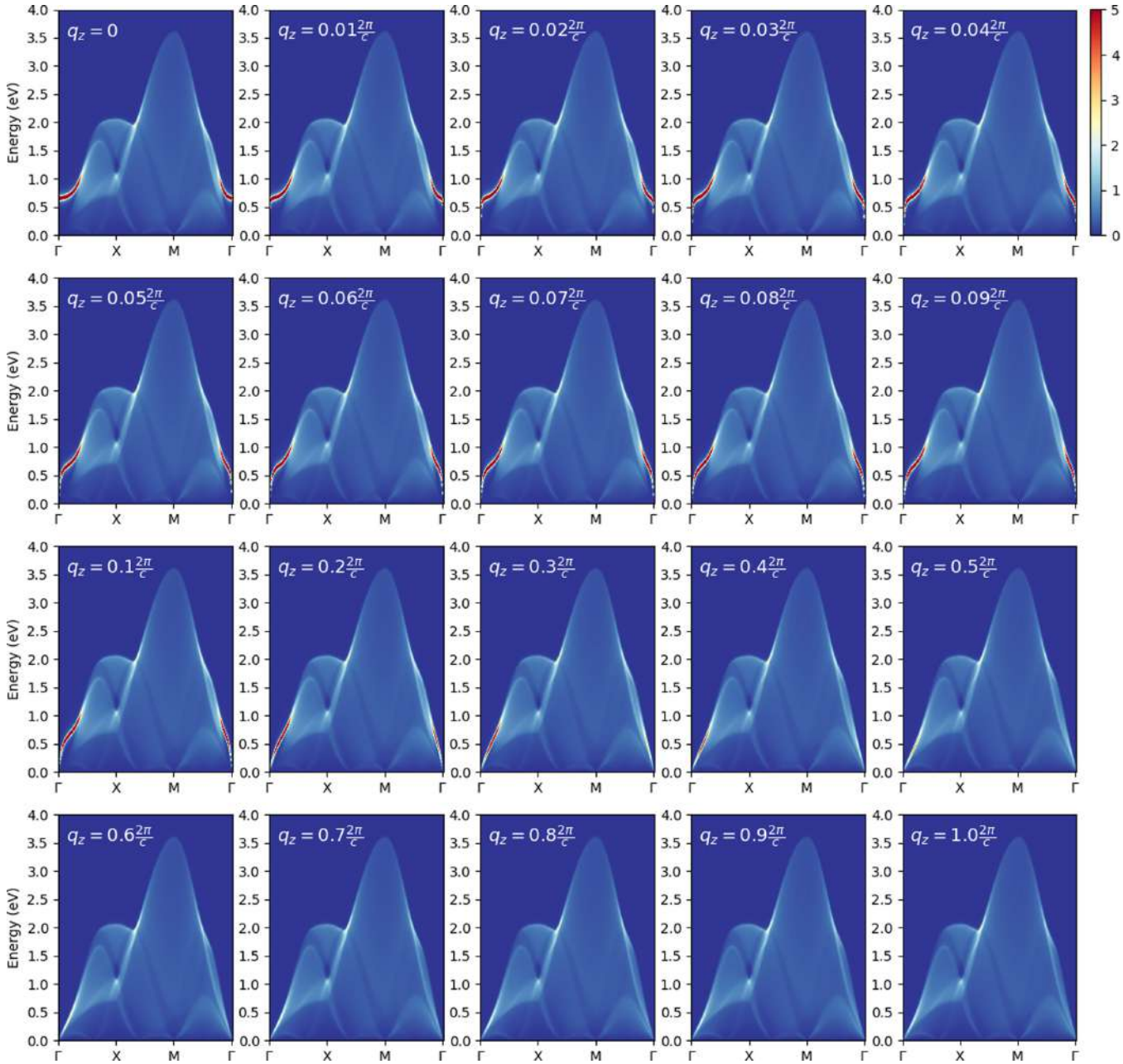

FIG. 4. Calculated loss function along the high-symmetry lines in the square Brillouin zone for various values of q_z.

gies eventually entering the particle-hole continuum around $(\pi/2, 0)$, where the peak intensity sharply decreases. As q_z increases the plasmon energy at Γ decreases, becoming zero for $q_z > 0.04$. Moreover, the plasmon dispersion along Γ-X softens becoming linear for $q_z > 0.3$, ultimately merging with the electron-hole continuum for very large q_z, which dampens out the plasmon peak entirely. The evolution of the plasmon with q_z is in agreement with Ref. [7]. Figure 5(c) compare the measured acoustic-plasmon energy with that from the calculated loss function plotted in Fig. 4 for $q_\parallel = 0.1$. The calculations further verify the decreased plasmon energy as being due to the increase of q_z and reveal the plasmon origin of the observed RIXS excitation.

E. Analysis of spectral weights

In combination with the absence of acoustic plasmon in Cu L-edge RIXS measurements [9–14], the results of O K-edge RIXS tuned to the ZRS resonance seem to suggest that the acoustic plasmons are predominantly of a O $2p$ character [25]. This conclusion, however, is in contrast to the ZRS picture [29], in which O $2p$ and Cu $3d$ are strongly hybridized and the singlet hops through the Cu^{2+} lattice in a way similar to a hole in the single-band effective Hamiltonian. In hole-doped cuprates, the ZRS band crosses the Fermi level at wave vectors near $(\pi, 0)$ and $(\frac{\pi}{2}, \frac{\pi}{2})$, as shown in angle-resolved photoemission measurements [60,61]. One can use a simple cluster model [62] to comprehend the spectral weight of the

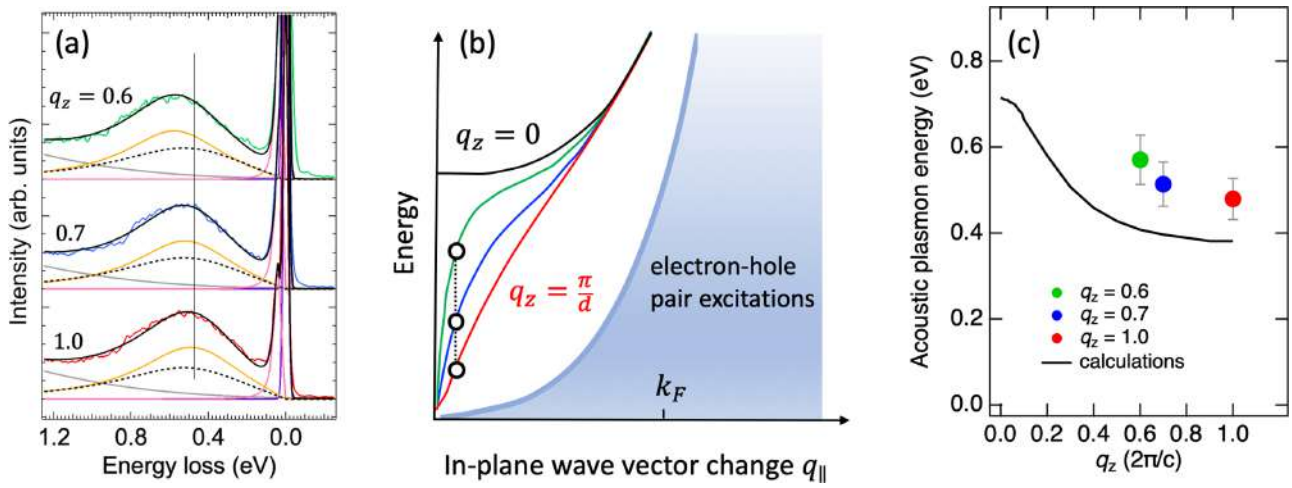

FIG. 5. 3D nature of acoustic plasmons. (a) RIXS spectra of LSCO after data smoothing for selected q_z with $q_\parallel$ fixed to 0.1. The incident x-ray energy was tuned to the ZRS resonance. The fitted spectral function for the plasmon and bimagnon is the antisymmetrized Lorentzian function, as plotted in orange curves and black dashed lines, respectively; the background curves are plotted in gray lines. Bimagnon spectra of all q_z have the same energy position and width. Spectra are vertically offset for clarity. The vertical line indicates the plasmon energy of $q_z = 1.0$. See Supplemental Material [55] for the details of curve fitting. (b) Graphic illustration of the dispersion relations of selected plasmon bands and the electron-hole pair excitations of a layered electron-gas model (after Ref. [7]). The circles indicate the plasmon energy in response to the change in q_z with $q_\parallel$ fixed. (c) Comparison of the measured acoustic plasmon energies with those from the calculated loss function for $q_\parallel = 0.1$. The measured plasmon energies plotted as colored circles correspond to spectra shown in (a), from which the plasmon energies were deduced through curve fitting. The plasmon energy plotted by the black line is from the calculated loss function shown in Fig. 4.

transitions from the ground state to the unoccupied ZRS and UHB probed by O K-edge RIXS; the former has a comparable spectral weight of O $2p$ and Cu $3d$ orbitals, whereas the latter is dominated by Cu $3d$.

In O K-edge RIXS, the O $1s$ electron is excited to the ZRS or UHB. Theoretically, one can use a model Hamiltonian and the Kramers-Heisenberg formula to calculate RIXS cross section [63]. To comprehend the spectral weight of a RIXS process, we approximate the excitation as a transition from the ground state to an excited state. We used a simple cluster model [62] to obtain the spectral weight. In the following approximation, we neglect the effect of core hole in the intermediate state. For a cluster model, the state of a Cu^{2+} ion surrounded by four oxygens is described as

$$|\psi_{Cu^{2+}}\rangle = \alpha\,|d^9\rangle + \beta\,|d^{10}\underline{L}\rangle\,, \tag{7}$$

and the ZRS and UHB states are

$$|\mathrm{ZRS}\rangle = \gamma\,|d^8\rangle + \delta\,|d^9\underline{L}\rangle + \epsilon\,|d^{10}\underline{L}^2\rangle \tag{8}$$

$$|\mathrm{UHB}\rangle = |d^{10}\rangle\,, \tag{9}$$

where $\underline{L}$ represents a ligand hole. The RIXS cross section at the ZRS and UHB resonances are approximately proportional to $|\langle\psi_{Cu^{2+}}|\,\hat{a}_i^\dagger\,|\mathrm{ZRS}\rangle|^2$ and $|\langle\mathrm{UHB}|\,\hat{a}_i^\dagger\,|\psi_{Cu^{2+}}\rangle|^2$ (i = Cu $3d$, O $2p$), respectively, where $\hat{a}_i^\dagger$ is the electron creation operator on orbital i. We extract the spectral weights of O $2p$ and Cu $3d$ at the ZRS resonance as follows:

$$I_{\mathrm{ZRS}}^{O2p} = |\alpha\delta + \beta\epsilon|^2 \tag{10}$$

and

$$I_{\mathrm{ZRS}}^{Cu3d} = |\alpha\gamma + \beta\delta|^2. \tag{11}$$

Similarly, the spectral weights of O $2p$ and Cu $3d$ at the UHB resonance are

$$I_{\mathrm{UHB}}^{O2p} = |\beta|^2 \tag{12}$$

$$I_{\mathrm{UHB}}^{Cu3d} = |\alpha|^2. \tag{13}$$

From the coefficients given by Eskes *et al.* for CuO [62], we have $\alpha = \sqrt{0.67}$, $\beta = \sqrt{0.33}$, $\gamma = \sqrt{0.07}$, $\delta = \sqrt{0.64}$, and $\epsilon = \sqrt{0.28}$. This gives $I_{\mathrm{ZRS}}^{O2p} = 0.86$, $I_{\mathrm{ZRS}}^{Cu3d} = 0.43$, $I_{\mathrm{UHB}}^{O2p} = 0.33$, and $I_{\mathrm{UHB}}^{Cu3d} = 0.67$. Therefore, O $2p$ and Cu $3d$ orbitals have a comparable spectral weight in the RIXS transition at the ZRS resonance, whereas the transition to the UHB is dominated by Cu $3d$. (Note that $I_{\mathrm{ZRS}}^{O2p} + I_{\mathrm{ZRS}}^{Cu3d}$ exceeds 1 is due to the so-called dynamical effect of spectral weight transfer widely seen in correlated systems.) Calculations using the three-orbital Hubbard model [34] for hole-doped cuprates also indicate that the spectral weight of Cu $3d_{x^2-y^2}$ in the ZRS band is comparable to that of O $2p$ and that in the UHB band is dominated by Cu $3d_{x^2-y^2}$. Our observation of plasmons at both ZRS and UHB resonances unravels that the acoustic plasmons are of ZRS character, consistent with the delocalized nature of the ZRS. In other words, not only O $2p$ but also Cu $3d$ states contribute to the itinerant motion of charge carriers in hole-doped cuprates.

IV. CONCLUSIONS

In conclusion, our observation of acoustic plasmons sheds light on the nature of the conducting carriers of hole-doped cuprates. O K-edge RIXS results demonstrate that the p and d orbitals are hybridized in ZRS bands and UHB, consistent with XAS results. The observation of plasmons at both UHB and ZRS resonances corroborates the ZRS picture, revealing that the acoustic plasmons indeed result from the delocalized

nature of the ZRS. Our findings indicate that the conducting carriers are ZRS rather than O $2p$ holes.

ACKNOWLEDGMENTS

We acknowledge NSRRC staff for technical support. We thank Teppei Yoshida for his technical advice on cleaving LSCO crystals. This work was supported in part by the Ministry of Science and Technology of Taiwan under Grants No. 103-2112-M-213-008-MY3 and No. MOST 108-2923-M-213-001. We acknowledge the support of Japan Society for the Promotion of Science under Grant No. 19K03741. The work at Northeastern University was supported by the U.S. Department of Energy (DOE), Office of Science, Basic Energy Sciences Grant No. DE-FG02-07ER46352 and benefited from Northeastern University's Advanced Scientific Computation Center (ASCC), and the NERSC supercomputing center through DOE Grant No. DE-AC02-05CH11231. The work at Los Alamos National Laboratory was supported by the U.S. DOE NNSA under Contract No. 89233218CNA000001 and the Center for Integrated Nanotechnologies, a DOE BES user facility in partnership with the LANL Institutional Computing Program for computational resources. Additional support was provided by DOE Office of Basic Energy Sciences Program (LANL code E3B5).

[1] B. Keimer, S. A. Kivelson, M. R. Norman, S. Uchida, and J. Zaanen, Nature (London) **518**, 179 (2015).
[2] M. Imada, A. Fujimori, and Y. Tokura, Rev. Mod. Phys. **70**, 1039 (1998).
[3] K. Segawa, M. Kofu, S. Lee, I. Tsukada, H. Hiraka, M. Fujita, S. Chang, K. Yamada, and Y. Ando, Nature Phys. **6**, 579 (2010).
[4] C. Weber, K. Haule, and G. Kotliar, Nature Phys. **6**, 574 (2010).
[5] M. Hepting, L. Chaix, E. W. Huang, R. Fumagalli, Y. Y. Peng, B. Moritz, K. Kummer, N. B. Brookes, W. C. Lee, M. Hashimoto, T. Sarkar, J. F. He, C. R. Rotundu, Y. S. Lee, R. L. Greene, L. Braicovich, G. Ghiringhelli, Z. X. Shen, T. P. Devereaux, and W. S. Lee, Nature (London) **563**, 374 (2018).
[6] J. Lin, J. Yuan, K. Jin, Z. Yin, G. Li, K.-J. Zhou, X. Lu, M. Dantz, T. Schmitt, H. Ding, H. Guo, M. P. M. Dean, and X. Liu, npj Quantum Mater. **5**, 4 (2020).
[7] V. Z. Kresin and H. Morawitz, Phys. Rev. B **37**, 7854 (1988).
[8] A. Greco, H. Yamase, and M. Bejas, Commun. Phys. **2**, 3 (2019).
[9] L. Braicovich, J. van den Brink, V. Bisogni, M. M. Sala, L. J. P. Ament, N. B. Brookes, G. M. De Luca, M. Salluzzo, T. Schmitt, V. N. Strocov, and G. Ghiringhelli, Phys. Rev. Lett. **104**, 077002 (2010).
[10] M. Le Tacon, G. Ghiringhelli, J. Chaloupka, M. M. Sala, V. Hinkov, M. Haverkort, M. Minola, M. Bakr, K. Zhou, S. Blanco-Canosa *et al.*, Nature Phys. **7**, 725 (2011).
[11] M. P. M. Dean, A. J. A. James, R. S. Springell, X. Liu, C. Monney, K. J. Zhou, R. M. Konik, J. S. Wen, Z. J. Xu, G. D. Gu, V. N. Strocov, T. Schmitt, and J. P. Hill, Phys. Rev. Lett. **110**, 147001 (2013).
[12] M. Minola, G. Dellea, H. Gretarsson, Y. Y. Peng, Y. Lu, J. Porras, T. Loew, F. Yakhou, N. B. Brookes, Y. B. Huang, J. Pelliciari, T. Schmitt, G. Ghiringhelli, B. Keimer, L. Braicovich, and M. Le Tacon, Phys. Rev. Lett. **114**, 217003 (2015).
[13] M. Minola, Y. Lu, Y. Y. Peng, G. Dellea, H. Gretarsson, M. W. Haverkort, Y. Ding, X. Sun, X. J. Zhou, D. C. Peets, L. Chauviere, P. Dosanjh, D. A. Bonn, R. Liang, A. Damascelli, M. Dantz, X. Lu, T. Schmitt, L. Braicovich, G. Ghiringhelli, B. Keimer, and M. Le Tacon, Phys. Rev. Lett. **119**, 097001 (2017).
[14] K. Ishii, T. Tohyama, S. Asano, K. Sato, M. Fujita, S. Wakimoto, K. Tustsui, S. Sota, J. Miyawaki, H. Niwa, Y. Harada, J. Pelliciari, Y. Huang, T. Schmitt, Y. Yamamoto, and J. Mizuki, Phys. Rev. B **96**, 115148 (2017).
[15] N. Nücker, U. Eckern, J. Fink, and P. Müller, Phys. Rev. B **44**, 7155 (1991).
[16] J. Fink, M. Knupfer, S. Atzkern, and M. S. Golden, J. Electron Spectrosc. Relat. Phenom. **117–118**, 287 (2001).
[17] F. Roth, A. König, J. Fink, B. Büchner, and M. Knupfer, J. Electron Spectrosc. Relat. Phenom. **195**, 85 (2014).
[18] M. Mitrano, A. A. Husain, S. Vig, A. Kogar, M. S. Rak, S. I. Rubeck, J. Schmalian, B. Uchoa, J. Schneeloch, R. Zhong, G. D. Gu, and P. Abbamonte, Proc. Natl. Acad. Sci. U.S.A. **115**, 5392 (2018).
[19] A. A. Husain, M. Mitrano, M. S. Rak, S. Rubeck, B. Uchoa, K. March, C. Dwyer, J. Schneeloch, R. Zhong, G. D. Gu, and P. Abbamonte, Phys. Rev. X **9**, 041062 (2019).
[20] I. Bozovic, Phys. Rev. B **42**, 1969 (1990).
[21] S. Uchida, T. Ido, H. Takagi, T. Arima, Y. Tokura, and S. Tajima, Phys. Rev. B **43**, 7942 (1991).
[22] D. van der Marel, J. Supercond. **17**, 559 (2004).
[23] J. Levallois, M. K. Tran, D. Pouliot, C. N. Presura, L. H. Greene, J. N. Eckstein, J. Uccelli, E. Giannini, G. D. Gu, A. J. Leggett, and D. van der Marel, Phys. Rev. X **6**, 031027 (2016).
[24] X. Yin, C. S. Tang, S. Zeng, T. C. Asmara, P. Yang, M. A. Naradipa, P. E. Trevisanutto, T. Shirakawa, B. H. Kim, S. Yunoki *et al.*, ACS Photonics **6**, 3281 (2019).
[25] A. Nag, M. Zhu, M. Bejas, J. Li, H. C. Robarts, H. Yamase, A. N. Petsch, D. Song, H. Eisaki, A. C. Walters, M. García-Fernández, A. Greco, S. M. Hayden, and K.-J. Zhou, Phys. Rev. Lett. **125**, 257002 (2020).
[26] S. Ono, S. Komiya, and Y. Ando, Phys. Rev. B **75**, 024515 (2007).
[27] A. Fujimori, E. Takayama-Muromachi, Y. Uchida, and B. Okai, Phys. Rev. B **35**, 8814 (1987).
[28] V. Emery, Phys. Rev. Lett. **58**, 2794 (1987).
[29] F. C. Zhang and T. M. Rice, Phys. Rev. B **37**, 3759 (1988).
[30] C. T. Chen, F. Sette, Y. Ma, M. S. Hybertsen, E. B. Stechel, W. M. C. Foulkes, M. Schluter, S.-W. Cheong, A. S. Cooper, L. W. Rupp, Jr., B. Batlogg, Y. L. Soo, Z. H. Ming, A. Krol, and Y. H. Kao, Phys. Rev. Lett. **66**, 104 (1991).
[31] P. Abbamonte, L. Venema, A. Rusydi, G. Sawatzky, G. Logvenov, and I. Bozovic, Science **297**, 581 (2002).
[32] L. H. Tjeng, C. T. Chen, and S.-W. Cheong, Phys. Rev. B **45**, 8205(R) (1992).
[33] M. Hashimoto, I. M. Vishik, R.-H. He, T. P. Devereaux, and Z.-X. Shen, Nature Phys. **10**, 483 (2014).

[34] C.-C. Chen, M. Sentef, Y. F. Kung, C. J. Jia, R. Thomale, B. Moritz, A. P. Kampf, and T. P. Devereaux, Phys. Rev. B **87**, 165144 (2013).
[35] S. Komiya, Y. Ando, X. F. Sun, and A. N. Lavrov, Phys. Rev. B **65**, 214535 (2002).
[36] S. Komiya, H.-D. Chen, S.-C. Zhang, and Y. Ando, Phys. Rev. Lett. **94**, 207004 (2005).
[37] H. Kanai, J. Mizusaki, H. Tagawa, S. Hoshiyama, K. Hirano, K. Fujita, M. Tezuka, and T. Hashimoto, J. Solid State Chem. **131**, 150 (1997).
[38] H. Takagi, T. Ido, S. Ishibashi, M. Uota, S. Uchida, and Y. Tokura, Phys. Rev. B **40**, 2254 (1989).
[39] A. Singh, H. Huang, Y. Chu, C. Hua, S. Lin, H. Fung, H. Shiu, J. Chang, J. Li, J. Okamoto *et al.*, J. Synchrotron Radiat. **28**, 977 (2021).
[40] C. T. Chen, L. H. Tjeng, J. Kwo, H. L. Kao, P. Rudolf, F. Sette, and R. M. Fleming, Phys. Rev. Lett. **68**, 2543 (1992).
[41] T. Nomura and J.-I. Igarashi, Phys. Rev. B **71**, 035110 (2005).
[42] R. S. Markiewicz and A. Bansil, Phys. Rev. Lett. **96**, 107005 (2006).
[43] R. S. Markiewicz, M. Z. Hasan, and A. Bansil, Phys. Rev. B **77**, 094518 (2008).
[44] K. Sturm, Z. für Naturforsch. A **48**, 233 (1993).
[45] F. Aryasetiawan and S. Biermann, Phys. Rev. Lett. **100**, 116402 (2008).
[46] S. Sahrakorpi, R. S. Markiewicz, H. Lin, M. Lindroos, X. J. Zhou, T. Yoshida, W. L. Yang, T. Kakeshita, H. Eisaki, S. Uchida, S. Komiya, Y. Ando, F. Zhou, Z. X. Zhao, T. Sasagawa, A. Fujimori, Z. Hussain, Z.-X. Shen, and A. Bansil, Phys. Rev. B **78**, 104513 (2008).
[47] C. Lane, Phys. Rev. B **101**, 235138 (2020).
[48] R. S. Markiewicz, S. Sahrakorpi, M. Lindroos, H. Lin, and A. Bansil, Phys. Rev. B **72**, 054519 (2005).
[49] R. Markiewicz, I. Buda, P. Mistark, C. Lane, and A. Bansil, Sci. Rep. **7**, 44008 (2017).
[50] R. S. Markiewicz and A. Bansil, Phys. Rev. B **75**, 020508(R) (2007).
[51] C. Lane, J. W. Furness, I. G. Buda, Y. Zhang, R. S. Markiewicz, B. Barbiellini, J. Sun, and A. Bansil, Phys. Rev. B **98**, 125140 (2018).
[52] J. W. Furness, Y. Zhang, C. Lane, I. G. Buda, B. Barbiellini, R. S. Markiewicz, A. Bansil, and J. Sun, Commun. Phys. **1**, 11 (2018).
[53] H. Y. Huang, A. Singh, C. Y. Mou, S. Johnston, A. F. Kemper, J. van den Brink, P. J. Chen, T. K. Lee, J. Okamoto, Y. Y. Chu, J. H. Li, S. Komiya, A. C. Komarek, A. Fujimori, C. T. Chen, and D. J. Huang, Phys. Rev. X **11**, 041038 (2021).
[54] V. Bisogni, M. Moretti Sala, A. Bendounan, N. B. Brookes, G. Ghiringhelli, and L. Braicovich, Phys. Rev. B **85**, 214528 (2012).
[55] See Supplemental Material at http://link.aps.org/supplemental/10.1103/PhysRevB.105.235105 for further information about RIXS curve fitting and calculations of the dielectric function.
[56] L. Chaix, E. W. Huang, S. Gerber, X. Lu, C. Jia, Y. Huang, D. E. McNally, Y. Wang, F. H. Vernay, A. Keren, M. Shi, B. Moritz, Z.-X. Shen, T. Schmitt, T. P. Devereaux, and W.-S. Lee, Phys. Rev. B **97**, 155144 (2018).
[57] A. J. Achkar, T. Z. Regier, H. Wadati, Y.-J. Kim, H. Zhang, and D. G. Hawthorn, Phys. Rev. B **83**, 081106(R) (2011).
[58] B. Kyung, V. Hankevych, A. M. Daré, and A. M. S. Tremblay, Phys. Rev. Lett. **93**, 147004 (2004).
[59] A. Greco, H. Yamase, and M. Bejas, Phys. Rev. B **94**, 075139 (2016).
[60] T. Yoshida, X. J. Zhou, T. Sasagawa, W. L. Yang, P. V. Bogdanov, A. Lanzara, Z. Hussain, T. Mizokawa, A. Fujimori, H. Eisaki, Z.-X. Shen, T. Kakeshita, and S. Uchida, Phys. Rev. Lett. **91**, 027001 (2003).
[61] K. M. Shen, F. Ronning, D. H. Lu, W. S. Lee, N. J. C. Ingle, W. Meevasana, F. Baumberger, A. Damascelli, N. P. Armitage, L. L. Miller, Y. Kohsaka, M. Azuma, M. Takano, H. Takagi, and Z.-X. Shen, Phys. Rev. Lett. **93**, 267002 (2004).
[62] H. Eskes, L. H. Tjeng, and G. A. Sawatzky, Phys. Rev. B **41**, 288 (1990).
[63] L. J. P. Ament, M. van Veenendaal, T. P. Devereaux, J. P. Hill, and J. van den Brink, Rev. Mod. Phys. **83**, 705 (2011).

What can we learn from the nickelate vs. cuprate phase diagrams?

Character of the "normal state" of the nickelate superconductors
Authors: Kyuho Lee, Bai Yang Wang, Motoki Osada, Berit H. Goodge, Tiffany C. Wang, Yonghun Lee, Shannon Harvey, Woo Jin Kim, Yijun Yu, Chaitanya Murthy, Srinivas Raghu, Lena F. Kourkoutis, and Harold Y. Hwang
arXiv:2203.02580

Recommended with a Commentary by Atsushi Fujimori, National Tsunghua University

The recent discovery of superconductivity in the infinite-layer nickelate $Nd_{1-x}Sr_xNiO_2$ [1] has attracted tremendous interest because the superconductivity occurs in the hole-doped square lattice of the Ni^+ ions, which have the same d^9 configuration as the Cu^{2+} ions in the cuprates. Therefore, information from the nickelates, namely, similarities to and differences from the cuprates, will help us to elucidate the mechanisms of the superconductivity and the unusual normal-state properties of the cuprates from new perspectives. For such purposes, experimental data from nickelates with as high quality as those from the cuprates are indispensable. In a recent breakthrough in the $Nd_{1-x}Sr_xNiO_2$ thin-film synthesis using $(LaAlO_3)_{0.3}(Sr_2TaAlO_6)_{0.7}$ (LSAT) substrates, the growth and reduction conditions were optimized and extended defects were eliminated, as reported in the recommended paper. This allowed the authors of the paper to investigate the intrinsic transport properties of $Nd_{1-x}Sr_xNiO_2$.

The recommended paper reports similarities between the nickelates and cuprates, including the *strange metal* behaviors, $\rho(T) \propto T$, near a quantum critical point (QCP) buried behind the superconducting dome (T_c dome). Here, the temperature at which the resistivity upturn occurs decreases with x and goes to zero at the QCP. This similarity between the nickelates and cuprates is remarkable considering the differences between the two systems such as the Mott-Hubbard- *versus* charge-transfer-type electronic structures [2] and the single-band *versus* multi-band structures [3, 4]. In particular, in spite of the fact that the parent compounds of the nickelates are metals due to the presence of electron pockets, the phase diagram is qualitatively similar to that of the cuprates, as shown in Fig. 1.

Furthermore, the differences between the two systems are even more intriguing. Compared to the cuprates, the nickelate show the following features:

(i) The T_c dome is shifted toward higher hole concentrations by $x \sim 0.05$.

(ii) The QCP is shifted toward a lower hole concentration from $x \sim$ 0.19-0.20 to 0.16.

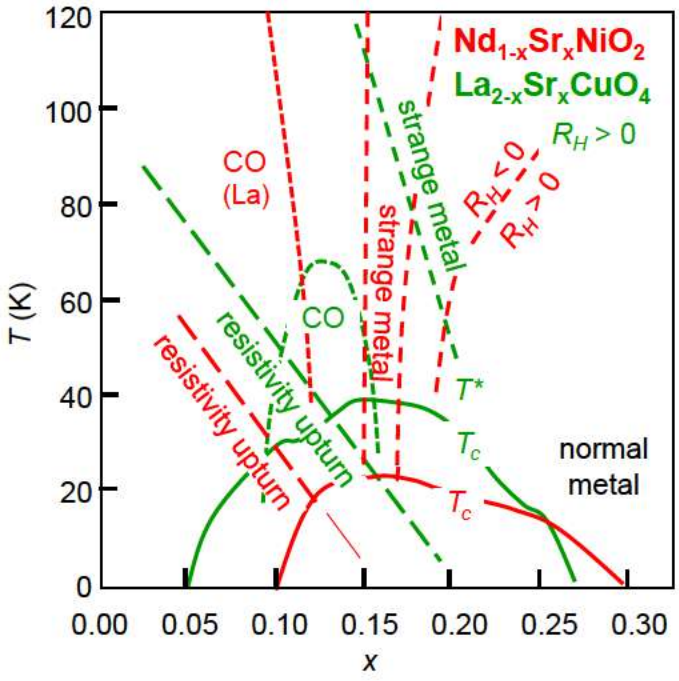

Figure 1: Phase diagram of $Nd_{1-x}Sr_xNiO_2$ (red) compared with that of the cuprate $La_{2-x}Sr_xCuO_4$ (LSCO, green) reported in the recommended paper. The charge-ordered (CO) phase of $La_{1-x}Sr_xNiO_2$ has been adopted from Ref. [5]. As for LSCO, the strange metal phase which appears above the pseudogap temperature T^* is taken from Refs. [6–8], and the CO phase from Ref. [9]. The resistivity upturn below T_c for LSCO has been measured under high magnetic fields, where the superconductivity is suppressed [10]

As for (i), if T_c is determined by the density of holes in the $d_{x^2-y^2}$ band, the presence of the electron pockets would increase the hole density and would shift the T_c dome toward lower x. It appears that, on the contrary, the presence of the electron pockets depletes the holes in the $d_{x^2-y^2}$ band, possibly through the formation of electron-hole pairs or excitons. The sign change of the Hall coefficient R_H in the overdoped region (Fig. 1) would reflect the shrinkage of the electron pockets and the recovery of the hole density with increasing x.

As for (ii), one should know first why the resistivity upturn occurs in the two systems. In the recommended paper, it is pointed out that the upturn cannot be explained by an extrinsic effect such as disorder but by an intrinsic electron correlation effect such as charge order (CO). Figure 1 shows that the CO occurs at lower x in the nickelates [5] than in the cuprates [9], which is correlated with the different QCP positions between the two systems. This in turn suggests that CO plays a role in the formation of the QCP. The CO scenario is consistent with the observation that the QCP occurs universally at $x = 0.19-0.20$ in various cuprates in spite

of the varying Fermi-surface shapes and topologies [11]. Other kinds of symmetry breaking such as time-reversal symmetry breaking (TRSB) [12] and rotational symmetry breaking (RSB) [13] have also been proposed as the origin of the QCP at $x = 0.19 - 0.20$ in the cuprates. The latter scenarios have been tested by various experimental methods including Kerr rotation for TRSB [14] and elasto-resistivity for RSB [15]. Similar experiments are highly desired for the nickelates.

Now the recommended paper has given much deeper insight into the physics of the nickelates than before, the next step would be to apply low energy spectroscopic tools such as ARPES and STM/STS. As for the cuprates, at least for LSCO, transport and spectroscopy show anomalies at the same "pseudogap" temperature T^* [7,8] (Fig. 1). Studies on nickelates using ARPES and/or STM/STS are challenging but will make the second breakthrough.

From the chemistry point of view, the difficulties in the synthesis of the superconducting nickelates compared to the cuprates would be due to the unusual valence state of Ni^+. In order to deduce electronic structure parameters such as the on-site Coulomb energy U and the p-to-d charge-transfer energy Δ, and hence the Mott-Hubbard *versus* charge-transfer character [2], core-level photoemission spectroscopy combined with model calculations is more accurate than x-ray absorption spectroscopy and inelastic x-ray scattering [16]. The new high-quality thin films will allow one to perform bulk-sensitive hard x-ray core-level photoemission and will give us a more quantitative information about chemical bonding in the nickelates.

References

[1] D. Li, K. Lee, B. Y. Wang, M. Osada, S. Crossley, H. R. Lee, Y. Cui, Y. Hikita, and H. Y. Hwang, Nature **572**, 624 (2019).

[2] M. Jiang, M. Berciu, and G. A. Sawatzky, Phys. Rev. Lett. **124**, 207004 (2020).

[3] H. Sakakibara, H. Usui, K. Suzuki, T. Kotani, H. Aoki, and K. Kuroki, Phys. Rev. Lett. **125**, 077003 (2020).

[4] C.-J. Kang and G. Kotliar, Phys. Rev. Lett. **126**, 127401 (2021).

[5] M. Rossi, M. Osada, J. Choi, S. Agrestini, D. Jost, Y. Lee, H. Lu, B. Y. Wang, K. Lee, A. Nag, Y.-D. Chuang, C.-T. Kuo, S.-J. Lee, B. Moritz, T. P. Devereaux, Z.-X. Shen, J.-S. Lee, K.-J. Zhou, H. Y. Hwang, W.-S. Lee, arXiv:2112.02484.

[6] H. Takagi, T. Ido, S. Ishibashi, M. Uota, S. Uchida, and Y. Tokura, Phys. Rev. B **40**, 2254 (1989).

[7] Y. Ando, S. Komiya, K. Segawa, S. Ono, and Y. Kurita, Phys. Rev. Lett. **93**, 267001 (2004).

[8] M. Hashimoto, T. Yoshida, K. Tanaka, A. Fujimori, M. Okusawa, S. Wakimoto, K. Yamada, T. Kakeshita, H. Eisaki, and S. Uchida, Phys. Rev. B **75**, 140503(R) (2007).

[9] R. Comin and A. Damascelli, Annu. Rev. Condens. Matter Phys. **7**, (2016) 369.

[10] G. S. Boebinger, Y. Ando, A. Passner, T. Kimura, M. Okuya, J. Shimoyama, K. Kishio, K. Tamasaku, N. Ichikawa, and S. Uchida, Phys. Rev. Lett. **77**, 5417 (1996).

[11] B. Keimer, S. A. Kivelson, M. R. Norman, S. Uchida, and J. Zaanen, Nature **518**, 179 (2015).

[12] C. M. Varma, Phys. Rev. Lett. **83**, 3538 (1999).

[13] Y. Huh and S. Sachdev, Phys. Rev. B **78**, 064512 (2008).

[14] R.-H. He, M. Hashimoto, H. Karapetyan, J. D. Koralek, J. P. Hinton, J. P. Testaud, V. Nathan, Y. Yoshida, H. Yao, K. Tanaka, W. Meevasana, R. G. Moore, D. H. Lu, S.-K. Mo, M. Ishikado, H. Eisaki, Z. Hussain, T. P. Devereaux, S. A. Kivelson, J. Orenstein, A. Kapitulnik, and Z.-X. Shen, Science **331**, 1579 (2011).

[15] K. Ishida, S. Hosoi, Y. Teramoto, T. Usui, Y. Mizukami, K. Itaka, Y. Matsuda, T. Watanabe, and T. Shibauchi, J. Phys. Soc. Jpn. **89**, 064707 (2020).

[16] M. Hepting, D. Li, C. J. Jia, H. Lu, E. Paris, Y. Tseng, X. Feng, M. Osada, E. Been, Y. Hikita, Y.-D. Chuang, Z. Hussain, K. J. Zhou, A. Nag, M. Garcia-Fernandez, M. Rossi, H. Y. Huang, D. J. Huang, Z. X. Shen, T. Schmitt, H. Y. Hwang, B. Moritz, J. Zaanen, T. P. Devereaux, and W. S. Lee, Nat. Mater. **19**, 381 (2020).

國立清華大學、物理學系 2022年6月1日

Open issues in high-temperature superconductors: challenges with advance spectroscopies

藤森 淳 Atsushi FUJIMORI
國立清華大學、國家同歩輻射研究中心、東京大学

NSRRC

NTHU

UTokyo

台湾-韓国-日本 強相関電子系討論会 20回!

Department of Physics Alumni, UTokyo 1974

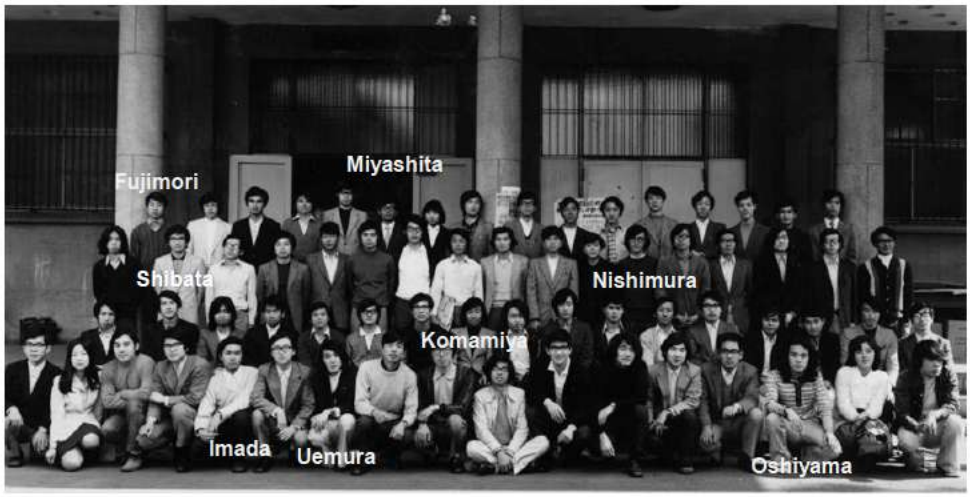

Magnetic circular dichroism (MCD) of semiconductors: Master thesis work

Designed and assembled an optical system for MCD w a supercond magnet

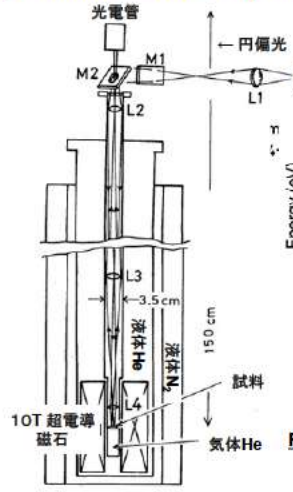

High-energy exciton

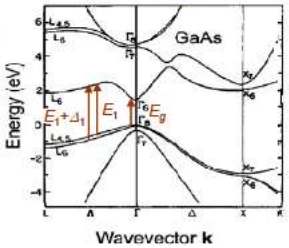

Derivation of *g* factors

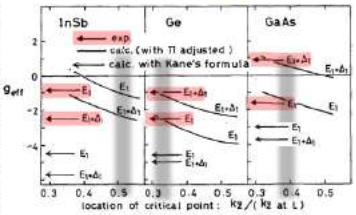

A. Fujimori, H. Fukutani & G. Kuwabara, JPSJ **45**, 910 (1978) + T. Koide.

First XMCD - Ni $M_{2,3}$ edge: T. Koide, A. Fujimori *et al.*, PRB **44**, 4697 (1991).
- Ni $L_{2,3}$ edge: C. T. Chen, F. Sette *et al.*, PRB **42**, 7262 (1990).

Prof. Sugano's course & round table on ligand-field theory

Transition-metal ion in a ligand/crystal field

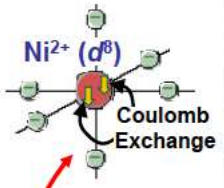

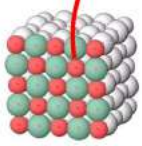

Antiferromagnetic insulator NiO

Optical transition energy (Tanabe-Sugano diagram)

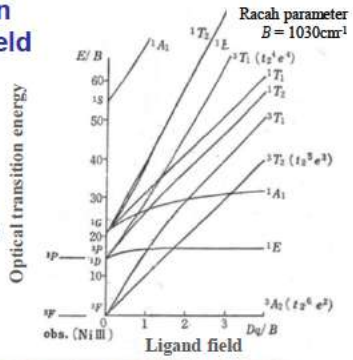

Prof. Kanamori Prof. Sugano Fujimori

Photoemission spectroscopy

Photoemission spectra

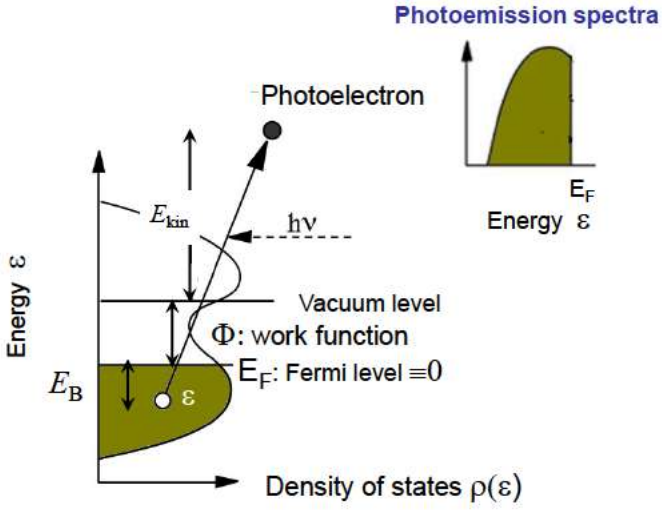

@National Institute for Research in Inorganic Materials (current NIMS)

Prof. Sugano's course & round table on ligand-field theory

Transition-metal ion in a ligand/crystal field

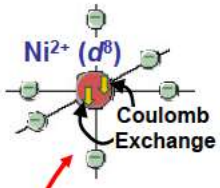

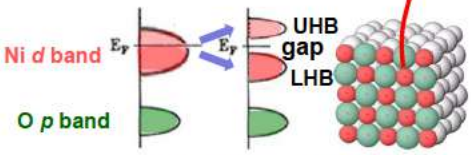

Optical transition energy (Tanabe-Sugano diagram)

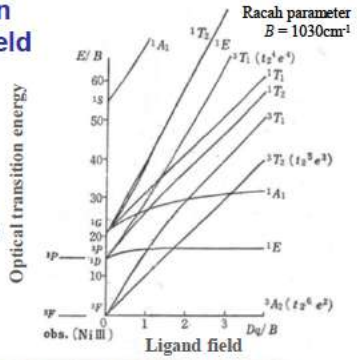

Prof. Kanamori Prof. Sugano Fujimori

Photoemission spectroscopy and cluster-model analysis of the Mott insulator NiO

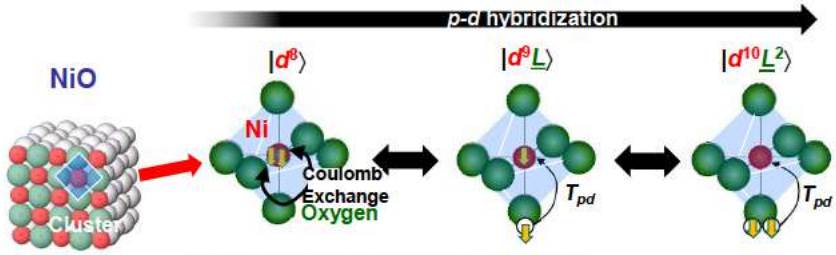

Photoemission spectra of NiO

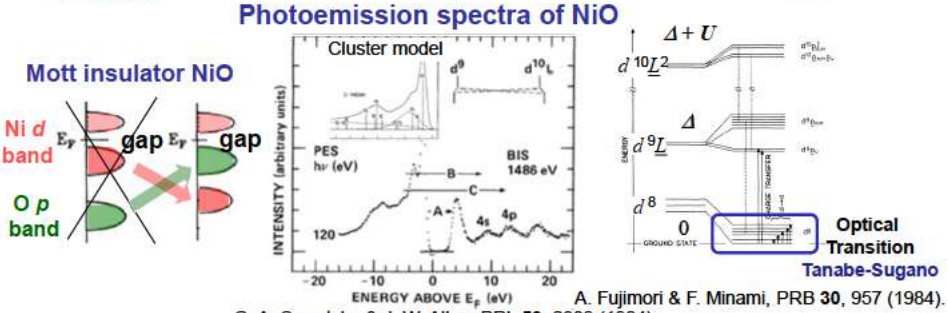

A. Fujimori & F. Minami, PRB **30**, 957 (1984).
G. A. Sawatzky & J. W. Allen, PRL **53**, 2339 (1984).

Cuprate high-temperature superconductors

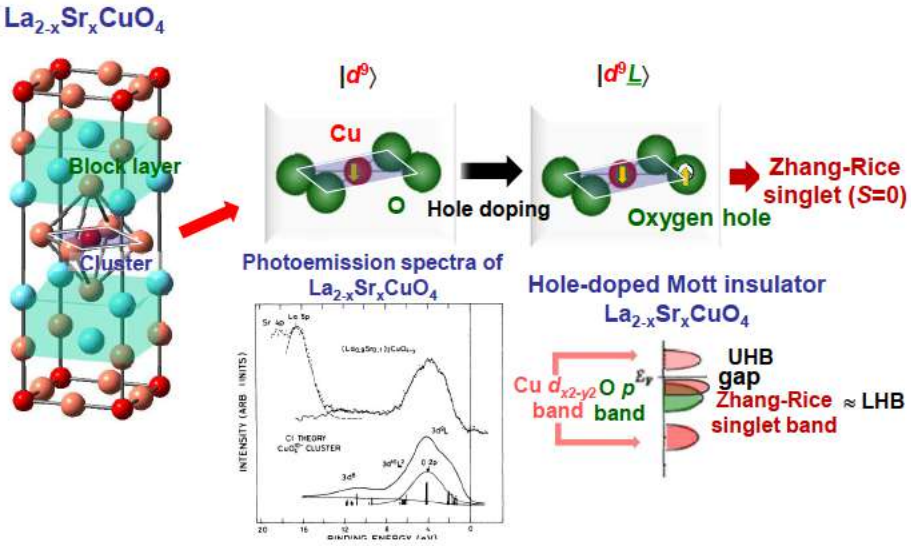

A. Fujimori, E. Takayama-Muromachi *et al.*, PRB **35**, 8814 (1987).

Zaanen-Sawatzky-Allen picture of transition-metal compounds

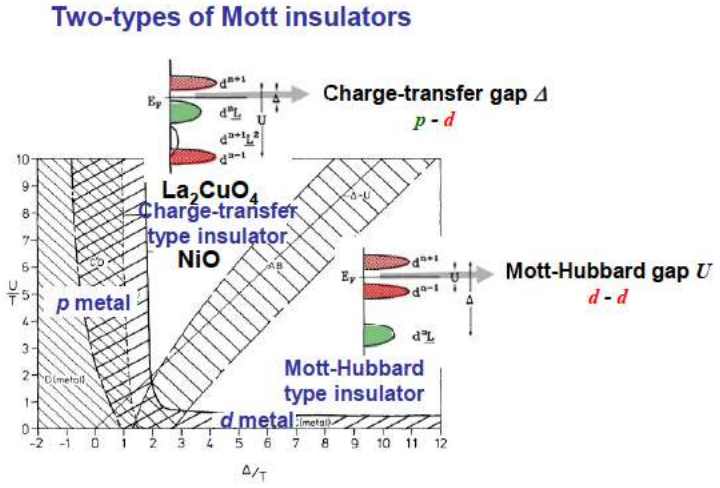

J. Zaanen, G. A. Sawatzky & J. W. Allen, PRL **55**, 418 (1985).

Outline

- **Cuprate high-T_c superconductors**
  - Pseudogap, strange metal, high-T_c mechanisms…
- **The origin of the pseudogap**
  - Superconducting fluctuations?
  - Charge order?
  - Nematicity?
  - Electron fractionalization?

Cuprate high-T_c superconductors

Discovered in 1986

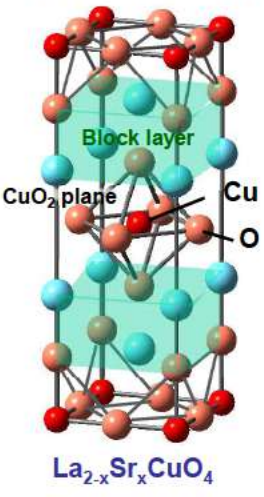

Phase diagram

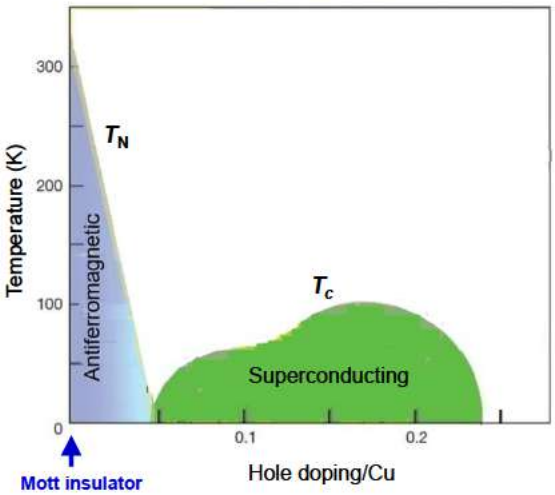

Cuprate high-T_c superconductors

Discovered in 1986

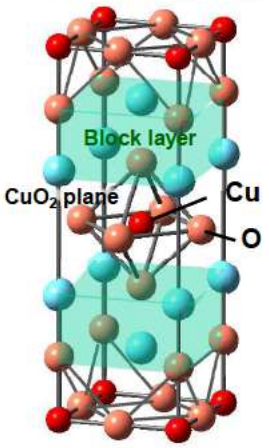

$La_{2-x}Sr_xCuO_4$

Phase diagram

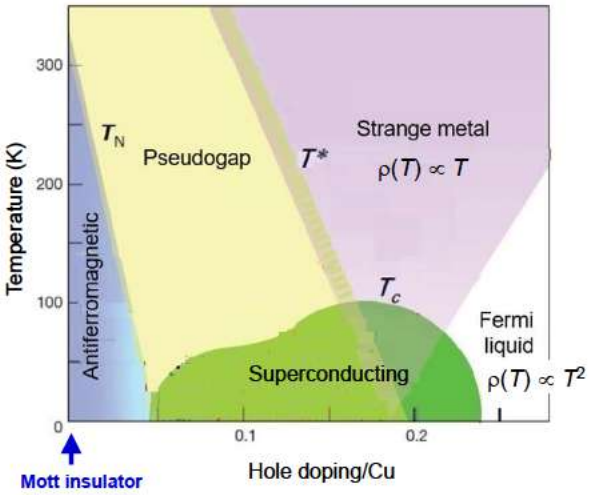

Pseudogap phenomena in cuprate high-T_c superconductors

Phase diagram

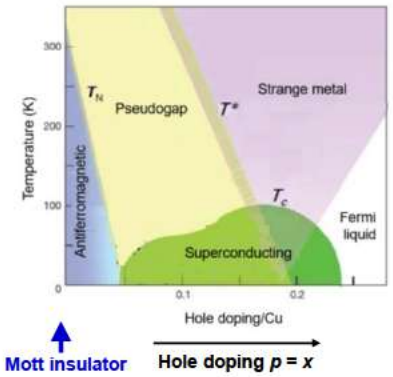

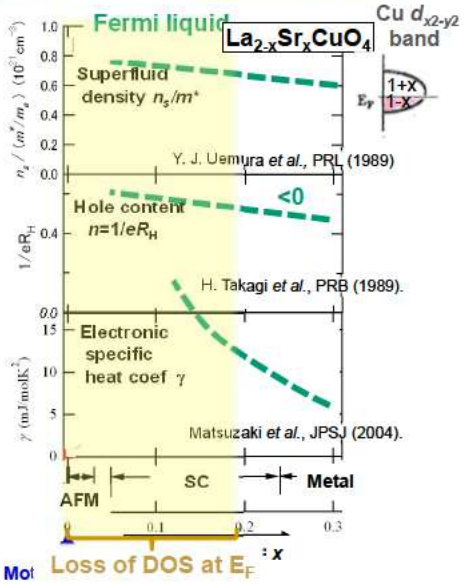

Photoemission spectroscopy

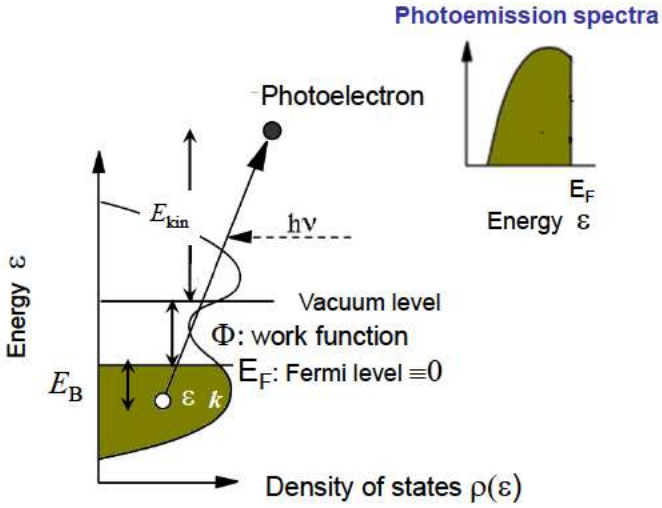

@National Institute for Research in Inorganic Materials (current NIMS)

Angle-resolved photoemission spectroscopy (ARPES)

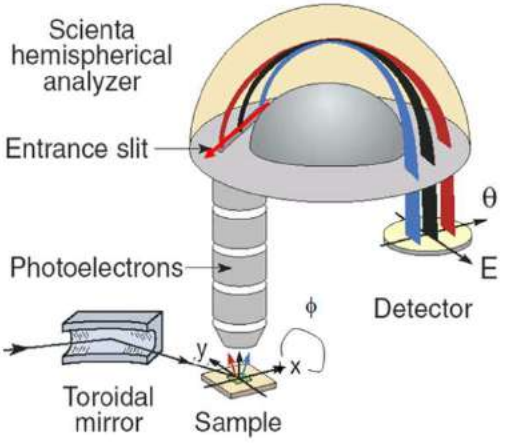

Band dispersion
$A(\mathbf{k},\varepsilon)$

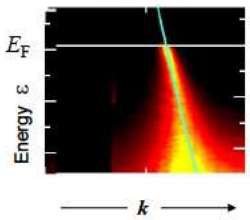

Fermi surface $A(k,\varepsilon=E_F)$

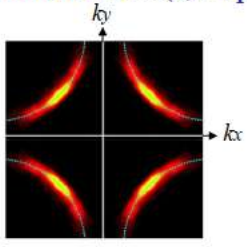

→ **Spectral function** $A(\mathbf{k},\varepsilon)$ **(**$\varepsilon<\mu$**)**

Pseudogap behavior of Fermi surface in cuprates

Fermi surface of $La_{2-x}Sr_xCuO_4$ measured by ARPES

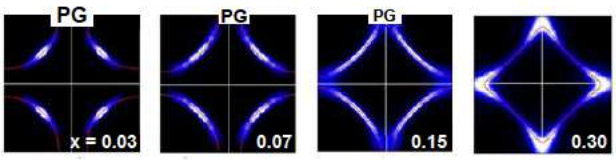

PG: Pseudogap

T. Yoshida, AF *et al.*, PRB **74**, 224510 (2006).

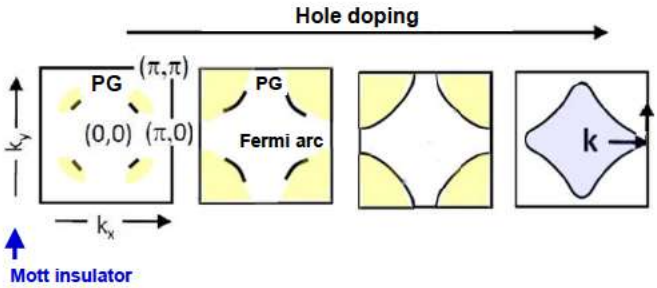

Cuprate high-T_c superconductors

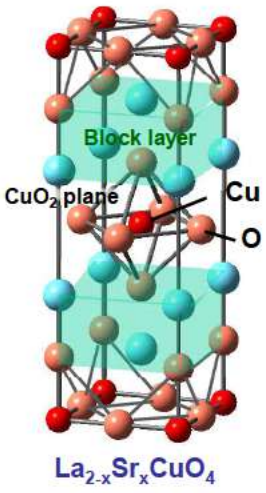

Phase diagram

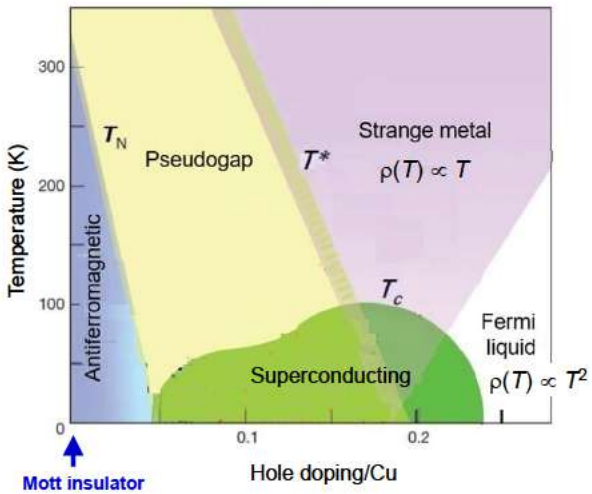

Outline

- **Cuprate high-T_c superconductors**
  - **Pseudogap, strange metal, high-T_c mechanisms…**
- **The origin of the pseudogap**
  - **Superconducting fluctuations?**
  - **Charge order?**
  - **Nematicity?**
  - **Electron fractionalization?**

Why does the pseudogap matter?

- **To understand the strange and unusual normal state**
  -- The normal state of cuprates is far more unusual than the (*d*-wave) superconducting state.

Pseudogap behavior of Fermi surface in cuprates

Fermi surface of $La_{2-x}Sr_xCuO_4$ measured by ARPES

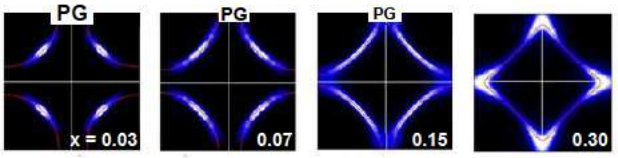

PG: Pseudogap

T. Yoshida, AF *et al.*, PRB **74**, 224510 (2006).

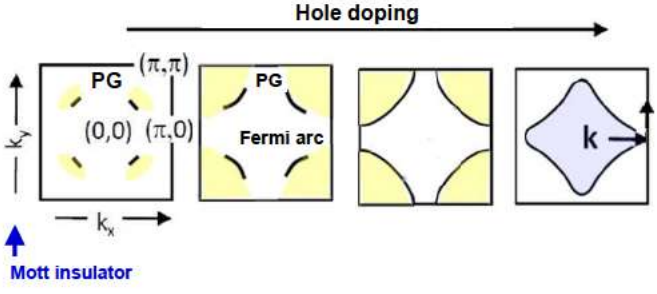

d-wave superconducting order parameter

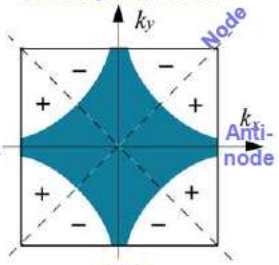

gap

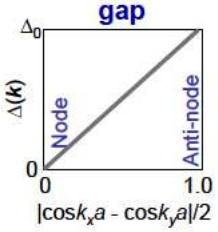

Why does the pseudogap in cuprates matter?

- To understand the strange and unusual normal state -- The normal state of cuprates is far more unusual than the (*d*-wave) superconducting state.
- To know the order parameter of the pseudogap phase, which ends at the quantum critical point (QCP) -- Quantum fluctuations of the order parameter may lead to the superconductivity.

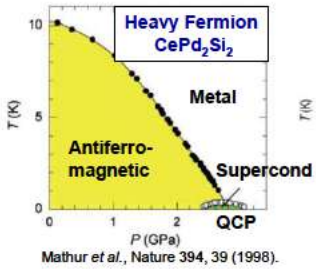

Mathur *et al.*, Nature **394**, 39 (1998).

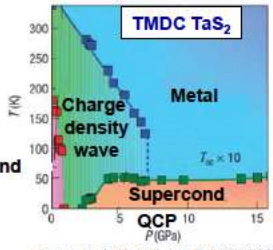

Sipos *et al.*, Nat. Mater. **7**, 960(2008).

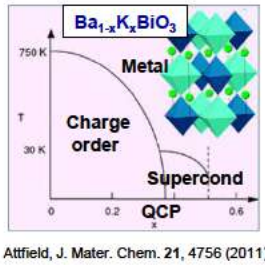

Attfield, J. Mater. Chem. **21**, 4756 (2011).

Cuprate high-T_c superconductors

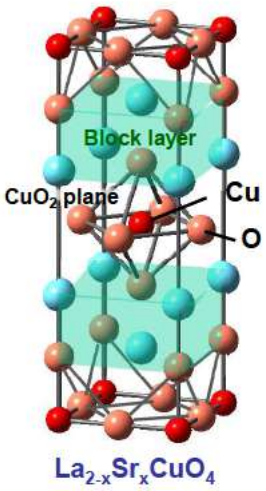

Phase diagram

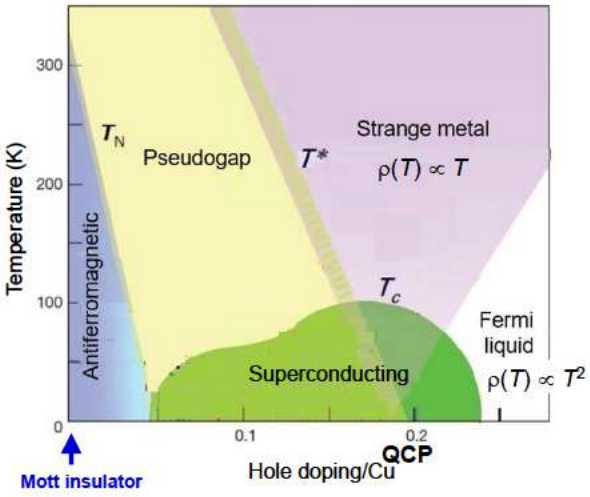

Outline

- **Cuprate high-T_c superconductors**
  - **Pseudogap, strange metal, high-T_c mechanisms …**

- **The origin of the pseudogap**
  - **Superconducting fluctuations/preformed Cooper pairs?**
  - **Charge order?**
  - **Nematicity?**
  - **Electron fractionalization?**

Cuprate high-T_c superconductors

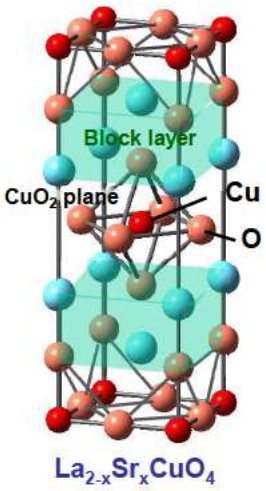

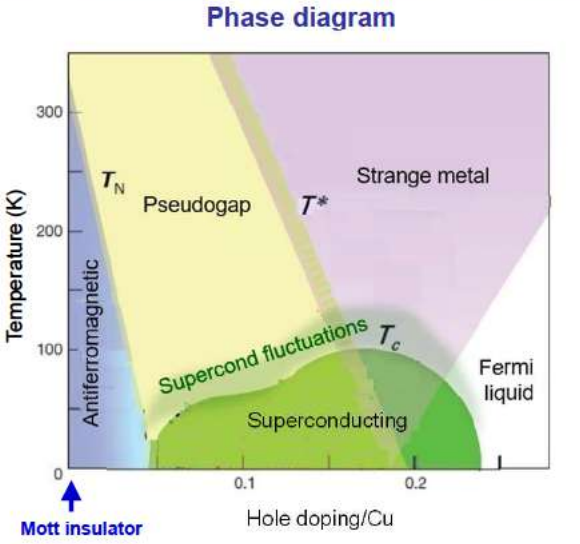

T. Usui, T. Watanabe, Y. Koike et al., JPSP **83**, 064713 (2014)

Outline

- **Cuprate high-T_c superconductors**
  - **Pseudogap, strange metal, high-T_c mechanisms …**
- **The origin of the pseudogap**
  - **Superconducting fluctuations?**
  - **Charge order?**
  - **Nematicity?**
  - **Electron fractionalization?**

Cuprate high-T_c superconductors

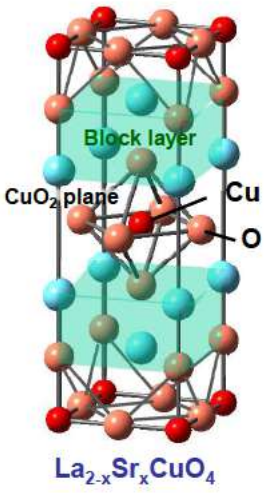

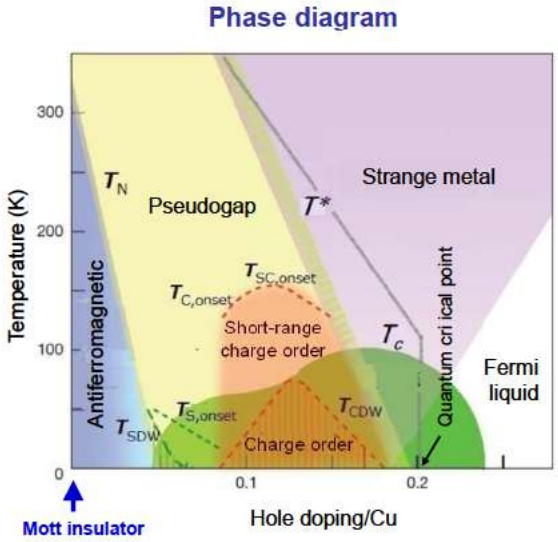

B. Keimer, S. A. Kivelson, M. R. Norman, S. Uchida & J. Zaanen, Nature **518**, 179 (2015).

Charge order

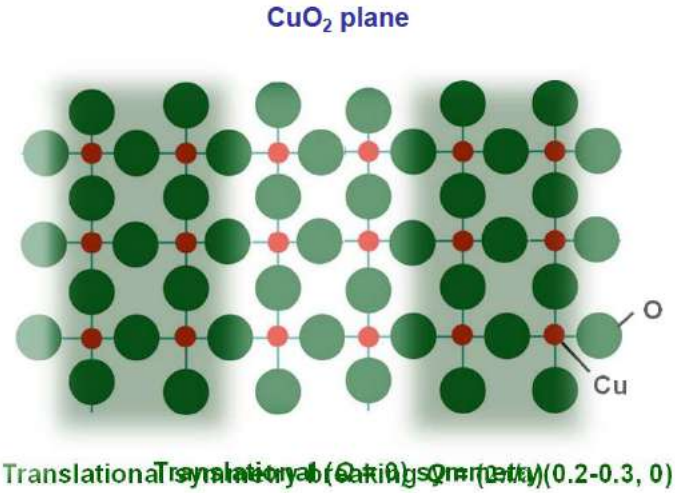

Resonant inelastic x-ray scattering (RIXS)

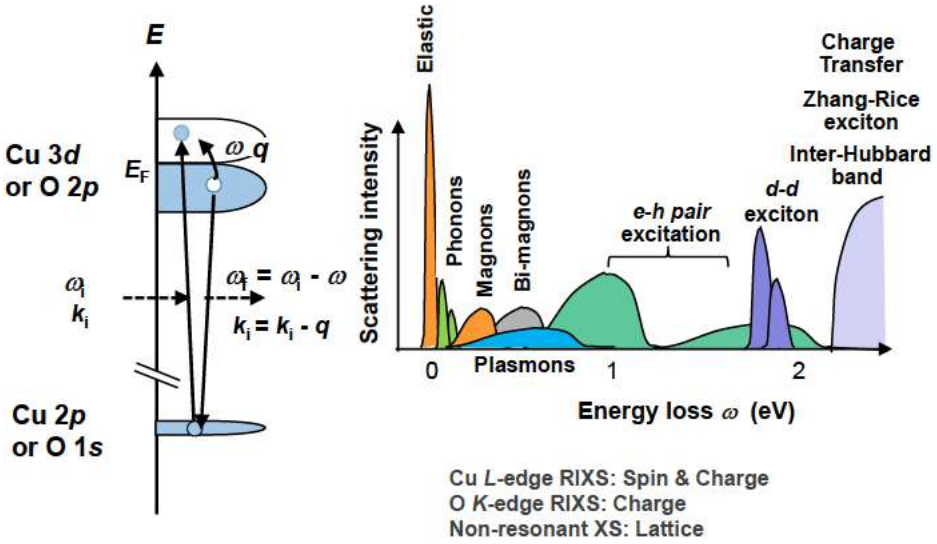

Cu *L*-edge RIXS: Spin & Charge
O *K*-edge RIXS: Charge
Non-resonant XS: Lattice

Resonant inelastic x-ray scattering (RIXS)

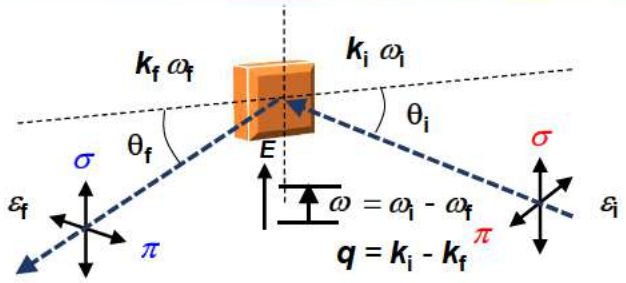

Scattering matrix element

$$f = \left(\varepsilon_f^* \cdot \varepsilon_i\right) F^{(0)} - i\left(\varepsilon_f^* \times \varepsilon_i\right) \cdot m F^{(1)} + \left(\varepsilon_f^* \cdot m\right)(\varepsilon_i \cdot m) F^{(2)}$$

Charge scat. → $\chi_c(q,\omega)$ | Magnetic scat. ∝ *m* → $\chi_s(q,\omega)$ | Magnetic scat. ∝ m^2

RIXS end-station at Taiwan Photon Source 41A

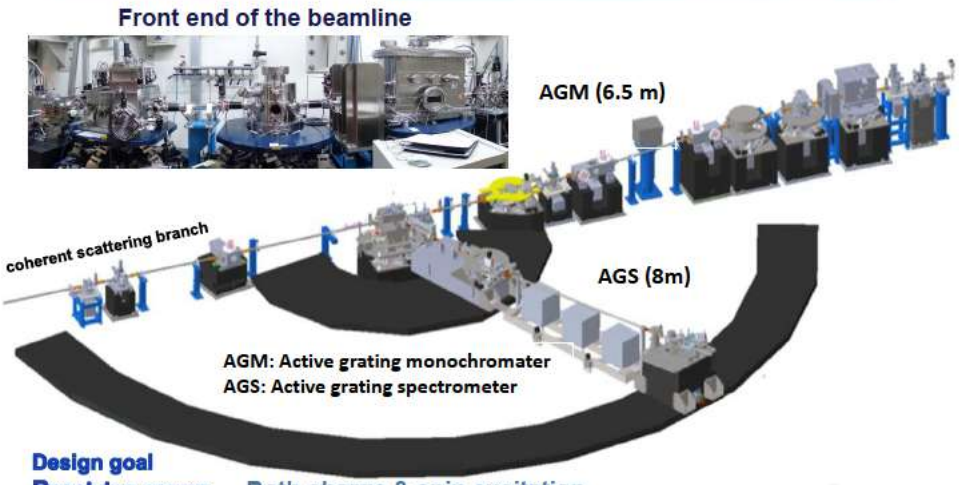

Design goal
Resolving power: Both charge & spin excitation
~43,000 (ΔE ~ 21 meV) at Cu L_3
~66,000 (ΔE ~ 8 meV) at O K (currently ~ 18 meV)

Flux ~ 7×10^{12} /sec @ 900 eV,
Beam size: 4.5 μm (H) x 5 μm (V)

Resonant inelastic x-ray scattering (RIXS)

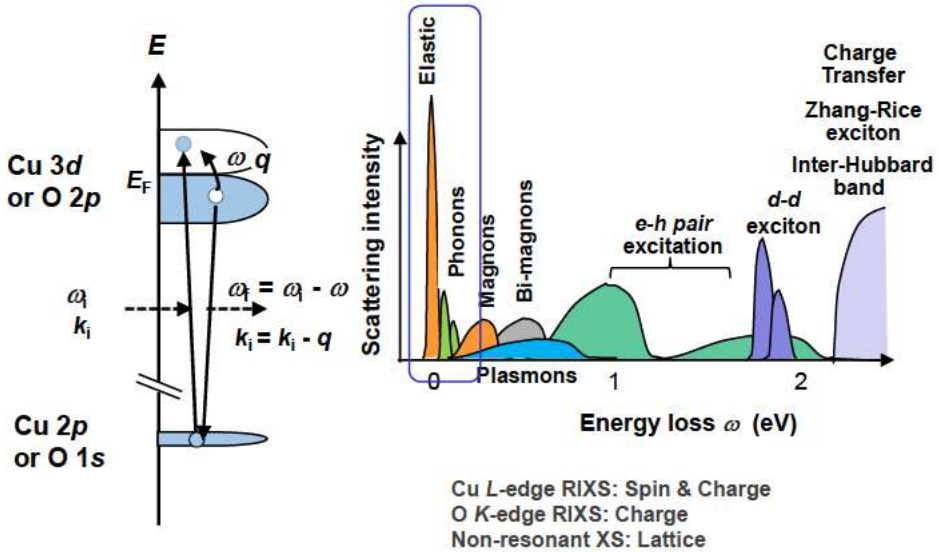

Cu *L*-edge RIXS: Spin & Charge
O *K*-edge RIXS: Charge
Non-resonant XS: Lattice

Short-range charge order detected by resonant inelastic x-ray scattering (RIXS)

RIXS from $La_{2-x}Sr_xCuO_4$ (x=0.15) at O *K* edge

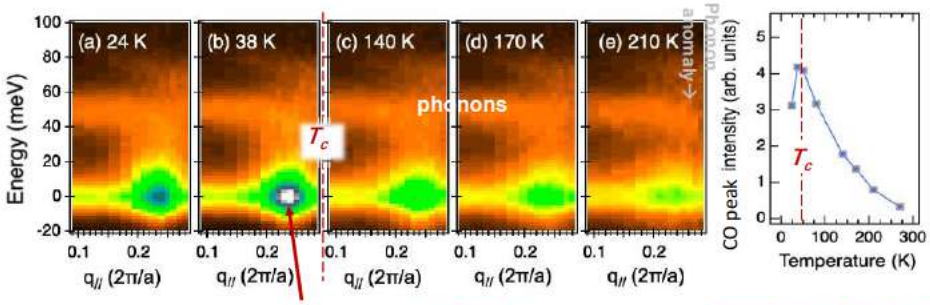

$q_{||} = Q_{CO} \sim (2\pi/a)(0.23, 0)$

→ charge period ~ $4a$

Competition between superconductivity and charge order

H. Y. Huang, A. Singh, C. Y. Mou, T. K. Lee, J. Okamoto, AF, C. T. Chen, & D. J. Huang *et al.*, PRX **11**, 041038 (2021).

Charge order order

CuO_2 plane

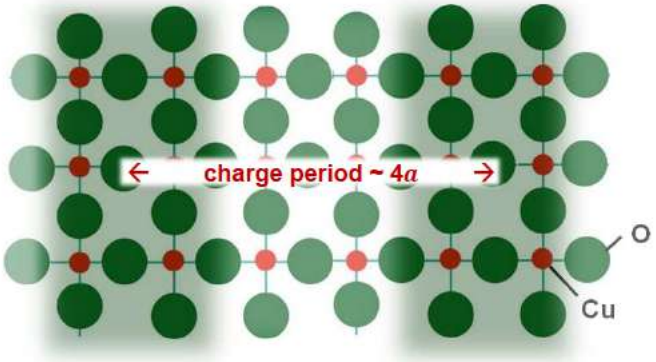

Translational symmetry breaking $Q = (2\pi/a)(0.2\text{-}0.3, 0)$

Intertwined charge density wave (CDW) and Cooper-pair density wave (PDW) orders

Spatially modulated *d*-wave SC

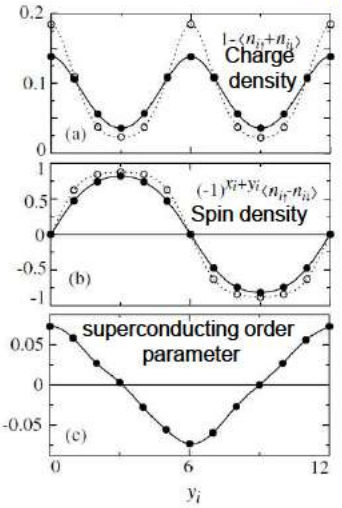

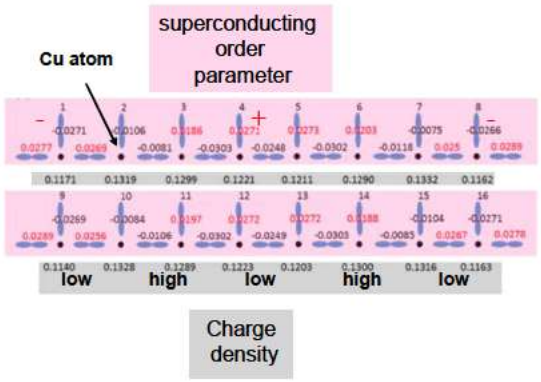

W-L. Tu and T-K Lee, Sci. Rep. **9**, 1719 (2018).

A. Himeda, T. Kato, and M. Ogata, PRL **88**, 117001 (2002).

Pseudogap behavior of Fermi surface in cuprates

Fermi surface of $La_{2-x}Sr_xCuO_4$ measured by ARPES

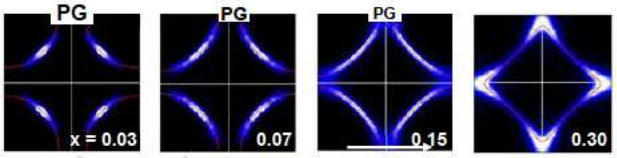

PG: Pseudogap

T. Yoshida, AF *et al.*, PRB **74**, 224510 (2006).

Hole doping

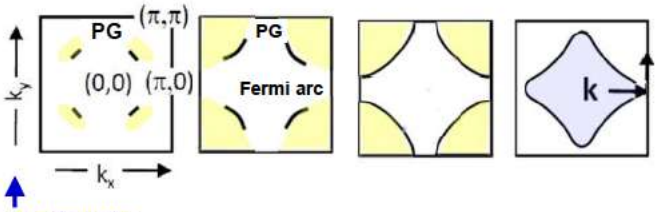

Mott insulator

***d*-wave superconducting order parameter**

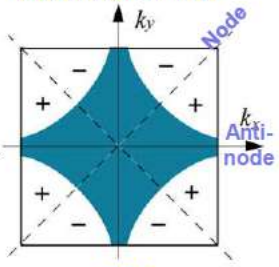

gap

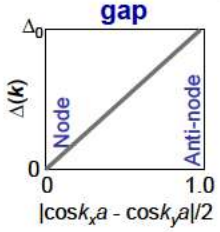

Superconducting fluctuation *versus* density order

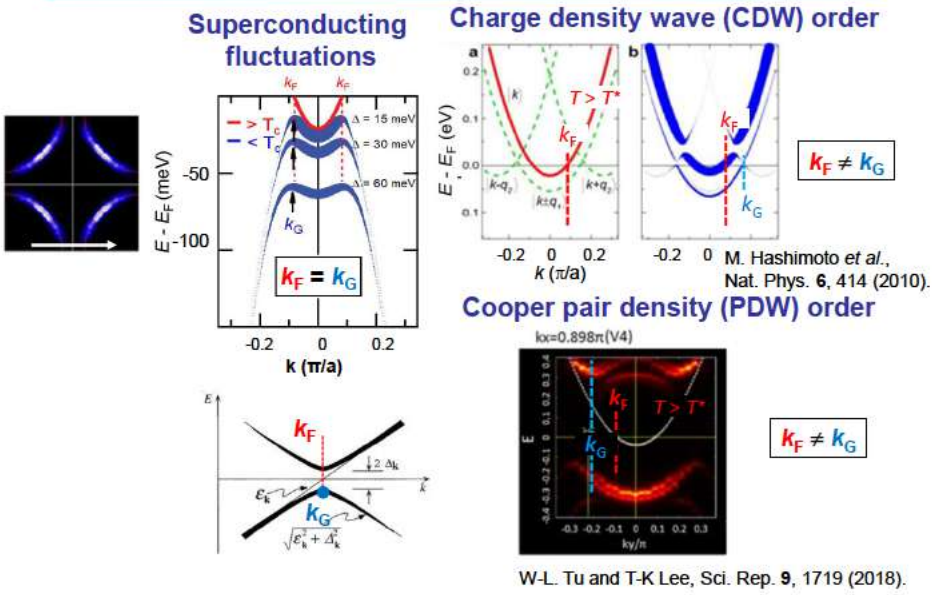

W-L. Tu and T-K Lee, Sci. Rep. **9**, 1719 (2018).

Superconducting fluctuation *versus* density order

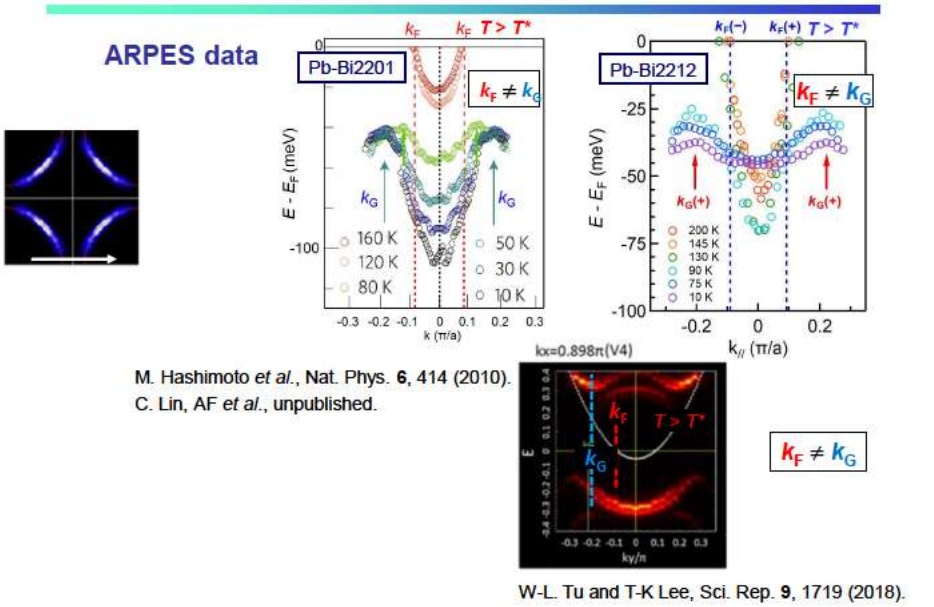

M. Hashimoto *et al.*, Nat. Phys. **6**, 414 (2010).
C. Lin, AF *et al.*, unpublished.

W-L. Tu and T-K Lee, Sci. Rep. **9**, 1719 (2018).

Charge order (plus Cooper-pair density order, spin)

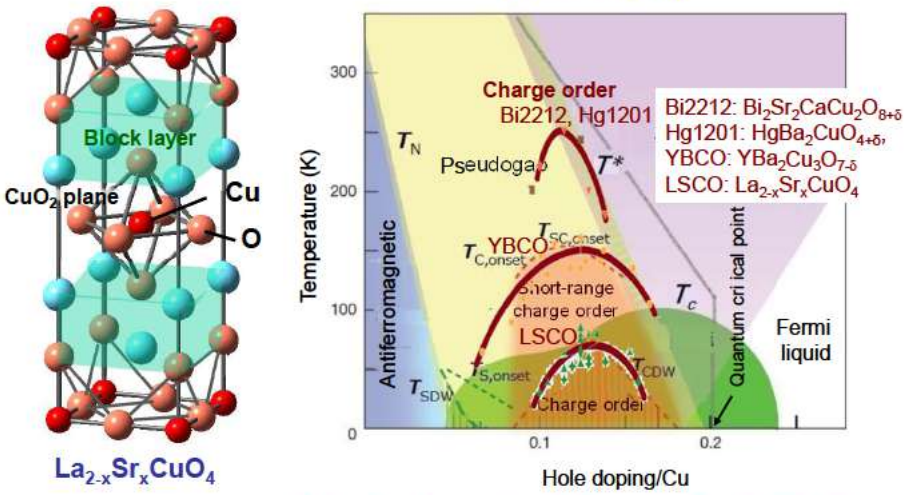

B. Keimer, S.A. Kivelson, M.R. Norman, S. Uchida & J. Zaanen, Nature 518, 179 (2015).

Outline

- **Cuprate high-T_c superconductors**
  - **Pseudogap, strange metal, high-T_c mechanisms …**
- **The origin of the pseudogap**
  - **Superconducting fluctuations?**
  - **Charge order?**
  - **Nematicity?**
  - **Electron fractionalization?**

Nematic order

CuO_2 plane

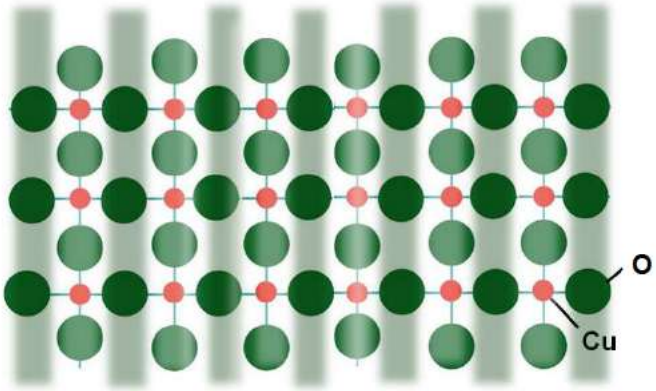

Translational (C_1) and C_4 rotational symmetry

C_4 rotational symmetry broken

Nematic order

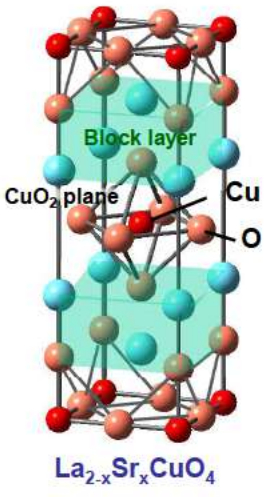

Phase diagram

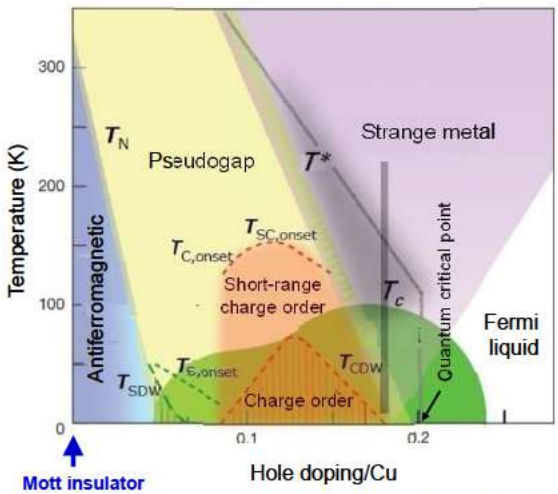

B. Keimer, S. A. Kivelson, M. R. Norman, S. Uchida & J. Zaanen, Nature **518**, 179 (2015).

ARPES of Pb-doped Bi2212 under uniaxial strain

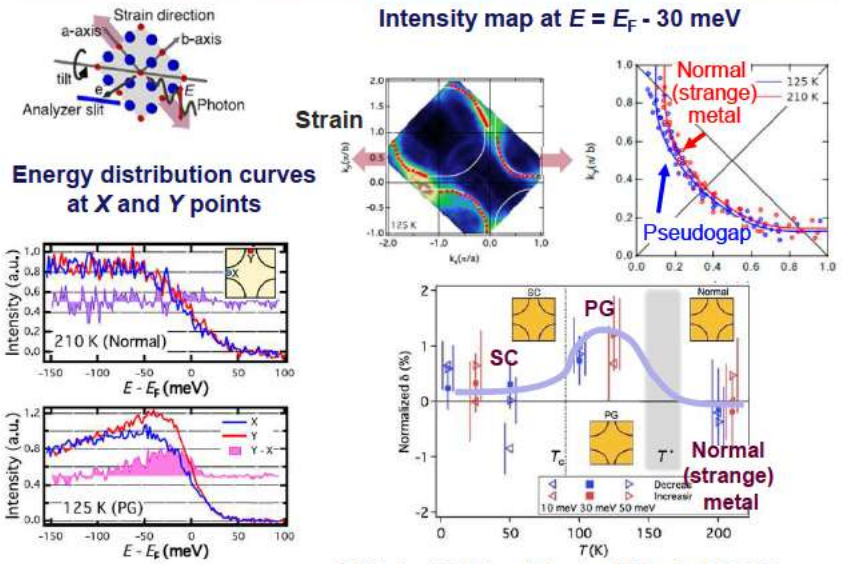

S. Nakata, AF *et al.*, npj Quantum Mater. **6**, 86 (2021).

Nematic order *vs.* charge/PDW order

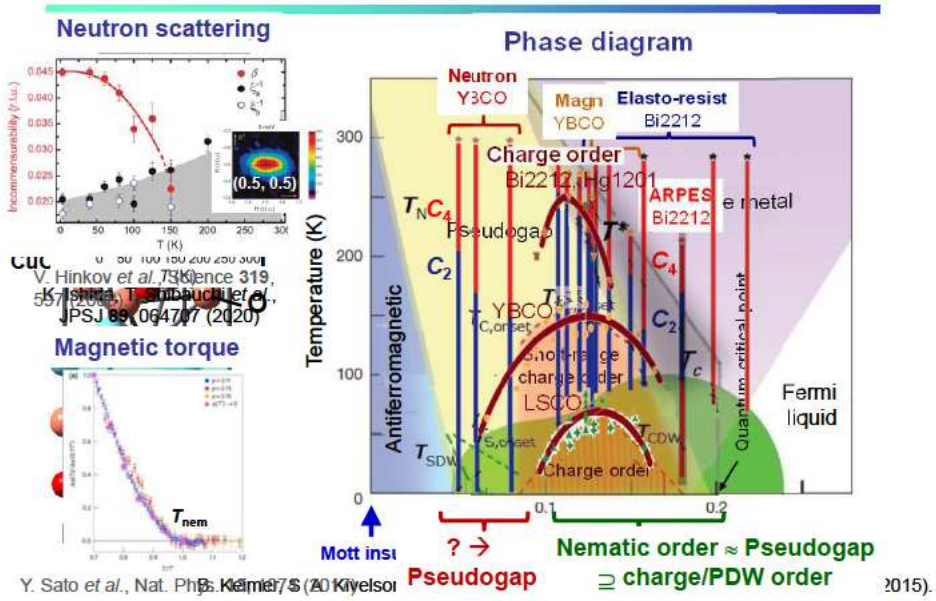

V. Hinkov *et al.*, Science **319**, 597 (2008), K. Ishida, T. Shibauchi *et al.*, JPSJ **89**, 064707 (2020)

Y. Sato *et al.*, Nat. Phys. **13**, 1074 (2017), B. Keimer, S. A. Kivelson

Outline

- **Cuprate high-T_c superconductors**
  - **Pseudogap, strange metal, high-T_c mechanisms …**
- **The origin of the pseudogap**
  - **Superconducting fluctuations?**
  - **Charge order?**
  - **Nematicity?**
  - **Electron fractionalization?**

Electron fractionalization in condensed matter

- **Spin-charge separation in quasi-one-dimensional systems**
  - **Electron → Holon & Spinon (Tomonaga-Luttinger liquid)**

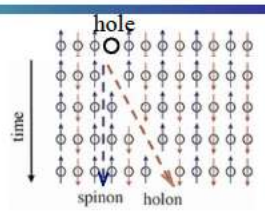

- **Fractional quantum-Hall effect (FQHE)**

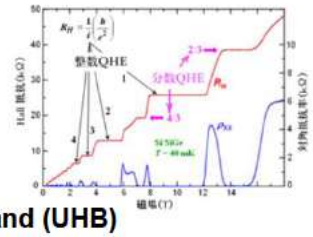

- **Mott insulator**
  - **Electron band → Upper Hubbard band (UHB) & Lower Hubbard band (LHB)**

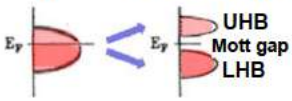

Cuprate high-temperature superconductors

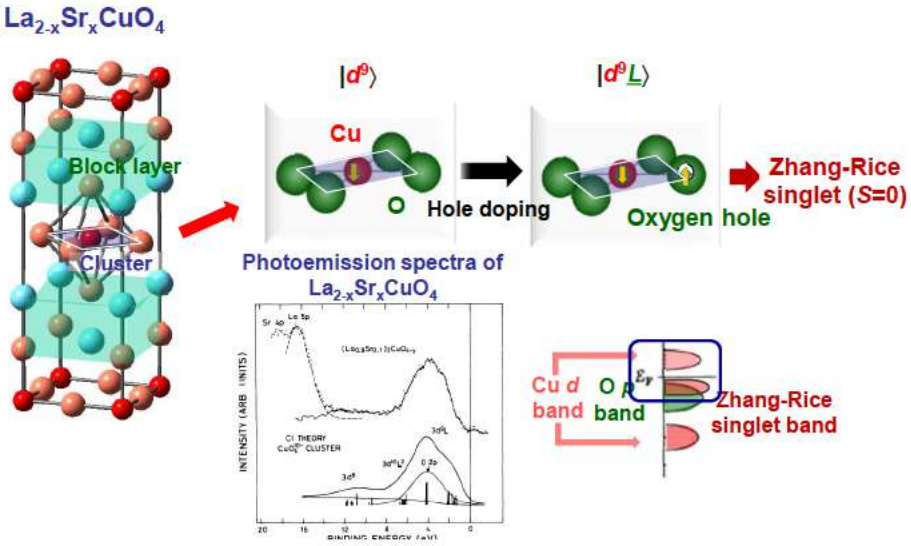

A. Fujimori, E. Takayama-Muromachi *et al.*, PRB **35**, 8814 (1987).

Electron fractionalization in condensed matter

- **Quasi-one-dimensional systems**
  - Electron → Holon & Spinon

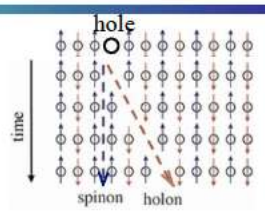

- **Fractional quantum-Hall effect (FQHE)**

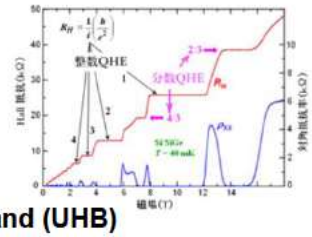

- **Mott insulator**
  - Electron band → Upper Hubbard band (UHB) & Lower Hubbard band (LHB)

- **Pseudogap**
  - LHB → In-gap band (IGB) & coherent LHB

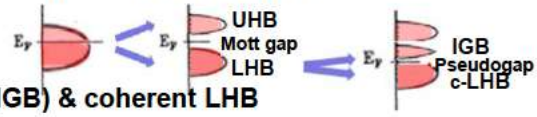

Electron fractionalization in Mott insulator and doped Mott insulator

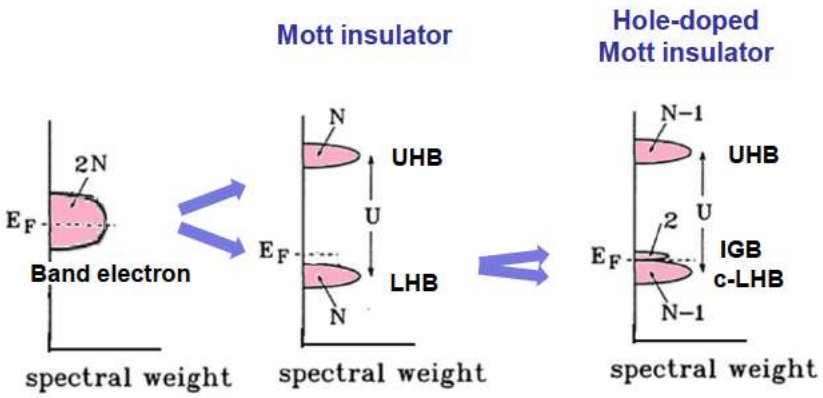

Hubbard-cluster calcula ion by:
H. Eskes, M. J. B. Meinders & G A. Sawatzky, PRL **67**, 1035 (1991).

Electron fractionalization in Mott insulator and doped Mott insulator

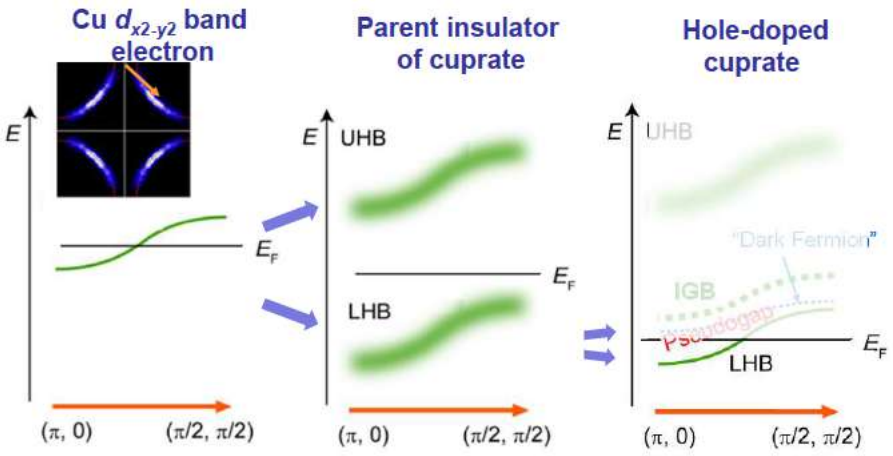

Cluster DMFT calculation: S. Sakai, M. Imada *et al.*, PRL **111**, 107001 (2013).

Electron fractionalization in doped Mott insulator - ARPES of electron-doped cuprates

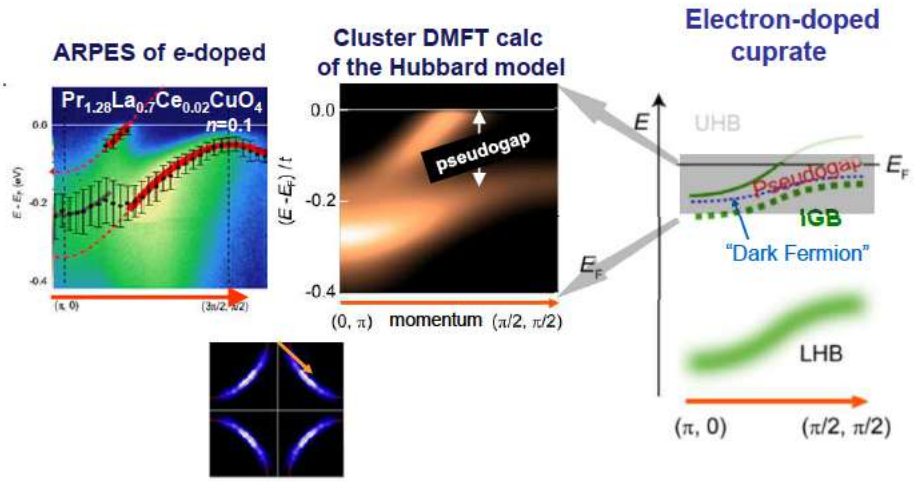

Cluster DMFT calculation: S. Sakai, M. Imada *et al.*, PRL **111**, 107001 (2013).
M. Horio, S. Sakai, M. Imada, T. Adachi, Y. Koike, AF *et al.*, arXiv:1801.04247

Electron fractionalization in doped Mott insulator - RIXS of hole-doped cuprates

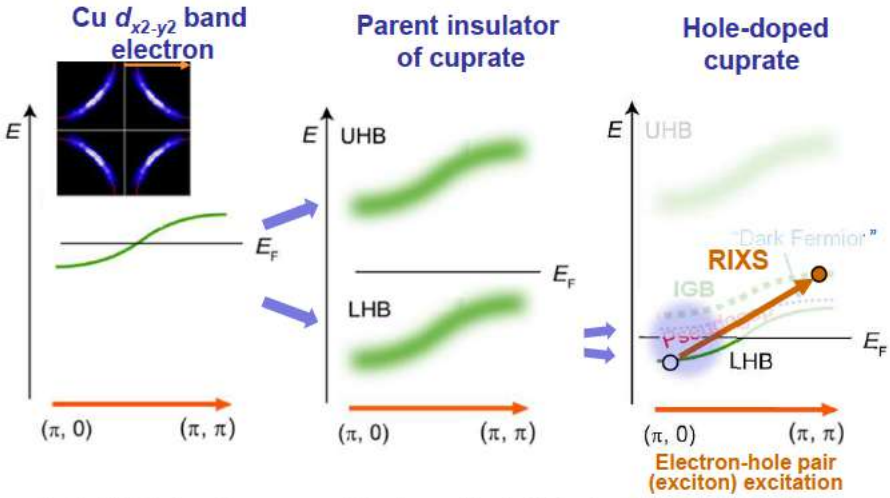

Cluster DMFT calc → Two-component Fermion model calc: M. Imada, JPSJ **90**, 074702 (2021).

Pseudogap behavior of Fermi surface in cuprates

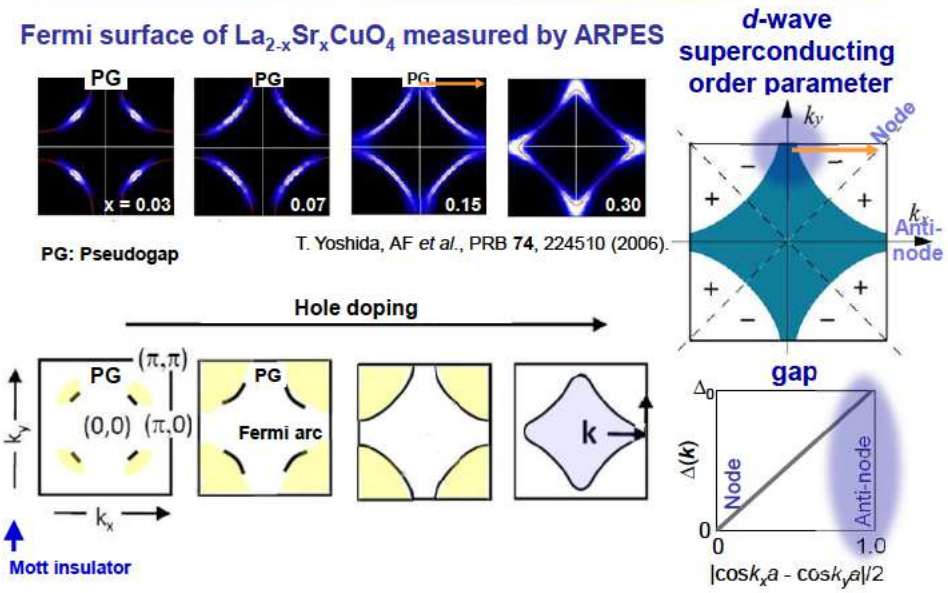

Electron fractionalization in doped Mott insulator - RIXS of hole-doped cuprates

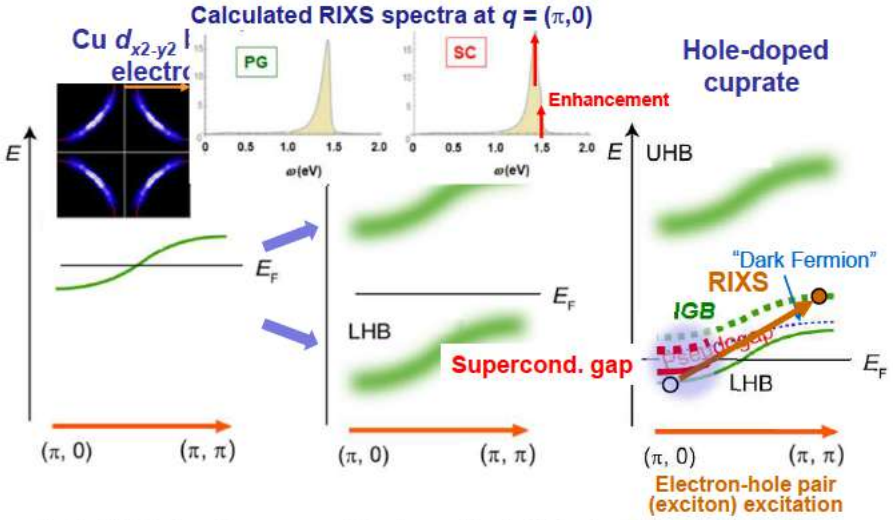

Cluster DMFT calc → Two-component Fermion model calc: M. Imada, JPSJ **90**, 074702 (2021).

Resonant inelastic x-ray scattering (RIXS)

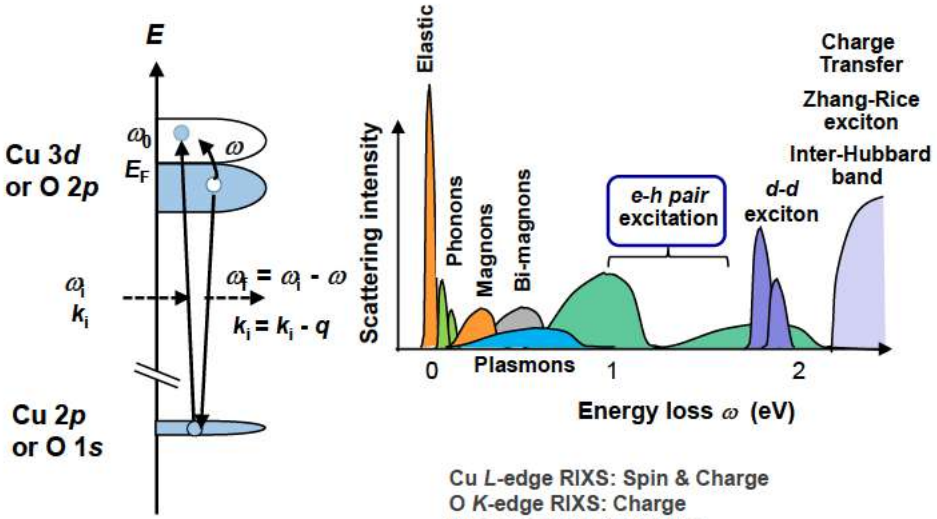

Cu *L*-edge RIXS: Spin & Charge
O *K*-edge RIXS: Charge
Non-resonant XS: Lattice

Electron fractionalization in doped Mott insulator - Electron-hole pair (exciton) excitation in RIXS

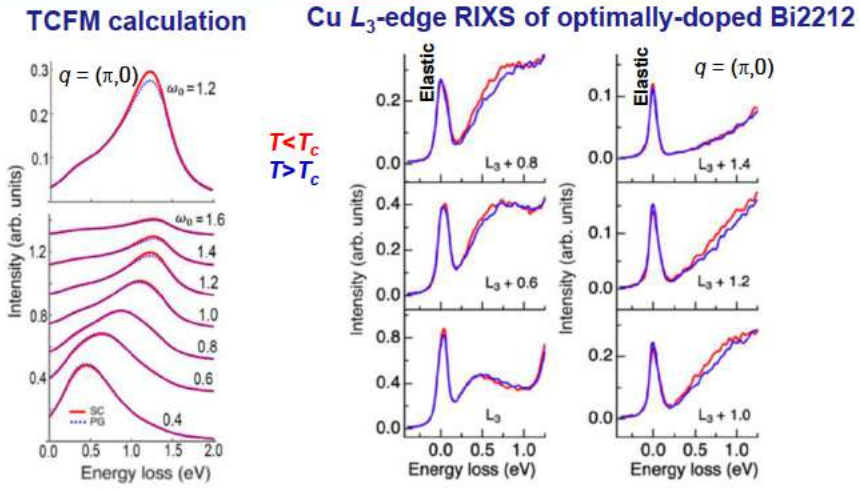

Cluster DMFT calc → Two-component Fermion model (TCFM) calc: M. Imada, JPSJ **90**, 074702 (2021).
Experiment: A. Singh, H. Y. Huang, J. D. Xie, J. Okamoto, C. T. Chen, T. Watanabe, AF, M. Imada, and D. J. Huang, submitted.

Electron fractionalization in doped Mott insulator - RIXS of hole-doped cuprates

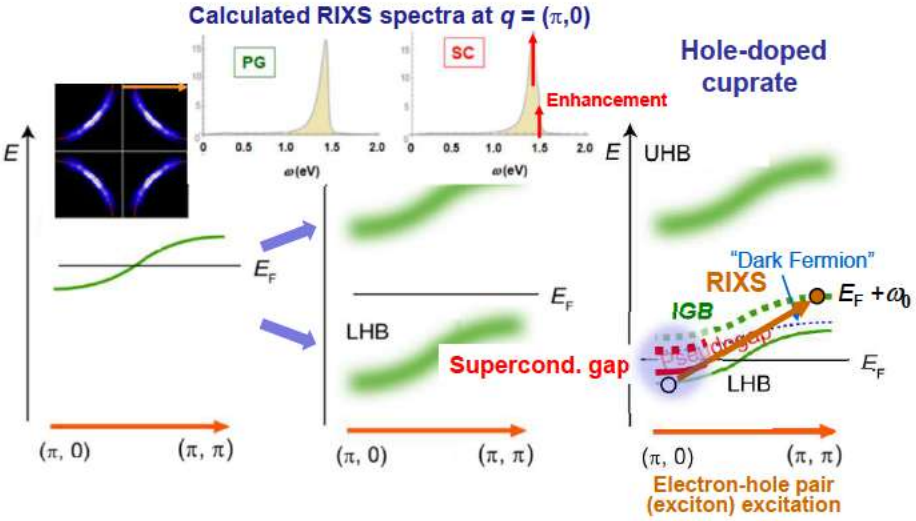

Cluster DMFT calc → Two-component Fermion model calc: M. Imada, JPSJ **90**, 074702 (2021).

Nematic order *vs.* charge/PDW order

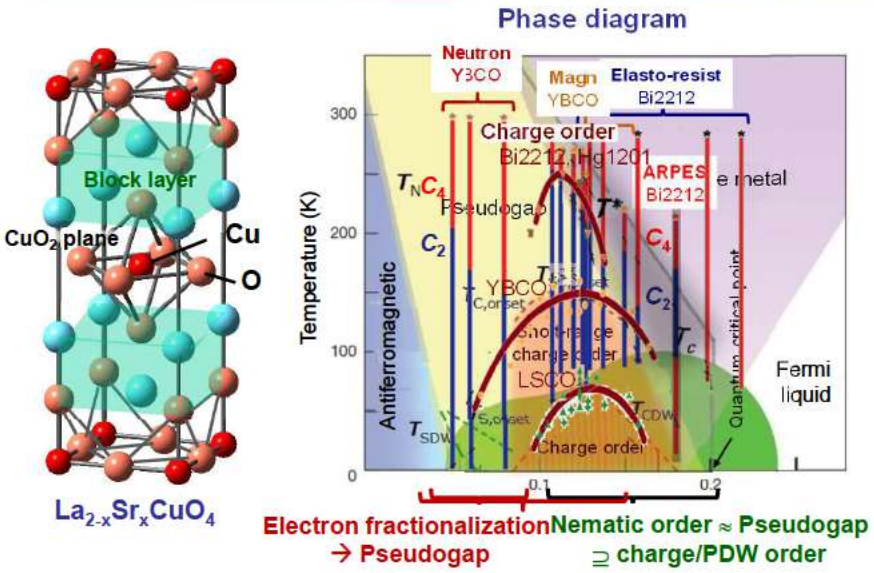

Outline

- **Cuprate high-T_c superconductors**
  - **Pseudogap, strange metal, high-T_c mechanisms …**
- **The origin of the pseudogap**
  - **Superconducting fluctuations/Preformed Cooper pairs?**
  - **Charge order/PDW? Translational symmetry breaking**
  - **Nematicity? Rotational symmetry breaking**
  - **Electron fractionalization? No symmetry breaking**
  - **Loop current? Time-reversal symmetry breaking**

Nematic order *vs.* charge/PDW order

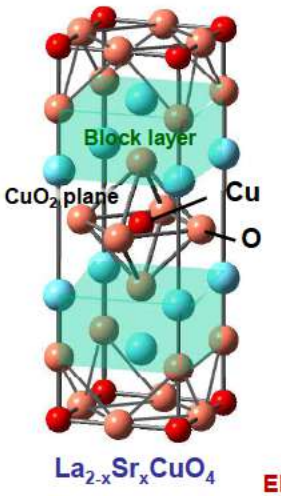

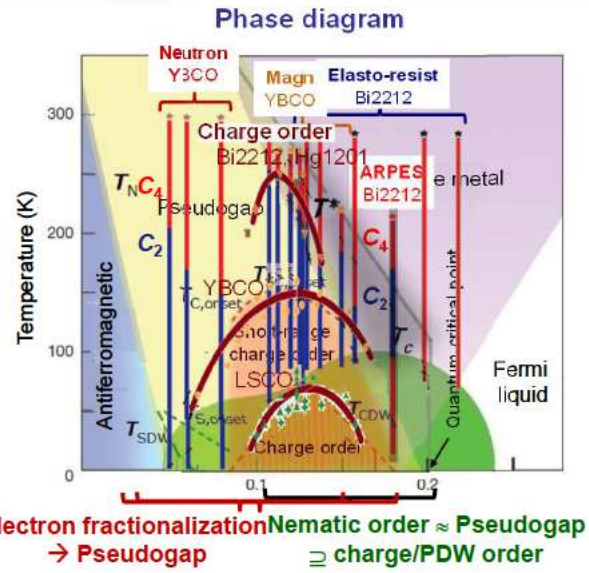

Electron fractionalization → Pseudogap

Nematic order ≈ Pseudogap ⊇ charge/PDW order

Outline

- **Cuprate high-T_c superconductors**
  - **Pseudogap, strange metal, high-T_c mechanisms …**
- **The origin of the pseudogap**
  - **Superconducting fluctuations/Preformed Cooper pairs?**
  - **Charge order/PDW?** Translational symmetry breaking
  - **Nematicity?** Rotational symmetry breaking
  - **Electron fractionalization?** No symmetry breaking
  - **Loop current?** Time-reversal symmetry breaking

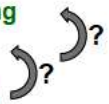

Nematic order *vs.* charge/PDW order

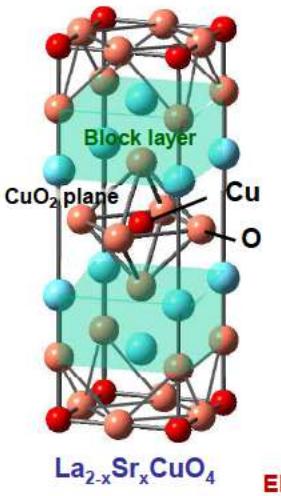

Phase diagram

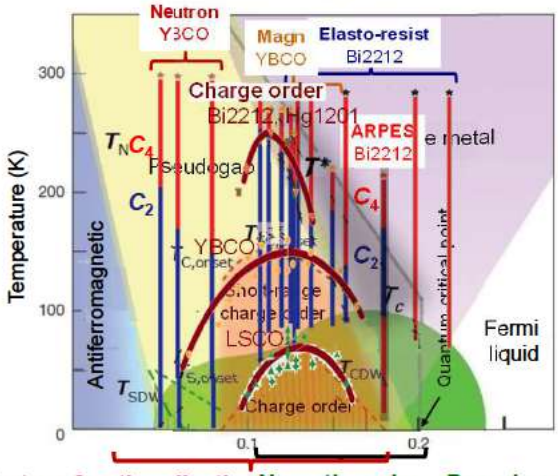

Electron fractionalization → Pseudogap

Nematic order ≈ Pseudogap → charge/PDW order

Summary

- **The origin of the pseudogap**
  - Superconducting fluctuations/Preformed Cooper pairs?
  - Charge order/PDW? Translational symmetry breaking
  - Nematicity? Rotational symmetry breaking
  - Electron fractionalization? No symmetry breaking
  - Loop current? Time-reversal symmetry breaking

- **Outlook**
  - Confirmation of electron fractionalization in cuprates using other spectroscopies (STM, pump-probe optics, …)
  - Application of the RIXS *e-h* pair excitation method to various quantum materials
  - Identification of new exotic phases using advanced spectroscopies

Acknowledgement

ARPES M. Horio (ISSP), C. Lin (U Zurich), S. Nakata (MPI Stuttgart), T. Yoshida (Kyoto U), K. Tanaka (UVSOR), M. Hashimoto, Z.-X. Shen (Stanford)

RIXS D.-J. Huang, A. Singh, J. Okamoto, H.-Y. Huang, C. T. Chen (NSRRC)

Theory M. Imada (Waseda U), S. Sakai (RIKEN), T.-K. Lee, C.-Y. Mou (NTHU), S. Johnston (UTK), T. P. Devereaux (Stanford)

Hole-doped cuprates H. Eisaki, D. Song, Y. Yoshida (AIST), S. Uchida (UTokyo), S. Komiya, Y. Ando (KRIEPI), T. Watanabe (Hirosaki U.)

Electron-doped cuprates T. Adachi (Sophia U), Y. Koike (Tohoku U)

Discussion T. Tohyama (TUS), H. Yamase (NIMS), M. Sato (Nagoya U.)

Electron fractionalization in Mott insulator and doped Mott insulator

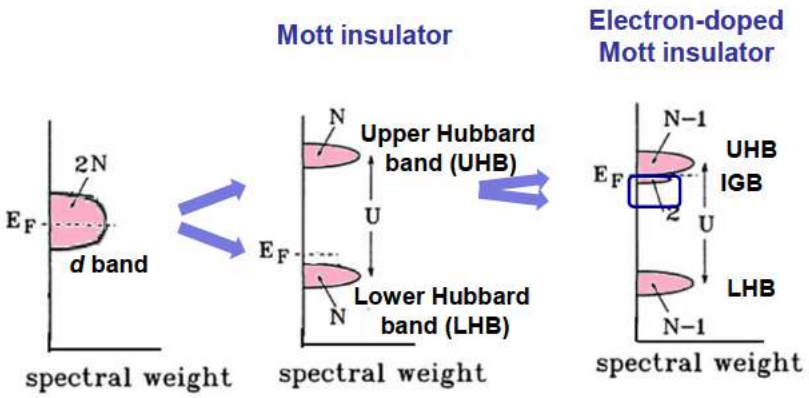

Hubbard-cluster calcula ion by:
H. Eskes, M. J. B. Meinders & G A. Sawatzky, PRL **67**, 1035 (1991).

ARPES of Pb-doped Bi2212 under uniaxial strain

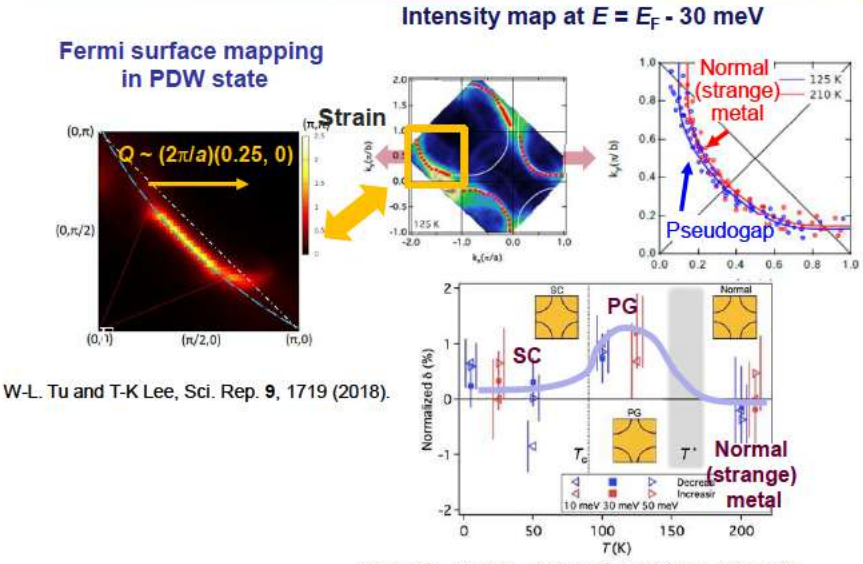

W-L. Tu and T-K Lee, Sci. Rep. **9**, 1719 (2018).

S. Nakata, AF *et al.*, npj Quantum Mater. **6**, 86 (2021).